NTNU

Norwegian University of
Science and Technology

Behaviour of the slip-cast crucible as a contamination source during silicon directional solidification

Hanna Vaksvik Skarstad

Chemical Engineering and Biotechnology
Submission date: July 2016
Supervisor: Marisa Di Sabatino, IMTE
Co-supervisor: Gaute Stokkan, SINTEF

Norwegian University of Science and Technology
Department of Materials Science and Engineering

Declaration

I hereby declare that this master thesis has been performed independently and in accordance with the rules and regulations of the Norwegian University of Science and Technology (NTNU).

Trondheim, July 2016
Hanna Vaksvik Skarstad

Preface

This master thesis is a part of the course TMT 4900 Materials Chemistry and Technology at the Norwegian University of Science and Technology (NTNU). The work has been a part of a collaboration project called "*Impurity Control in High Performance Multicrystalline Silicon*" where NTNU, IFE and SINTEF are research partners. The project is sponsored by the Research Council of Norway, REC Solar, REC Silicon, Steuler Solar and The Quartz Corp.

I would like to show my gratitude to my supervisor Associate Professor Marisa Di Sabatino Lundberg and co-supervisor Dr. Gaute Stokkan for their guidance and advice. I am very grateful for the inspiring and motivating conversations throughout the semester. A huge thanks is given to Dr. Antoine Autruffe for his clever suggestions and motivating words. I would like to thank Dr. Astrid Marie Flattum Muggerud for the good advice in the group meetings. I would also like to thank Dr. Kai Erik Ekstrøm for help with the EDS analysis and also helpful advice.

I would like to thank the technical staff of the department for equipment training and help with sample preparation when required. I would like to give a special thanks Morten Peder Raanes for performing the electron probe micro analyses.

Lastly, A warm thanks to my family and friends, especially to Magnus Vemundstad and Frode Vaksvik for proofreading.

Your help has been much appreciated!

Abstract

In this work, the behaviour of the slip-cast crucible as a contamination source of multicrystalline silicon during directional solidification (DS) was investigated. Transport parameters of iron were estimated in two types of amorphous silica materials; synthetic Heraeus quarts glass and a Vesuvius slip-cast crucible. The slip-cast crucible is porous and consists of sintered quartz glass particles, and has much lower density than the quartz glass. The diffusivity of iron the crucible and quartz glass was estimated at 1100, 1200 and 1300 °C. The solubility of iron has also been estimated in the quartz glass. Samples of both materials were heat treated in contact with a solid iron source to obtain contact diffusion. The diffusion profile of iron in quartz glass was obtained by using quantitative analysis (line scans) with an electron probe micro analyser. Semi-quantitative X-ray mapping was performed on the slip-cast crucible samples, followed by image analysis. The concentration profile of both materials were fit to the solution of *Fick's* diffusion equation under the appropriate conditions. The diffusivity of iron in quartz glass was estimated to be on the order of 10^{-15} and 10^{-14} m^2/s over the range of 1100-1300 °C. The diffusivity of iron in the crucible material was estimated to be on the order of 10^{-14} and 10^{-13} m^2/s over the range of 1100-1300 °C. The temperature independent diffusion constant and activation energy of the diffusion were estimated for both materials. The diffusivity in the quartz glass and the crucible can expressed as $D = 2,6 \times 10^{-13} \exp(-\frac{44,9 \text{kJ/mol}}{RT})$ m^2/s and $D = 1,2 \times 10^{-8} \exp(-\frac{146,7 \text{kJ/mol}}{RT})$ m^2/s, respectively. The diffusivity in the slip-cast crucible was an order of magnitude higher than the diffusivity of iron in the denser quartz glass. This indicates that the structure of the crucible affects the silicon contamination. The parameters obtained were applied in a finite element model that simulates the iron diffusivity across the crucible, coating and into the silicon melt during DS. The simulation resulted in a larger concentration in the melt when the values from the slip-cast crucible were applied. However, the difference from the quarts glass contamination was not as large as expected. It is reasonable to assume that if the simulation had been tested with even cleaner coating, a larger difference could have been observed.

Sammendrag

I dette arbeidet har digelens rolle som forurensingskilde under krystallisering (directional solidification) av multikrytallinsk silisium blitt undersøkt. Transportparametere av jern har blitt beregnet i to typer amorf silika: syntetisk kvartsglass og en slikkerstøpt digel produsert av Vesuvius. Det slikkerstøpte digelmaterialet er porøst og består av sintrede glasspartikler, og har mye lavere tetthet enn kvartsglasset. Diffusiviteten av jern i digelen og i glasset ble estimert ved 1100, 1200 and 1300 °C. Løseligheten av jern har også blitt beregnet i kvartsglass. Kontaktdiffusjon ble oppnådd ved å varmebehandle silikaprøvene i kontakt med en jernkilde. Diffusjonsprofilen av jern i kvartsglass ble beregnet ved bruk av kvantitativ analyse (linje scan) med en electron probe micro analyser. Semi-quantitative X-ray mapping ble utført på digelprøvene, etterfulgt av bildeanalyse. Konsentrasjonsprofilen av materialene ble kurvetilpasset løsningen av *Fick's* diffusjonsligning under de gjeldende forholdene. Diffusiviteten av jern kvartsglass ble estimert til å være av størrelsesorden 10^{-15} og 10^{-14} m^2/s i temperaturintervallet 1100-1300 °C. Diffusiviteten av jern i digelmaterialet ble estimert til å være av størrelsesorden 10^{-14} og 10^{-13} m^2/s i temperaturintervallet 1100-1300 °C. Den temperaturuavhengige diffusjonskonstanten og diffusjonens aktiveringsenergi ble beregnet for begge materialer. Diffusiviteten i kvartsglass og i digelen kan utrykkes som henholdsvis $D = 2,6 * 10^{-13} \exp(-\frac{44,9 \text{kJ/mol}}{RT})$ m^2/s og $D = 1,2 * 10^{-8} \exp(-\frac{146,7 \text{kJ/mol}}{RT})$ m^2/s. Diffusiviteten av jern i digelen er en størrelsesorden større enn diffusiviteten av jern i kvartsglasset. Dette indikerer at strukturen av digelen påvirker omfanget av silisiumforurensiningen. Parameterne ble brukt i en finite element model som simulerer jerndiffusjon gjennom digelen, coatingen og inn i silisiumsmelten under krystalliseringen. Modelleringen viste en større jernkonsentrasjon i smelten ved bruk av digelprøven enn kvartsglasset. Forskjellen var likevel mindre enn forventet. Det er rimelig å tro at ved bruk av renere coating kunne forskjellen observert vært større.

Contents

Chapter 1

Introduction

1.1 Motivation

Solar PV technologies only accounted for approximately 1,2 % of the global power generation at the end of 2015 [1]. In order to meet future energy demands in a sustainable manner, the share of global power production from solar cells must increase. The multicrystalline silicon (mc-Si) solar cell is the most cost effective solar technology. In order to increase the viability and competitiveness of multicrystalline solar cell, the cell performance must be improved.

The interaction of defects and impurities during the silicon crystallization process is directly related to the degradation of the solar cell efficiency. Metal impurities in the silicon ingot function as recombination centres for electron hole pairs which reduce the minority carrier life time of the cell. Understanding the introduction of impurities in conjunction with their effect on the solar cell efficiency, has gained a renewed importance due to recent advanced in the structure technology of mc-Si. Quantification of impurity transport parameters as well as knowledge about their behaviour has gained increased attention in recent years.

The slip-cast solidification crucible is widely acknowledged as a significant source of contamination of multicrystalline silicon ingots during directional solidification [2–4]. The slip-cast crucible is processed from natural quartz which contains impurities such as metal elements. The crucible consists of sintered quartz glass particles in various sizes which result in a material with much higher porosity than amorphous silica glass. During the crystallization stage of mc-Si, the crucible is generally coated with a silicon nitride layer. The impurities can diffuse through the media and be incorporated into the silicon. Quantification of the transport parameters of impurities through the slip-cast crucible is crucial to optimize the crucible material, reduce silicon contamination and improve the cell efficiency. Research has shown that the diffusivity measured in amorphous silica is considerably slower than the one measured in the slip-cast crucible

material [2, 5–8]. This indicates that the structure of the crucible affects the degree of silicon contamination.

1.2 Aim of this work

The present work investigates the behaviour of the slip-cast crucible as a contamination source of mc-Si silicon and aims to achieve the following objectives:

1. Quantify the diffusivity and solubility of iron in quarts glass at 1100 °C, 1200 °C, and 1300 °C, by performing solid state diffusion experiments and electron probe micro analysis (EPMA). The quartz glass can be representative of Czochralski crucibles and the fused glass particles in the slip-cast crucible structure. The material was also studied in order to obtain a reference of iron diffusion in amorphous silica materials.

2. Estimate the diffusivity of an actual slip-cast crucible material at 1100°C, 1200 °C, and, 1300 °C, by performing solid state diffusion and semi-quantitative X-ray mapping.

3. Apply the estimated parameters in a Finite element model that uses COMSOL Multiphysics as a solver. The model simulates the iron diffusivity across the crucible, coating and silicon, and into the silicon melt. The model also simulates the segregation at interfaces of the media. The simulation will contribute to better understanding of the silicon contamination during crystallisation and the significance of crucible structure and purity.

Chapter 2

Theory

2.1 Crystalline silicon solar cells

Crystalline silicon solar cells can be divided into two subcategories; multicrystalline and monocrystalline. Monocrystalline silicon consists of one large crystal and does not contain any grain boundaries, whereas the multicrytsalline silicon consists of many crystals in the mm^2-cm^2 range.

During the first stages of solar cell production, high purity silicon is extracted from natural quartz sand after carbothermic reduction and several refining steps. After the silicon has reached the purity standard required, the silicon feedstock is melted and crystallized. Different solidification methods are used to make monocrystalline and multicrystalline silicon and there are also different requirements to feedstock purity. Multicrystalline silicon is produced by using the directional solidification technique. During this stage, the silicon is in direct contact with a silicon nitride coated solidification crucible, usually made of silica. Monocrystalline silicon is crystallized through the Czochralski process, where one silicon crystal is grown and never in direct contact with the crucible and coating. The ingots are cut into wafers, cleaned and chemically treated to be finally completed into solar cells [9, 10].

While monocrystalline silicon can be considered extreme perfection, in terms of atomic structure and purity, multicrystalline silicon contains defects and impurities that are introduced mainly from the crucible, coating and feedstock. The degree of perfection in the silicon determines the cell ability to behave as a semiconductor. The monocrystalline solar cells therefore achieve higher efficiencies than the multicrystalline. Current laboratory cell efficiency records from monocrystalline and multicrystalline solar cells are 25.6 % and 20.8 %, respectively [11]. Commercial solar cell efficiency are approximately 5 percentage points lower for both technologies. However, the multicrystalline solar cells are the most cost effective.

2.2 Impurity impact on mc-Si

In mc-Si solar cells, defects and impurities interact to limit the semiconductor properties of the device. The interaction reduces the minority carrier life time and relative efficiency [12]. In recent years, advances in the crystallisation technology have led to mc-Si with lower defect density than before. This has been termed "high performance multicrystalline silicon". A new nucleation strategy results in smaller grains compared the original mc-Si. This nucleation strategy has made it possible to control and stop dislocation cluster proliferation during growth, which results in a material with improved structure [13–15]. Since important developments have occurred in terms of mc-Si structure and does no longer seem to be the largest contributor to deviation from perfect crystallinity, reducing the contaminants becomes increasingly important. The cell's sensitivity to impurities is high and introductions of only small concentrations can be detrimental to the cell performance. Figure 2.1 illustrates this concept. The graph presents the relative efficiency of the state-of-the-art (2010) solar cell as a function of feedstock impurity concentration of Ti, Cr, Cu, Ni and Fe [12]. Iron is an

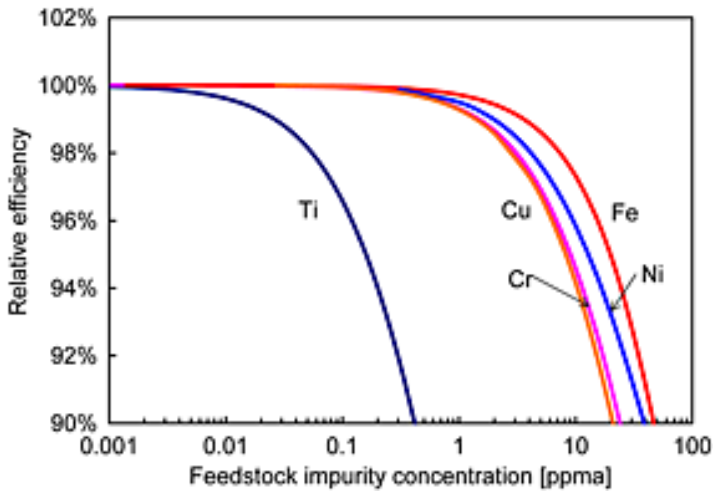

Figure 2.1: The relative efficiency of the solar cell as a function of feedstock impurity concentration of Ti, Cr, Cu, Ni and Fe. The device is state-of-the-art (2010) [12].

especially dominant and harmful metal impurity to the cell efficiency [16–18]. Iron forms complexes with defects and creates recombination centres, which reduces the minority carrier lifetime of the device. Iron can also contribute to crystal defects [18].

2.3 Directional solidification

During the crystallisation stage of mc-Si, directional solidification, the ingot contamination originates from the feedstock, coating, crucible and furnace. During this process the solid feedstock is melted and recrystallised. The Bridgman technique is illustrated in Figure 2.2. The coated crucible, containing molten silicon, is slowly moved downwards and away from the heated part of the process chamber. This way the temperature gradient is fixed and the silicon will nucleate from the bottom of the crucible. The grains will elongate parallel to the pulling direction [14, 19]. A typical temperature profile for this process in a Crystalox furnace is given in Figure 2.3 [4].

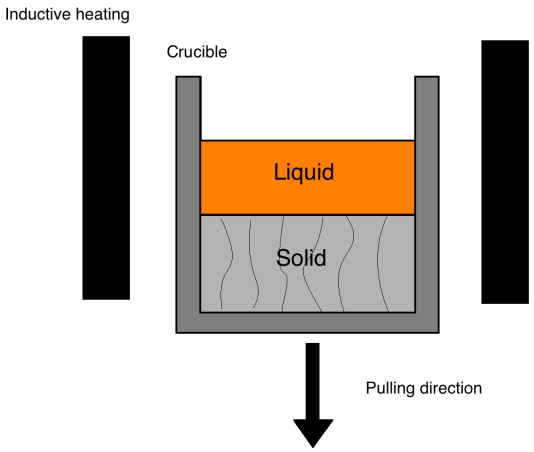

Figure 2.2: Multicrystalline silicon production with conventional Bridgman technique.

2.4 The solidification crucible

The silica (SiO_2) slip-cast crucible is the most used crucible for directional solidification. The crucible is produced by electrical fusion at 2000 °C, where a large amount of natural quartz sand is transformed into silica glass. The glass is crushed into particles with an appropriate size for the crucible manufacture. Silica powder is mixed with water and binder to form a fused silica slurry, which is poured into in a plaster mould. This is followed by several steps of moisture absorption and annealing at high temperatures. The resulting crucible consists of sintered quartz glass particles. Figure 2.4 shows a Vesuvius (ready to use) slip-cast crucible, spray coated with silicon nitride, containing a mc-Si ingot [20].

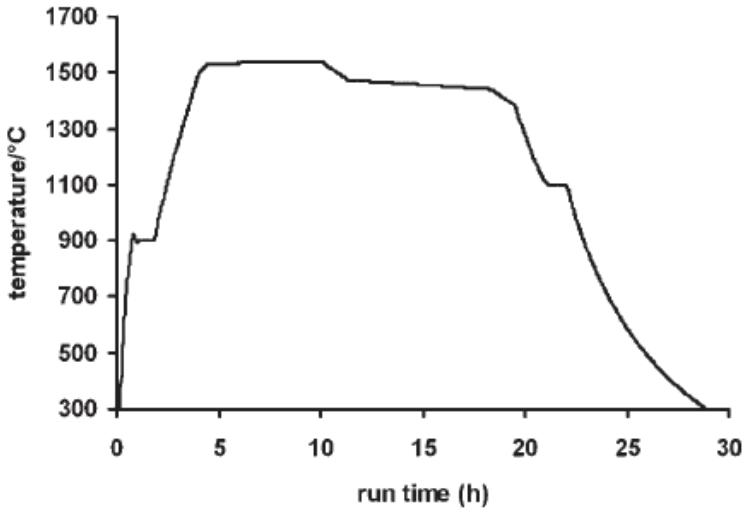

Figure 2.3: Temperature profile during directional solidification of silicon [4].

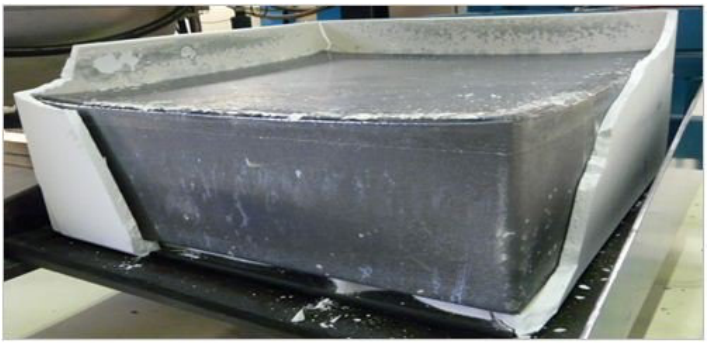

Figure 2.4: Spray coated Vesuvius silica slip-cast crucible with an mc-Si ingot [20].

Unfortunately solidification crucibles contain impurities, such as metal elements, originating from the natural quartz sand that are introduced during manufacture. Impurity measurements of iron and cobalt in a standard, a high purity crucible, crucible coating and silicon ingot are given in Figure 2.5. The impurities are measured horizontally from the edge towards the inner part of the ingot with inductive coupling plasma mass spectrometry [2]. The effects of crucible and coating contamination has been studied by several groups [2–4]. It has been acknowledged that impurities that diffuse into the silicon melt from the crucible and coating are dominating over feedstock contamination. High purity poly-silicon have been solidified in high purity and industrial grade coating and crucible systematically. Both the crucible and the coating had a significant impact on the impurity level of the solidified ingot [4].

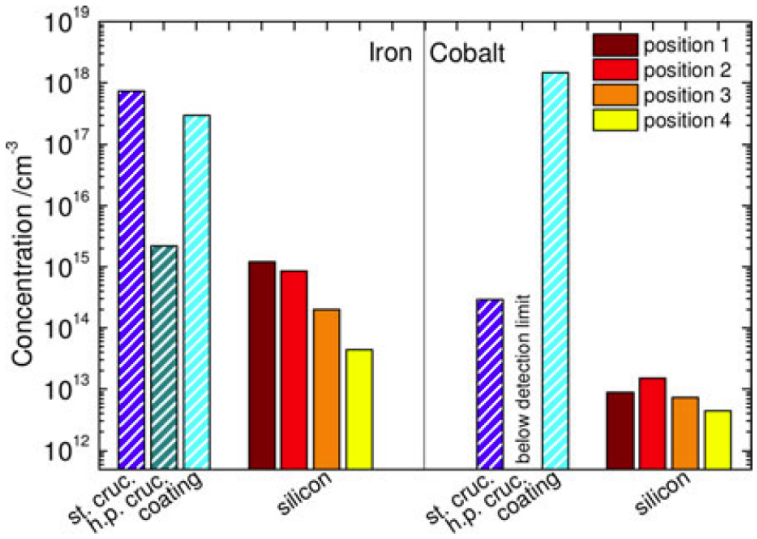

Figure 2.5: Impurity measurements of iron and cobalt in a standard, a high purity crucible, crucible coating and silicon ingot. The impurities are measured horizontally from the edge towards the inner part of the ingot with inductive coupling plasma mass spectrometry [2].

2.4.1 Silica

In order to gain a better understanding of the silica crucible's role as a contamination source, the nature and structure of amorphous silica must be examined. The silica polymorphs consists of different SiO_4 tetrahedra arrangements. A silicon atom is surrounded by four oxygen atoms in the tetrahedra. This results in an anion complex $[SiO_4]^{4-}$. A cis- and trans-configuration of $[SiO_4]^{4-}$-tetrahedra (without the central silicon atom showing) are shown in Figure 2.6a [21]. The difference between amorphous

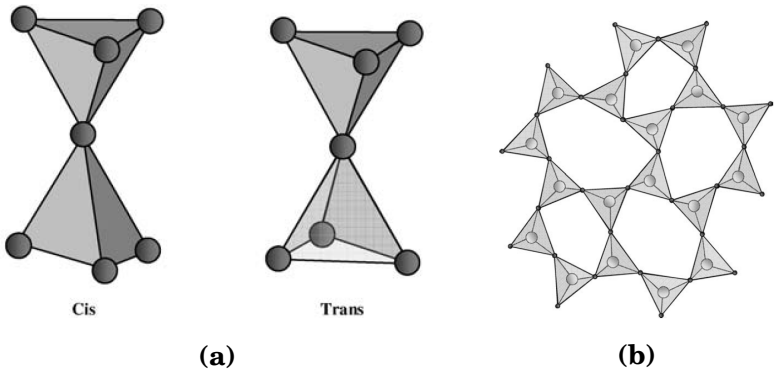

Figure 2.6: Structure of amorphous silica, 2.6a: A cis- and trans-configuration of $[SiO_4]^{4-}$-tetrahedra (without the central silicon atom showing) [21]., 2.6b: A disordered 3-dimensional network of silica [21].

silica and the crystalline phases, is determined by the SiO_4 tetrahedra arrangements. In crystalline silica the tetrahedra are arranged in a repetitive order. In amorphous silica, however, the tetrahedra are not arranged and form a disordered 3-dimensional network of silica as shown in Figure 2.6b [22–25]. The arrangement has the mean density of 2-2.20 g/cm^3. The crystalline silica phases are shown in the unary phase diagram of silica in Figure 2.7. A schematic illustration of silica phase transitions with

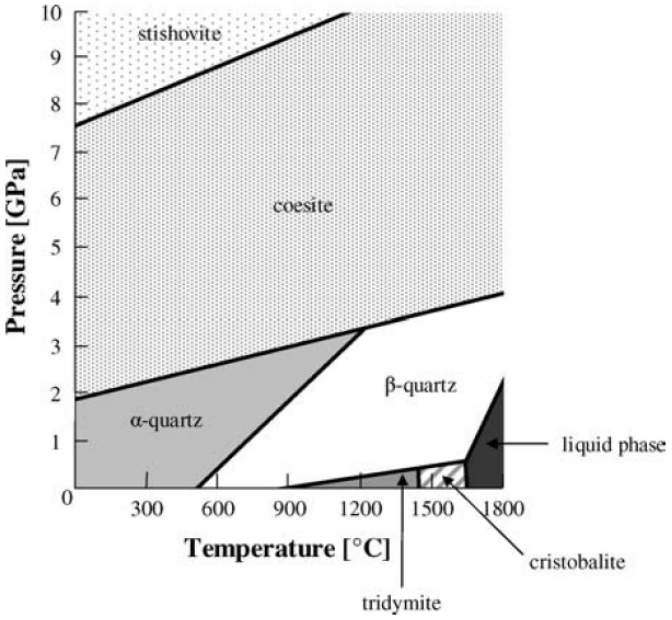

Figure 2.7: Phase diagram of silica [21].

decreasing temperature is shown in Figure 2.8. As shown in Figure 2.8, rapid cooling of liquid silica results in amorphous silica. Rapid cooling prevents silica from crystallizing, which results in a glassy substance [22, 23]. Fused quartz, silica glass and quartz glass are used interchangeably in the industry and are all synonyms for glass made from high purity quartz [26]. Quartz is the silica polymorph that is stable at room temperature and exists as an abundant mineral as can be seen in Figure 2.7. Amorphous silica is not a stable phase, and can be considered a disordered crystalline phase. The glass transition temperature, T_g, of SiO_2 lies at 1202 °C. Linear crystallization of amorphous SiO_2 into β-cristobalite has been observed by several researchers [21]. Depending on the temperature, one would expect from the phase diagram that heating up the silica glass would result in a phase transformation of β-quartz, β-tridymite or β-cristobalite. However, researchers have observed that silica turns directly into β-cristobalite at 1000 °C and melts at 1705 °C. Crystallisation of amorphous silica to β-cristobalite causes minor cracks around the crystallisation centres because of vol-

ume reduction. Low-temperature phase transition of β-cristobalite must be considered if the phase has been formed in the amorphous phase at elevated temperatures. β-cristobalite can undergo a phase transition below 300 °C from β-phase to α-phase. The phase transition causes volume decrease of 6,2 vol%. β-cristobalite formation has been observed to take place after 100 hours below 1000 °C and after 20h between 1100 and 1200 °C. Above 1400 °C the crystallisation transition can occur after minutes. The presence of impurities influences the crystallisation speed [21].

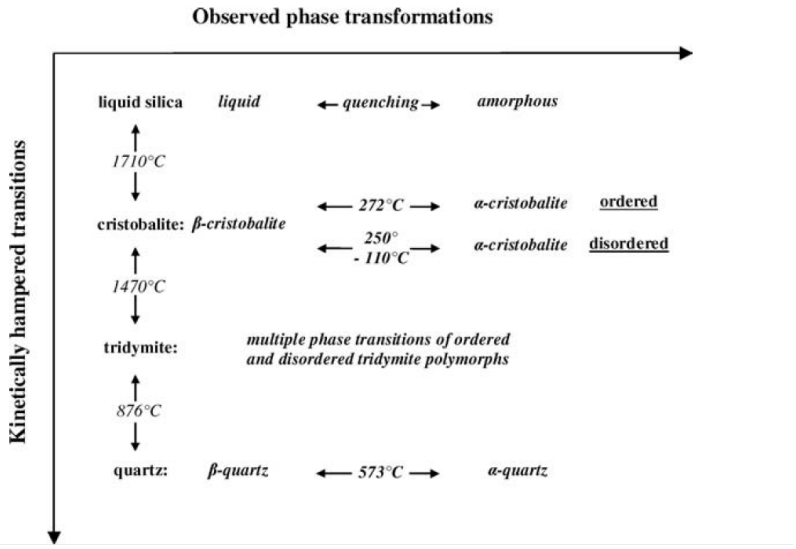

Figure 2.8: A schematic illustration of silica phase transitions with decreasing temperature [21].

Heraeus quartz glass is a pure type of quartz glass manufactured for optical purposes. The material density is 2.20 g/cm^3 [27]. Table 2.1 shows the impurity content of elements in ppm wt in HOQ 310. The glass has low bubble content and an extemely low coefficient of thermal expansion. At an interval of 0-900 °C the thermal expansion coefficient is 0,48 K^{-1}.

Table 2.1: Impurity content of elements in HOQ 310 [27].

Element	Al	Ca	Cr	Cu	Fe	K	Li	Mg	Na	Ti	OH
ppm wt	20	1	0,1	0,1	0,8	0,8	1	0,1	1	1	30

2.5 Impurity transport mechanisms

Considering the concentration of impurities in a crucible is not enough to determine its significance as a contamination source. A specie might be present in a large concentration, but never reach the silicon melt. Transport parameters of impurities in a material are crucial in order to understand how it behaves as a contaminant source. Transport mechanisms and properties of impurity elements are presented in the following sections.

2.5.1 *Fick's* law of diffusion

Diffusion is the process by which an element or impurity is transported, by random molecular or atomic motion, from a region of higher to lower concentration in a system [28, 29]. An isotropic material has the same diffusion properties and structure in every direction. The diffusion equations of an isotropic medium was developed by direct analogy to the equations of heat conduction and states that "the rate of transfer through a unit area of a section is proportional to the concentration gradient measured normal to the section" [29]. If diffusion does not change with time, the condition is termed steady state. Steady state diffusion of an isotropic material in one dimension is stated in Equation 2.5.1 and is referred to as Fick's first law [29]. J [$s^{-1}cm^{-2}$] is the diffusion flux and is defined as rate transfer per unit area. C [at cm^{-3}] is the concentration and x [cm] is the position within the solid. C plotted against x gives the diffusion profile. dC/dx is the concentration gradient. D is the constant of proportionality and is called the diffusion coefficient [cm^2s^{-1}].

$$J = -D\frac{dC}{dx} \tag{2.5.1}$$

When the diffusion is non-steady state, the concentration gradient varies with time at different points in the material. The diffusing species are eventually depleted or accumulated as a result. Under non-steady state conditions *Fick's* second law in one dimension applies and is given in equation 2.5.2 [28–30]. Concentration profiles at two different times and at the same holding temperature, where the surface concentration of diffusing species is held constant, are shown Figure 2.9. When D is independent of concentration, Equation 2.5.2 can be written as in Equation 2.5.3.

$$\frac{\delta C}{\delta t} = \frac{\delta}{x}(D\frac{\delta C}{\delta x}) \tag{2.5.2}$$

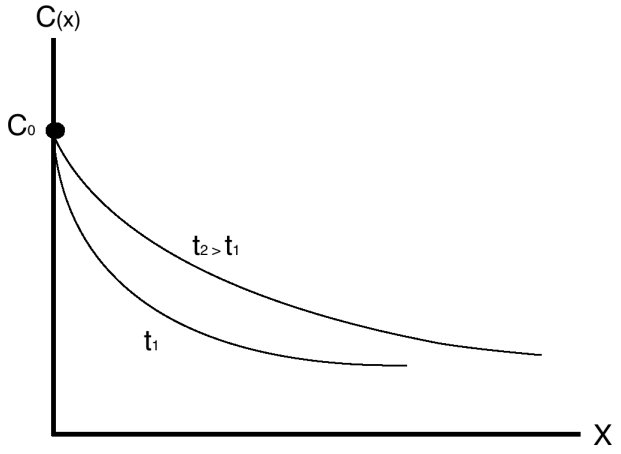

Figure 2.9: Diffusion profiles at different holding times at one specific holding temperature.

$$\frac{\delta C}{\delta t} = D\frac{\delta^2 C}{\delta x^2} \tag{2.5.3}$$

When boundary and initial conditions are specified, solutions to equation 2.5.3 can be obtained by the use of Laplace transformation. The derivation of the solution can be found in "The Mathematics of Diffusion" by J.Crank. In the case of a semi-infinite solid with a surface layer that is kept constant, the boundary and initial conditions are given in Equation 2.5.4 and 2.5.5 respectively. The solution to Equation 2.5.3 under these conditions is given in Equation 2.5.6, where C_0 is the boundary concentration, $C(x,t)$ is the concentration in point x at time t. D is the diffusion coefficient independent of time and concentration, however, dependent on temperature. The diffusion profile follows the error function, erf.

$$C(x,t) = C_0, \quad x = 0, \quad t > 0 \tag{2.5.4}$$

$$C(x,t) = 0, \quad x > 0, \quad t = 0 \tag{2.5.5}$$

$$C(x,t) = C_0(1 - \mathrm{erf}\frac{x}{2\sqrt{Dt}}) \tag{2.5.6}$$

A solid is termed Semi-infinite if the thickness, l, of the solid is over ten times the diffusion length $\sqrt{Dt}$, hence l>$10\sqrt{Dt}$. [28]. erf is equal to 1-erfz. erfz is given by Equation 2.5.7. Numerical values can be calculated and extensive tables of the error function are available [29, 31].

$$\mathrm{erfz} = \frac{2}{\pi^{0.5}}\int_0^2 \exp(-\eta^2)\,\mathrm{d}\eta \tag{2.5.7}$$

The Diffusion coefficient is temperature dependent and follows the *Arrhenius* equation given in Equation 2.5.8. D_0 is the temperature independent diffusion coefficient, E_a is the activation energy of the diffusion [J/mol], R [J/mol K] is the universal gas constant and T is the temperature [K]. The *Arrhenius* equation is also often expressed in terms of E_a [eV] and Boltzmans constant, k, [eV/K]. Equation 2.5.8 can be written with use of the natural logarithm as in Equation 2.5.9. When the natural logarithm of D is plotted as a function of inverse temperature, the y-intercept value of the linear regression will correspond to $\ln(D_0)$ and $\frac{E_a}{R}$ corresponds to the slope.

$$D = D_0 \exp(-\frac{E_a}{RT}) \tag{2.5.8}$$

$$\ln(D) = \ln(D_0) - \frac{E_a}{RT} \tag{2.5.9}$$

2.5.2 Solubility

The solubility limit of a material refers to the maximum amount of solute atoms that can be dissolved in a solvent to form a solid solution at a certain temperature [28]. It can be assumed that local equilibrium is reached at the interface between the material and a second phase. During contact diffusion, in cases when a precipitate or a phase is formed on the sample surface, the solubility can be obtained at a precipitate - sample interface. This is in accordance with the *Gibbs-Thompson* relation for thermodynamic equilibrium at a precipitate interface [32]. The precipitate or phase in this case behaves as an infinite contamination source of the sample, where the boundary concentration, C_0 forms instantly and is $\sim$ the solubility, S, which is kept constant at the interface. The solubility, S, is temperature dependent and follows the *Arrhenius* Equation as shown in Equation 2.5.10, where S_0 is the temperature independent pre-exponential factor, H_S is the activation energy or solution enthalpy [28]. Equation 2.5.10 can be written with use of the natural logarithm as in Equation 2.5.11. When the natural logarithm of S is plotted as a function of inverse temperature, the y-intercept value of the linear regression will correspond to $\ln(S_0)$ and $\frac{H_S}{R}$ corresponds to the slope.

$$S = S_0 \exp(-\frac{H_S}{RT}) \tag{2.5.10}$$

$$\ln(S) = \ln(S_0) - \frac{H_S}{RT} \tag{2.5.11}$$

2.5.3 Segregation

When two media with different solubilities of an impurity are in contact and diffusion occur, the impurities will separate at the interface of the two media according to the different solubilities. This phenomenon is called segregation. Different media can also mean different states of the same compound. An impurity is redistributed at the interface between two media until the ratio of the concentrations at the interface is equal to the ratio of the solubilities - i.e. the partition (or segregation) ratio. In silicon, the solubility is larger in the liquid phase than in the solid. For this reason, the impurities will prefer to stay in the melt as the silicon solidifies. The segregation coefficient between the two media is expressed as the ratio between the solubility in M_1, and M_2, in Equation 2.5.12 [33, 34].

$$k_0 = \frac{C_{M_1}}{C_{M_2}} \tag{2.5.12}$$

2.5.4 Diffusivity of iron in amorphous silica

The diffusion of iron in amorphous silicon dioxide has been studied by among others Atkinson et al., Ramappa et al., Kononchuc et al., Istratov et al. and Schubert et al. [2, 5–8]. The Arrhenius relationships are presented in Table 2.2, containing the temperature independent diffusion coefficient and activation energy. Each study has investigated different types of amorphous silica and applied different methods. None of the research considers quantitative measurement directly on a material equivalent to a solidification crucible. Ramappa, Atkinson and Kononchuc have performed quantitative analysis of iron diffusion in silicon dioxide. Rampappa measured the diffusivity of iron between 700-1100 °C. In the research, an iron layer was deposited on the surface of a thermally oxidized silicon wafer. Atkinson has measured the diffusivity of synthetic SiO_2 glass in the temperature range 500-1000 °C. Kononchuc has measured the iron diffusivity in the SiO_2 layer of silicon-on-wafer (SIO) structures between 900-1050 °C. Istratov has made a least square fit to diffusion data from Ramappa and Atkinson as well as Kononchuc. Schubert′s results are based on fitting a diffusion model to actual impurity measurements in silicon solidified in a slip-cast crucible. In Table 2.2 it can be seen that diffusivity measured in amorphous silica, as e.g. encountered in SOI structures, is considerably slower than in the amorphous silica with the slip-cast crucible structure.

Table 2.2: Temperature independent diffusion coefficients of iron in different structures of amorphous silica [2, 5–8]

Author	Structure	Method	D_{Fe} [cm^2/s]	
Atkinson	silica glass	Quantitative	6×10^{-3}	$\exp\frac{-3eV}{kT}$
Ramappa	silica glass	Quantitative	4×10^{-8}	$\exp\frac{-1.5eV}{kT}$
Kononchuc	silica glass	Quantitative	10^{-3}	$\exp\frac{-2.8eV}{kT}$
Istratov	silica glass	Curve Fit [5, 7, 8]	$2,2 \times 10^{-2}$	$\exp\frac{-3.05eV}{kT}$
Schubert	silica crucible	Modelling	50	$\exp\frac{-3.05eV}{kT}$

Unlike well ordered crystalline materials, amorphous materials cannot be expected to follow atomistic diffusion mechanisms. Amorphous materials are in a thermodynamically non equilibrium state [5]. In solid glass an atom must jump the size of an atomic diameter in order to diffuse. The diffusion in silica glass is therefore different from diffusion in the crystalline phases. The diffusion coefficient is dependent on the thermal history of the sample. In glass, the diffusion coefficient, viscosity and density are related to how quickly the glass is cooled through the glass transition temperature, as well as its final temperature of cooling. Rapid cooling leads to a less dense structure, low viscosity and hence larger diffusion coefficient. The properties of glass samples can vary even though they have the same composition [22]. Iron atoms will, according to the literature, behave as point defects in SiO_2 [7]. The diffusion will therefore be determined by thermal diffusivity and the density of the point defects. Fe^{2+} ions can react with SiO_2 to form fayalite (Fe_2SiO_4). Fe^{3+} ions can substitute the Si^{4+} positions in the anion tetrahedra. This would introduce positively charged oxygen vacancies, since the Fe^{3+} ion have 1+ lower oxidation number. The diffusion of iron will be determined by the interaction of the oppositely charged defects. Ramappa suggests that the the mechanism of iron diffusion in SiO_2 is a combination of vacancy and interstitial modes of diffusion. Ramappa found that the activation energy of the diffusion in SiO_2 is decreasing with atomic size of metals [5].

Chapter 3

Method

3.1 Diffusion couple experiments

3.1.1 Sample preparation

Diffusion couples consisting of amorphous silica and steel were prepared for heat treatments. Two types of diffusion couples were created; one contained a sample of slip-cast crucible material and one contained quartz glass. Both types of amorphous silica samples were coupled with steel as an iron source. A piece of the quartz glass and a piece of crucible material were weighed and the volumes were measured in order to estimate approximate volume densities of the materials.

Samples of solid steel, 30x30x7 mm, were provided by NTNU. The sample contact surfaces were ground before each heat treatment in order to obtain a flat and smooth surface to ensure sufficient sample contact. Each steel sample was ground mechanically on a Knut-Rothor machine from Struers with diamond abrasives in the following order: 220 piatto, 9 µm Allegro and 3 µm mol. The quartz glass samples were provided from the glass blower work shop at NTNU and manufactured by Heraus Quartz glass GmbH & Co (HOQ 310). HOQ 310 is manufactured by electrical fusion of natural quartz [27]. The samples were cut into 20x5x5 mm samples. The samples were cut by the glass blower work shop and cleaned in HF by Torlid Krogstad, staff engineer at the Department of materials science and Engineering. Slip-cast crucible material was provided from NTNU and produced by Vesuvius. The material was cut into 20x5x5 mm samples and ground with clean diamond abrasives in the same order as the steel samples.

Figure 3.1a and Figure 3.1b shows the slip-cast crucible material diffusion couple and quartz glass diffusion couple, respectively. The samples were secured with 0,5 mm thick Kanthal wire to ensure that the contact remained throughout the heat treatments. The Kanthal wire was only in contact with the silica samples on the top outer

surface, hence 5 mm away from the contact surface which is considered a safe distance away from the area the diffusion takes place. The Kanthal wire was not in contact with the sample at the interface between the steel and silica. The Kanthal wire was tightened approximately the same amount on each sample by using flat-nosed pliers. Both mechanical polish of the iron source as well as securing the diffusion couples with Kanthal wire were measures to ensure that the contact was optimal and that the diffusion was consistent throughout the heat treatment. These measures were introduced after previous work suggested that variations in diffusivity of iron in quartz glass were due to poor contact between the sample and iron source [35].

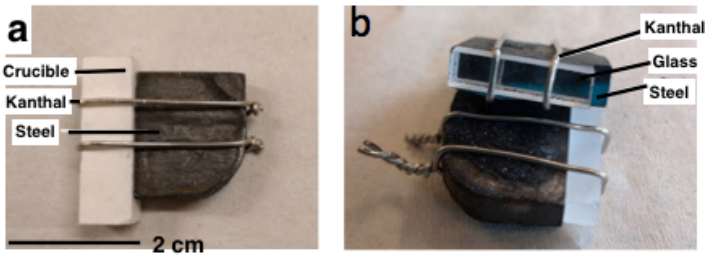

Figure 3.1: The diffusion couple set up of a) the slip-cast crucible and b) the quartz glass material, both in contact with steel, and secured with Kanthal wire.

3.1.2 Heat treatments

Two heat treatment series were performed. The quartz glass samples are named with an a.b.c.d system. a = material, where C means crucible, Q means quartz glass and Qr means quartz glass heat treated in argon atmosphere. b = temperature of heat treatment [°C], c = duration of heat treatment [h], and d = cronological sample number. An additional B is added, between c and d, in cases where the sample was cooled by quenching.

The first heat treatment series is presented in Table 3.1. The table contains temperature, times and sample names of the heat treatments of quartz glass and crucible samples in a Nabertherm LHT 04/18 air atmosphere furnace. The most logical choice would be to compare samples heat treated at the exact same holding times at different heat treatment temperatures. Earlier work [35] suggested that the heat treatment at 1100 °C had to be long enough for the iron concentration to exceed the detection limit of the quantitative analysis instruments. Secondly, the holding time at the highest temperature needed to be short enough to ensure that the iron concentration profile

had a slope. The choice was therefore made to use shorter holding times for the highest temperature heat treatments. According to the diffusion theory applied in this work given in Section 2.5.1, the diffusivity is independent of time under these conditions and the length of the holding time should be unessential. The ideal furnace would be a furnace with argon atmosphere, however, there was no such furnace available at NTNU which could be opened safely at high temperatures (1400 °C). The assumption was made that the absence of inert atmosphere would not affect the diffusion considerably. Quenching was introduced in order to avoid large precipitates to form and disturb the analysis. One set of samples was quenched and one was air cooled. Since the steel melted at the first heat treatment at 1400 °C, there were no further heat treatments at higher temperatures than 1300 °C

The second heat treatment series is presented in Table 3.2. The table contains the temperatures, holding times and sample names of the quartz glass samples heat treated in a Nabertherm N17/HR argon atmosphere furnace. Since quenching made the quartz glass samples too porous and full of cracks for further analysis, this was not continued for the second heat treatment series. The choice of proceeding to inert atmosphere heat treatments was also made. This was because more precipitation seemed to occur after heat treatments in air compared to results from previous work, where the heat treatments were executed in inert atmosphere [35]. The maximum temperature of the available argon atmosphere furnace was 1280 °C. Samples were also heat treated at one temperature at different times in order to verify the assumption of time independent diffusion coefficients.
All diffusion couples were heat treated in an alumina crucible and placed at the exact same spot in the furnace in order ensure similar heat treatment conditions. The samples were heat treated separately. The samples were placed in and removed from the furnace when the furnace had reached the desired holding temperature.

3.2 Techniques

In order to analyse the samples quantitatively the cross sections of the samples needed to be exposed. The samples were cut on a Conrad D-38678 Clausthal-Zellerfeld diamond saw and embedded in epoxy resin. The cross sections were then ground with waterproof silicon carbide paper (FEPA) and used in the following order: P#500 - P#800 - P#1200 - P#2400. The cross sections were further polished with 9µm allegro and 3µm and 1µm mol diamond abrasives.

Table 3.1: Temperature, times and sample names of the heat treatments of quartz glass and crucible samples in a Nabertherm LHT 04/18 air atmosphere furnace.

Material	Cooling medium	T[°C]	t[h]	Sample name
Quartz glass	Air	1100	17	Q.1100.17.1
		1200	5	Q.1200.5.1
		1300	3	Q.1300.3.1
	Water	1100	17	Q.1100.17.B.1
		1200	5	Q.1200.5.B.1
		1300	3	Q.1300.3.B.1
Crucible material	Air	1200	7	C.1200.7.1
		1400	3	C.1400.3.1
	Water	1100	17	C.1100.17.B.1
		1200	7	C.1200.7.B.1
		1300	3	C.1300.3.B.1

Table 3.2: Temperatures, holding times and sample names of the quartz glass samples heat treated in a Nabertherm N17/HR argon atmosphere furnace.

Material	Cooling medium	T[°C]	t[h]	Sample name
Quartz glass	Air	1100	0,17	Qr.1100.0,17.1
			0,5	Qr.1100.0,5.1
			1	Qr.1100.1.1
			3	Qr.1100.3.1
			3	Qr.1100.3.2
			5	Qr.1100.5.1
			7	Qr.1100.7.1
			15	Qr.1100.15.1
		1160	15	Qr.1160.15.1
		1200	3	Qr.1200.3.1
			15	Qr.1200.15.1
		1280	3	Qr.1280.3.1
			15	Qr.1280.15

3.2.1 ICP-MS

Two series of inductively coupled plasma-high resolution-mass spectrometer (ICP-MS) analysis were run with three slip-cast crucible material samples in each. The three

samples were taken from the outside, mid part and inside of the crucible in order to obtain the iron concentration of the slip-cast crucible before heat treatment and to detect any difference in iron concentration between the three areas in the crucible. Prior to analysis, the material samples were pulverised and dissolved in hydrogen fluorides solution prepared by Torild Krogstad. The ICP-MS determines the elemental content of the samples. A high-temperature inductively coupled plasma is coupled with a mass spectrometer. The atoms of the element in the sample are converted into ions by the icp source and separated and detected by the mass spectrometer [36]. This analysis was performed with an ICP-MS trippel quad Agilent 8800 combined with Element 2 at NTNU.

3.2.2 XRD

X-ray diffractometer (XRD) was performed on sample Qr.1280.3.1 after heat treatment. This was to investigate the ferrous surface layer forming on the sample surface, which behaves as an infinite contamination source. The XRD analysis was performed on a Bruker D8 Advance DaVinci X-ray Diffractometer. XRD identifies phases by comparison with data from known structures. Crystal structures diffract certain wavelengths. This way its possible to separate different crystal structures. Quantification of changes in the structural parameters is possible [37].

3.2.3 SEM

Samples were examined with a scanning electron microscope (SEM) prior to heat treatment. Secondary and backscatter electron micrographs were obtained. Five vertical and five horizontal lines were drawn on a secondary electron micrograph considered representative of the crucible structure, and the grains were counted along the lines. An approximate value of the average amount of grains per distance was obtained. All sample cross sections were examined, after heat treatment and preparation, in order to check if the surfaces were sufficiently prepared for EPMA analysis. Prior to analysis, the samples were coated with a thin layer carbon, in order to make the samples conducting, by using an Agar Turbo Carbon Coater. The analysis was performed on a low vacuum Fe-SEM (Zeiss Supra 55 VP) at NTNU. Energy dispersive X-ray spectroscopy (EDS) was performed on sample Qr.1100.0,17.1 and Qr.1100.0,5.1. The EDS is a part Zeiss Supra 55 VP and is used in conjunction with SEM. The EDS detects the X-rays emitted from the surface elements after bombardment of electrons to characterise the composition [38].

3.2.4 EPMA

Line scans of the quartz glass sample cross sections were executed using a JEOL JXA-8500F Electron Probe Micro Analyser. The instrument combines high SEM resolution with X-ray analysis of sub-micron areas. A fine focused electron beam bombards the surface. X-ray, secondary and backscattered electrons are emitted and their wavelengths and intensities are measured. The instrument at NTNU has 5 wavelength dispersive X-ray spectrometers (WDS) and an energy dispersive X-ray spectrometer (EDS) [39]. The uncertainty of the instrument is considered negligible in this study.

The element distribution of iron for all the samples was measured with EPMA. The iron concentration in mass% was measured along line scans across the sample cross sections. Morten Peder Raanes, Head engineer of the Department of Material Science and Engineering at NTNU, performed the analyses. The line scan started from the cross section edge (contact surface with iron) and each line scan was approximately 100 µm long. The probe step length was 0,5 µm and the size of the probe analysing volume was 1 µm.

Semi-quantitative X-ray mapping was performed on the crucible material samples. Four grey scale mappings were preformed per cross section. The maximum intensity on the grey scale corresponded to 70 mass%. This was set to obtain large enough contrast for the lowest values, but also to exclude disturbing noise from the mapping. The setting is assumed to give the most accurate result. To test if adjustments of the grey scale led to large differences in the result. X-ray mappings with maximum intensities of 20 mass% and 10 mass% were created.

To be absolutely sure that iron diffusion from Kanthal did not disturb the measurements, all quantitative measurements were performed at least 300 µm away from the sample surfaces that had been exposed to the furnace atmosphere.

3.3 Analyses

3.3.1 Image analyses

The four micrographs from each X-ray mapping, of areas right next to each other, were connected in Adobe Photoshop to form one image. The colour profile was changed into

two dimensional grey scale.

A script was created in Matrix Laboratory (MatLab) in order the obtain an approximate concentration profile average of iron in the slip cast crucible samples. The script is given in Appendix B.1. The script performs the following steps:

1. Imports image and returns a matrix with the image grey scale intensities of iron ranging from 1 to 256. The dimension of the intensity matrix (NxP) corresponds to the number of pixels (resolution) in the image. The top rows of the matrix correspond to the sample interface with the iron source. Iron has diffused downwards in the image/matrix. Hence, the values of iron in each column decrease towards to the bottom of the image/matrix. Each column can be pictured as a separate concentration profile. The width of the image corresponds to the number of columns (P).

2. Converts the intensities into iron concentrations by use of the relation given in Equation 3.3.1
$$\frac{(C_{max} - C_{min}) \times I}{I_{max} - I_{min}} = C_{Fe}. \tag{3.3.1}$$
Where C_{Fe} is the iron concentration. C_{max}, C_{min}, I_{max} and I_{min} are maximum and minimum values of iron concentration and intensity, respectively.

3. Excludes the values above the solubility limit of iron in amorphous silica in the next matrix. The values remaining were considered dissolved and diffused atoms. The concentrations above the solubility limit were considered precipitates and considered infinite sources of iron. The solubility of iron at 1100 °C in quartz glass was from earlier work estimated to be approximately 0,5 mass% [35]. The solubility of iron in quartz glass is assumed to also apply to the slip-cast crucible material. Since this is a very approximate value, and the solubility is also likely to increase with temperature, a tolerance of 0,3 mass% was included. A factor named "noise acceptance" was also included. This factor allows one or two subsequent values, above the solubility limit, to be included in the matrix. Two values above the solubility limit midst a column of values below the solubility limit were considered most likely to be noise. The values included by the noise acceptance factor, that were above the solubility limit, were converted to zero.

4. Creates one average column of iron concentrations. In other words, all the values in each row were averaged, which resulted in one column with dissolved iron concentration (average concentration profile).

3.3.2 Curve fitting

The obtained values for mass% of iron of each line scan and mapping were plotted as a function of distance. The plots were fitted to Equation 2.5.6 with the MatLab curve fitting tool. The parameters obtained were used to make Arrhenius plots with use of Equation 2.5.9 and 2.5.11. The temperature independent diffusion coefficient and solubility pre-exponential were quantified.

3.3.3 Impurity transport simulation

A model has been applied in this work to attain an approximate estimate of the concentration of iron that has diffused into the silicon melt during directional solidification. The model is a finite element model that uses COMSOL Multiphysics as a solver [40]. The finite element method (FEM) entails dividing a problem into sections or finite elements. The method is used to solve boundary condition partial differential equations numerically. The differential equations are given in Section 2.5.1. The model is one dimensional. Figure 3.2 shows the three domains in the model in form of line segments. The actual thickness of each domain (crucible, coating and wafer) is presented above the corresponding line segment. The solver is time dependent. In the model there is no liquid convection. The convection is accounted for by defining infinite diffusivity in the liquid, which means that the impurity distribution is homogeneous in the melt. In reality, there are convection loops in the silicon melt during directional solidification that keep the liquid homogenised, so the simplification is considered to be close to reality [34, 41]. The model requires the segregation at the interfaces and diffusion in the different media.

The solubility in the different media is required to obtain the segregation at the interfaces as explained in Section 2.5.2. In this simulation the segregation coefficient of iron at the interfaces of the crucible-coating and coating-silicon melt was set to 1. The applied segregation coefficient of iron at the solid-liquid silicon interface was $2*10^{-5}$. The time was set to 12 hours and the temperature to the melting temperature of silicon (1414 °C). The iron concentration of the crucible and coating are given Figure 2.5, which shows Schubert's estimations. The iron concentration of high purity coating is 1/5 of the iron concentration in the standard coating. The diffusivity, D, in the coating are also taken from Schubert's estimations and amounts to $D = 3\exp^{\frac{-3,05eV}{kT}}$ [2]. Schubert has used the activation energy obtained from Istratov [6]. The model quantified the approximate iron concentration that diffuses from the crucible and coating into

the melt. The Scheil equation, given in Appendix A, can then be applied. The equation converts the iron concentration in the liquid into iron concentration in the solid.

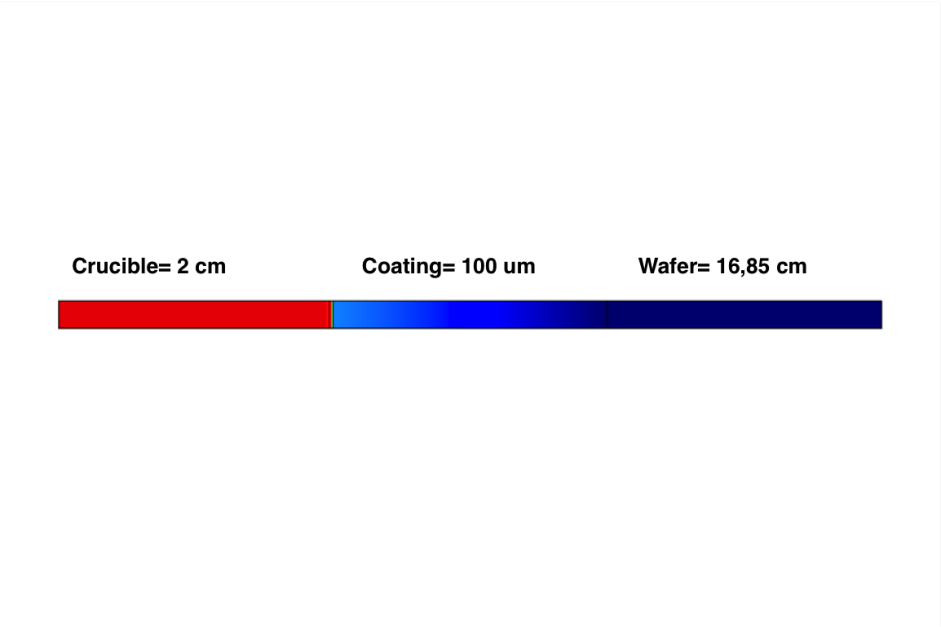

Figure 3.2: Shows line segments of the crucible, coating and wafer in model, which corresponds to the thickness of the media. The thickness of the media are written above the line segments.

Chapter 4

Results

The samples are labelled a.b.c.d as described in Section 3.1.2. The line scans are named a.b.c.d.e where an additional "e" is added to label the line scan.

4.1 Analysis of quartz glass

The measured volume density of the quartz glass was 2,23 g/cm^3. The equation applied is given in Appendix A. Figure 4.1a shows a backscatter image of a sample cross section heat treated at 1100 °C, where line scan Qr.1100.15.1.3 was performed. In Figure 4.1a the microprobe path can be seen as a red, vertical line along the surface in the centre of the cross section. The bottom black layer in the image is epoxy. The composition of the white phase above the epoxy was obtained from the line scan to be approximately 50 mass% iron, 35 mass% oxygen and 15 mass% silicon. The thickness of the layer varies on different places of the sample surface. In the image, an area with precipitates above the layer can be observed. The area further above consists of SiO_2 glass with diffused iron. Differences were observed in thickness of the iron oxide layer and in thickness of the area with precipitates. At higher temperatures the iron oxide layer was generally less continuous and the area with large precipitates was larger. This can be seen at a sample cross section heat treated at 1300 °C shown in Figure 4.1b, containing line scan Q.1300.3.1.1. The actual microprobe path can be observed as a light line in the centre of the cross section. The samples heat treated at 10 and 30 minutes at 1100 °C, Qr.1100,0,17.1 and Qr.1100,0,5.1, were analysed qualitatively with SEM an EDS. This was to investigate:

1. How early a new phase formed on the sample surface during heat treatment.
2. To confirm that the phase formed at the surface of the sample was an iron oxide phase.

Both of the samples contained the white surface layer when examined in SEM. Figure 4.2 shows the EDS results of the sample Qr.1100,0,17.1 cross section. The epoxy is the black phase to the left, the iron oxide phase is the white phase in the centre,

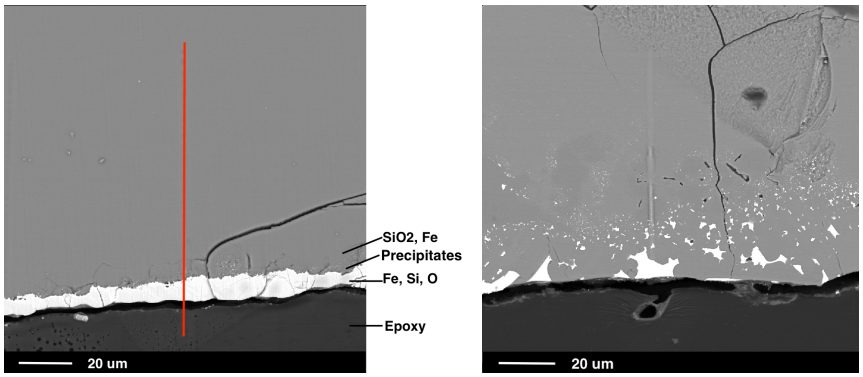

(a) **(b)**

Figure 4.1: Figure 4.1a shows a backscatter image of a sample cross sections heat treated at 1100 °C, where line scan Qr.1100.15.1.3 was performed. The microprobe path can be seen as a red, vertical line along the surface in the centre of the cross section. Figure 4.1b shows a backscatter image of a sample cross sections heat treated at 1300 °C, where the line scan Q.1300.3.1.1 was performed. The actual microprobe path can be observed as a light line in the centre of the cross section.

and the phase to the right is SiO_2 phase with the diffused iron. The Figures present the same area with different elements detected. A secondary electron image of the area analysed is shown in Figure 4.2a. Figure 4.2b shows iron as blue, oxygen as green and silicon as red. The abundance of points in each colour, corresponds to the amount of the element present. The white layer in Figure 4.2a corresponds to the iron, silicon, oxygen containing phase in Figure 4.2b. This is confirmed by viewing each of the elements individually. Iron, oxygen and silicon are presented in Figure 4.2c, 4.2d and 4.2e, respectively. In order to determine which crystalline phases were present in a heat treated quartz sample, sample Qr.1280.3.1 was analysed with XRD. The intensities plotted against diffraction angle is shown in Figure 4.3. The peaks correspond to crystalline phases and only three can be observed. The phases that matched the peaks were synthetic cristobalite and quartz. No crystalline phase of iron oxide silicon was observed.

4.1.1 Iron distribution

Figure 4.4 shows the full iron distribution of line scan Qr.1100.15.1.3 and can roughly be divided into five parts. The parts are marked with vertical lines and numbered. The first part of the data points corresponds to the epoxy. The second part corresponds to the iron oxide phase as well as its interface with SiO_2. The third part contains the scattered points, where the iron content in the data points is decreasing towards the

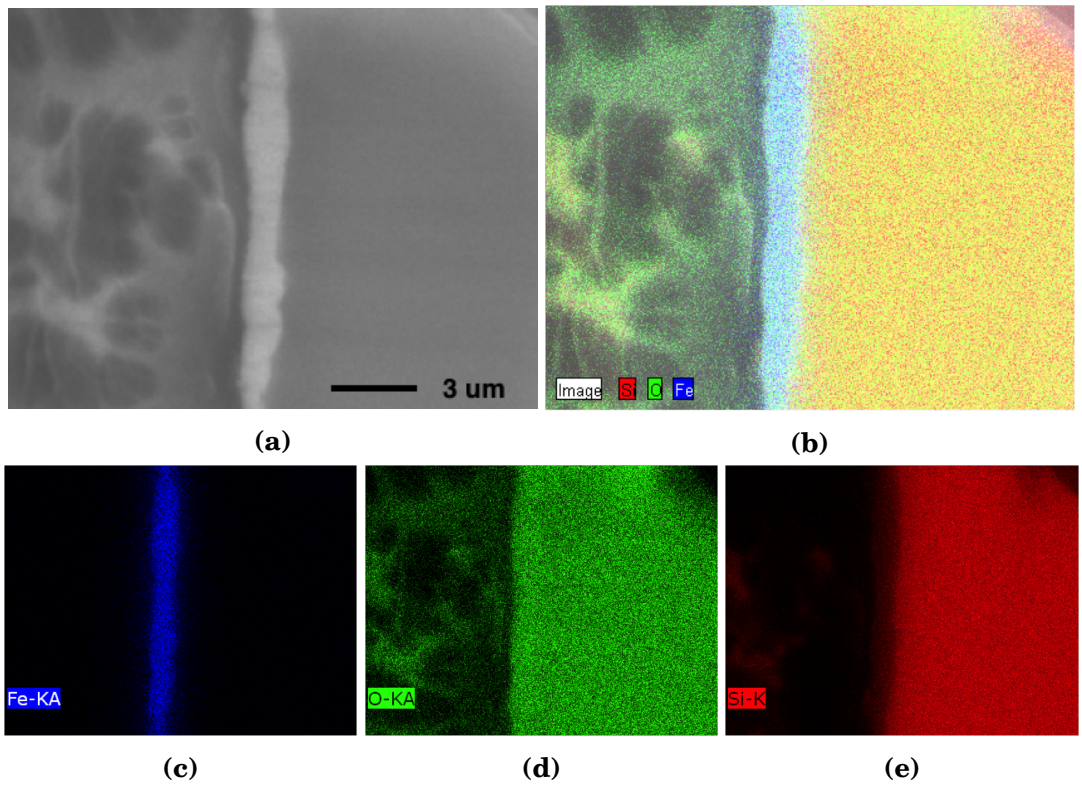

Figure 4.2: Shows five EDS images of the sample Qr.1100,0,17.1 cross section. The epoxy is the black phase to the left, the iron oxide phase is the white phase in the centre, and the phase to the right is SiO_2 phase with the diffused iron. The Figures presents the same area with different elements detected. Iron is blue, oxygen is green and silicon is red.

continuous line of data points at 0,34 mass%. The fourth part is the main result and consists of a continuous line of data points used as the diffusion profile in this study. The values below the detection limit of the EPMA instrument, 0,013 mass%, were not included. In order to obtain a diffusion profile as accurate as possible, the scattered data points were excluded. This corresponds to the part five in Figure4.4.

4.1.2 Approximation to the diffusion equation

The fit curve, obtained from fitting the diffusion profile to Equation 2.5.6, is presented as a black line in Figure 4.5. The diffusion profile begins after the part with precipitated particles, however the most accurate value of the solubility would be at the interface between the iron oxide phase and SiO_2 as stated in Section 2.5.2. In order to avoid the disturbance of the particles, the fit curve has been extrapolated to reach the interface as shown in Figure 4.6. The temperature dependent diffusion coefficients, D, and solubility, S, from the diffusion profile and the fit curve from the line

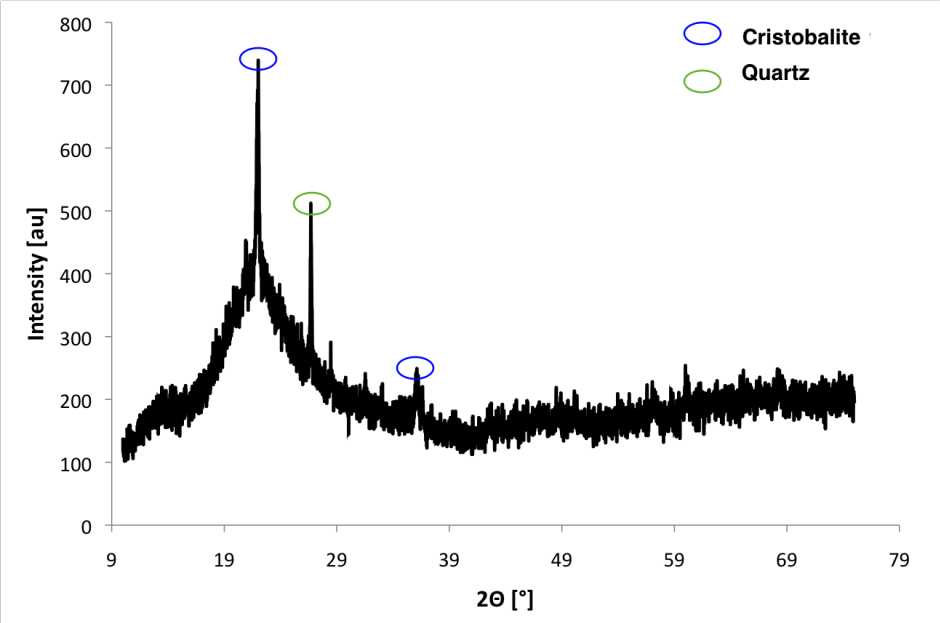

Figure 4.3: XRD analysis of sample Qr.1280.3.1. The intensities are plotted against diffraction angle. The peaks correspond to synthetic cristobalite and quartz

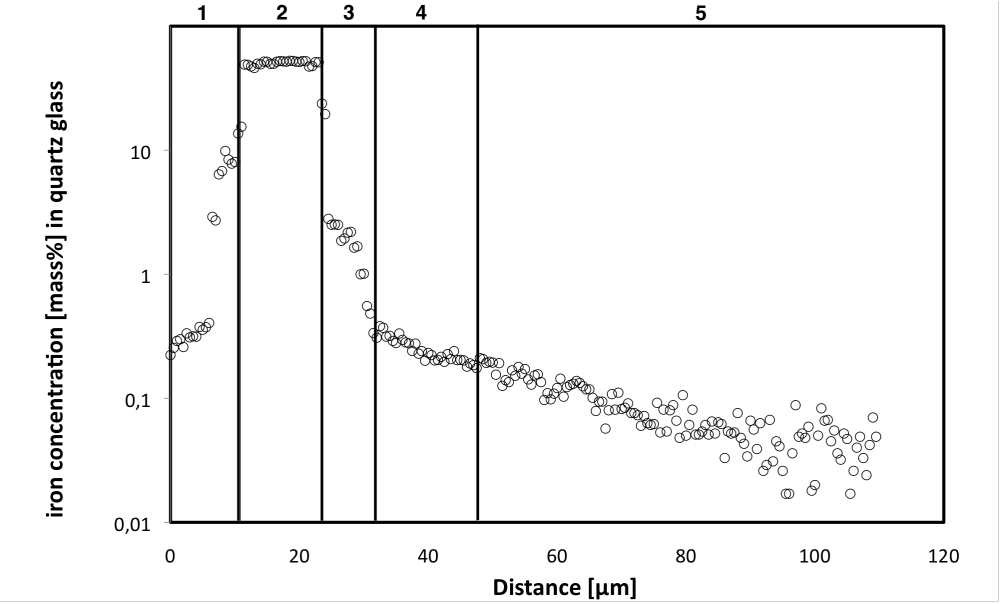

Figure 4.4: Concentration of iron as a function of distance [µm] obtained from line scan Qr.1100.15.1.3. The concentration profile is divided into five different parts.

scan data points are presented in Table 4.1. The rest of the back scatter cross sections images, from where the line scans in Table 4.1 were performed, are given in Appendix C.1. The rest of the concentration profiles that were used to estimate the parameters

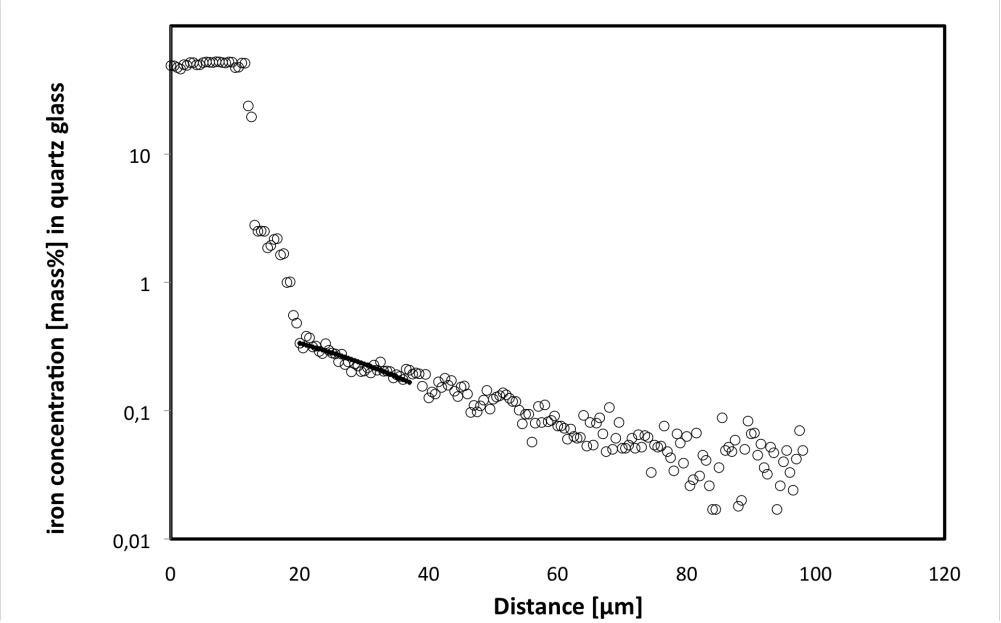

Figure 4.5: Concentration of iron as a function of distance [µm] obtained from line scan Qr.1100.15.1.3. A curve fit to the diffusion equation is shown as a black line

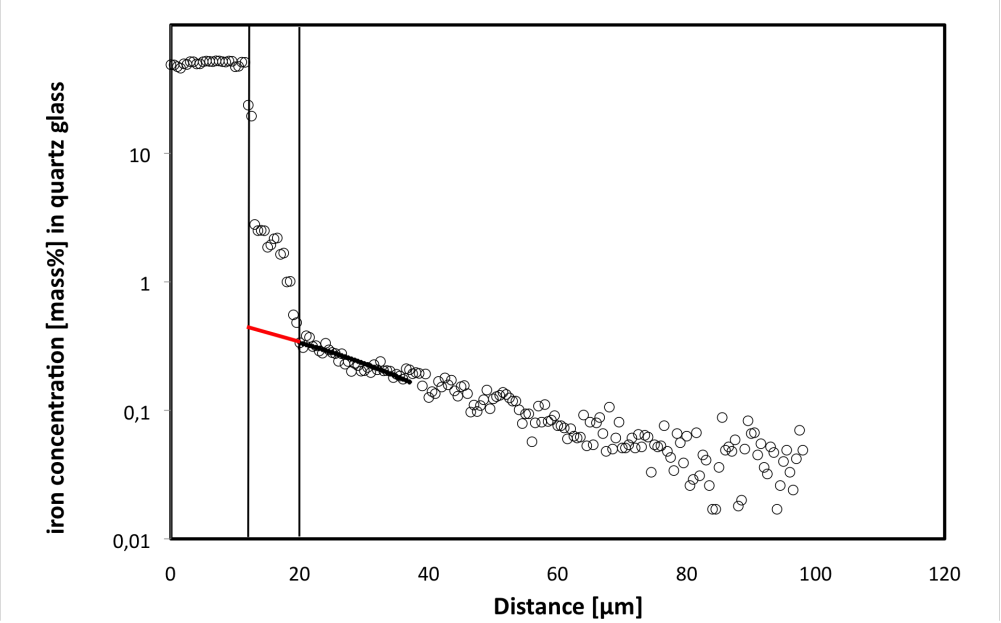

Figure 4.6: Concentration of iron as a function of distance [µm] obtained from line scan Qr.1100.15.1.3. A curve fit to the diffusion equation is shown as a black line, and the fit curve is extrapolated to reach the iron oxide interface

in Table 4.1 are given in Appendix D. No diffusion profiles were obtained from sample Q.1200.5.1, Qr.1200.3.1, the samples heat treated at 1160 and 1280 °C, and the

Table 4.1: Temperature, duration of heat treatment, sample name and corresponding diffusivity, D, boundary concentration, C_0 and solubility, S, from the diffusion profiles and fit curves.

T[°C]	t[h]	Line scan	D[m^2/s]	C_0[mass%]	S[mass%]
1100	3	Qr.1100.3.1.1	$1{,}11\times10^{-14}$	0,59	0,59
		Qr.1100.3.1.2	$1{,}45\times10^{-14}$	0,72	0,78
		Qr.1100.3.2.1	$1{,}78\times10^{-14}$	0,38	0,44
	5	Qr.1100.5.1.1	$1{,}04\times10^{-14}$	0,25	0,38
		Qr.1100.5.1.2	$3{,}09\times10^{-15}$	0,36	0,73
	7	Qr.1100.7.1.1	$3{,}66\times10^{-15}$	0,16	0,19
		Qr.1100.7.1.2	$2{,}86\times10^{-15}$	0,17	0,21
	15	Qr.1100.15.1.1	$4{,}34\times10^{-15}$	0,42	0,49
		Qr.1100.15.1.3	$5{,}78\times10^{-15}$	0,34	0,42
	17	Q.1100.17.1.1	$1{,}58\times10^{-15}$	0,28	0,40
		Q.1100.17.1.2	$1{,}32\times10^{-15}$	0,28	0,44
1200	15	Qr.1200.15.1.1	$2{,}52\times10^{-15}$	0,16	0,21
		Qr.1200.15.1.2	$5{,}36\times10^{-15}$	0,12	0,15
		Qr.1200.15.1.3	$2{,}59\times10^{-15}$	0,16	0,30
1300	3	Q.1300.3.1.2	$1{,}71\times10^{-14}$	0,16	0,22
		Q.1300.3.1.3	$6{,}86\times10^{-15}$	0,19	0,38

quenched samples. The profiles were scattered and discontinuous. The average diffusion coefficient at each temperature with error bars are presented in Figure 4.7. The average solubilities are presented in Figure 4.8

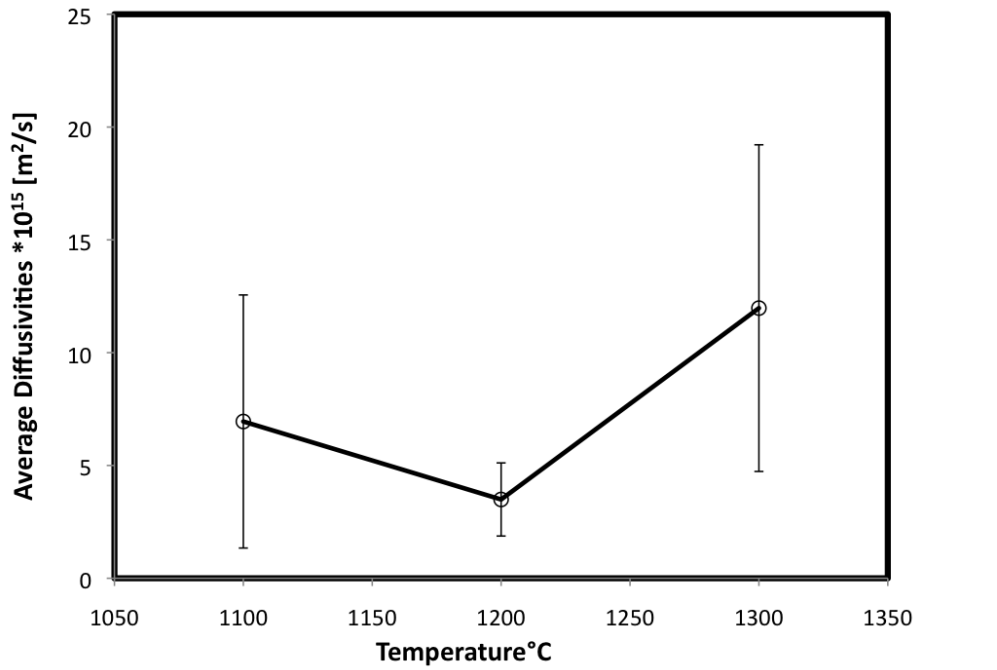

Figure 4.7: Average diffusion coefficients with error bars at 1100, 1200 and 1300 °C.

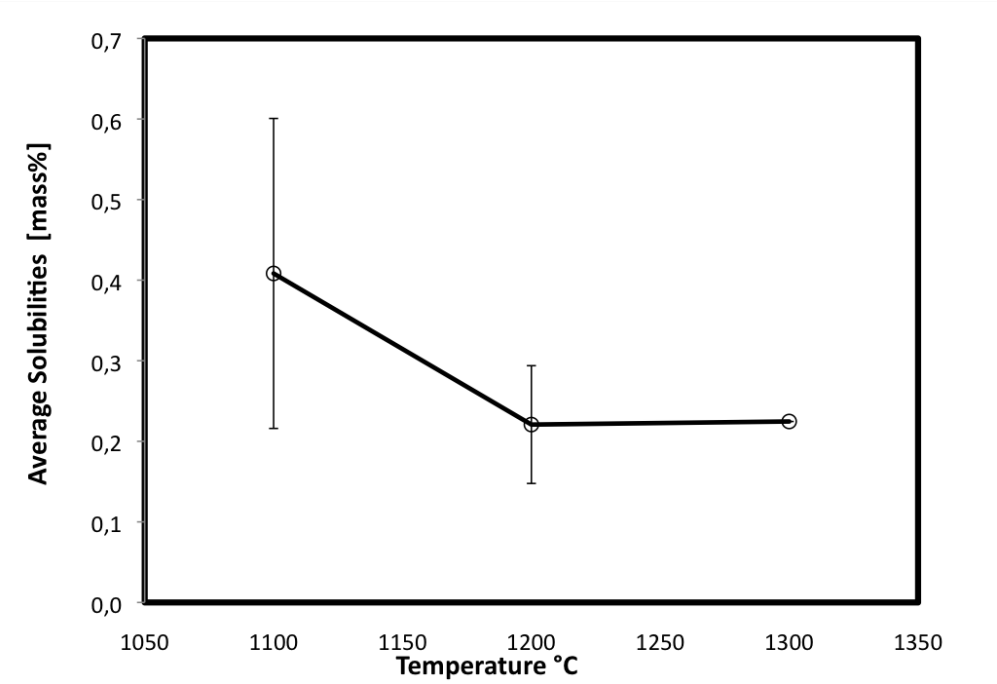

Figure 4.8: Average solubilities with error bars at 1100, 1200 and 1300 °C.

4.2 Analysis of crucible material

A secondary electron micrograph of a polished crucible sample cross section before heat treatment is shown in Figure 4.9. The average amount of grains per distance were found to be 57,5 grains/mm. The measured volume density of the material was found to be 1,9 g/cm^3. The density equation applied is given in Appendix A. Two series of samples from three parts of the crucible were tested with ICP-MS. The iron concentrations in the different samples are given in Table 4.2.

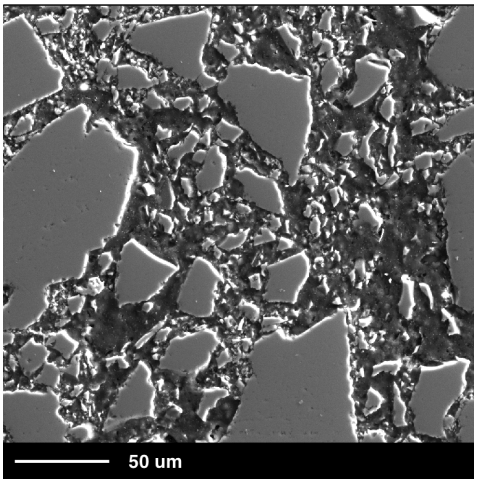

Figure 4.9: A secondary electron micrograph of a polished crucible sample cross section before heat treatment.

Table 4.2: ICP-MS values of iron concentration from the inside, middle part and outside of a Vesuvius silica crucible, prior to heat treatment.

Series	Position in crucible	iron concentration [ppm wt]
1	inside	46,9
	middle	59,9
	outside	46,9
2	inside	29,9
	middle	45,2
	outside	26,4

The semi quantitative X-ray mapping was performed on the cross sections of the samples C.1100.17.1, C.1200.7.1 and C.1300.3.1. The relationship between intensity and mass% of the resulting images was adjusted to give the most accurate result. Three

images with different intensity adjustments were created from each mapping. The image, which would presumably give the most trustworthy result, had the following contrast adjustments: High enough contrast for the lowest intensities to be detected, but also low enough to exclude disturbing noise from the mapping. This was found to be the case in which the maximum intensity of the image corresponded to 70 mass%. Images with different contrast scaling were created in order to test if the adjustments of the grey scale led to large differences in the results. Hence, to investigate if it was sufficient to determine the most trustworthy grey scale adjustments based on the visual quality of the image. Images with 20 mass% and 10 mass% as maximum intensities were created to compare. Figure 4.10a shows a backscatter electron image of the cross section of sample C.1100.17.1. The white phase in the image corresponds to a second phase containing iron. The top of the image shows the interface that was in contact with iron during heat treatment. Figure 4.10b, 4.10c and 4.10d present the X-ray mapping images of the cross section C.1100.17.1, with image maximum intensity corresponding to 70 mass%, 20 mass% and 10 mass%, respectively.

In the case of the crucible material, there is no clear interface between the surface layer and silica. The solubility of iron in the crucible material can therefore not be estimated in the same manner as quartz glass. As can be seen from Figure 4.10a there are large precipitates in the structure. The precipitates are assumed to behave as infinite contamination sources as described in Section 2.5.2. The area with diffused iron is therefore obtained below the visible layer of precipitates. It can also be observed that the detected iron in the images are deeper into the structure when there are fewer large grains present. This has been accounted for in the script created in Matlab, explained in Section 3.3.1. The diffusion depth along the width varies, hence the values in columns with diffused iron values have different starting points in the matrix. Therefore the columns must be adjusted to the same height in order to obtain an average column in a meaningful way. As described in Section 3.3.1 the point at which the values start being below the solubility limit is detected. All the values above are converted to zeros by the script. Each of the columns are pushed up to the first row of the matrix to make sure that the concentrations that have diffused the same length are on the same row in the matrix. Hence, the values that have diffused the same length are averaged in order to obtain an average concentration profile as a function of distance.

The average solubility of 0,5 mass% was obtained for 1100 degrees for quartz glass

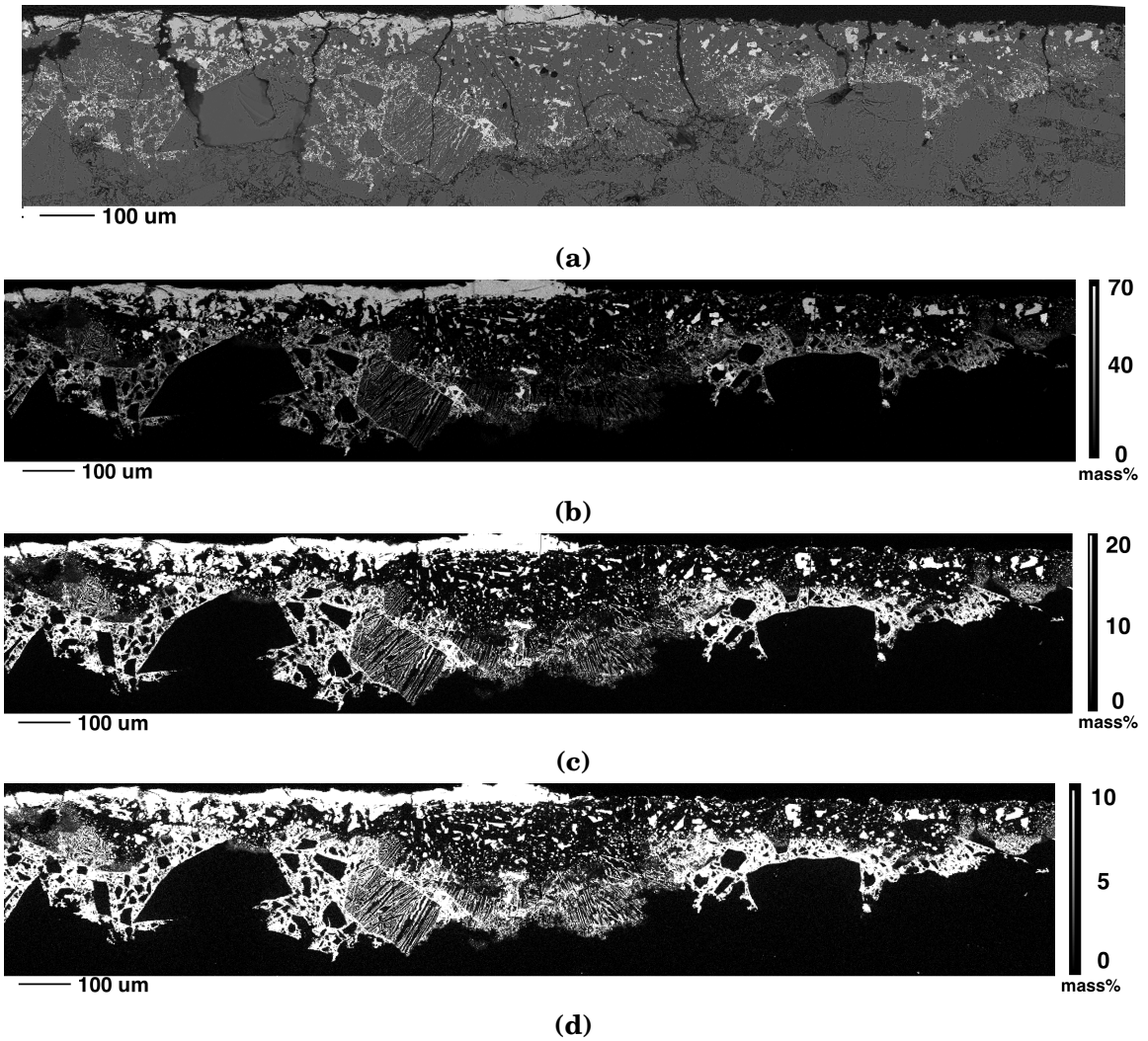

Figure 4.10: Figure 4.10a shows a backscatter electron image of the cross section of sample C.1100.17.1. Figure 4.10b, 4.10c and 4.10d present the X-ray mapping images of the cross section C.1100.17.1, with image maximum intensity corresponding to 70 mass%, 20 mass% and 10 mass%, respectively.

in previous work by the author. Only an approximate value is required, since the technique is not entirely quantitative and it was considered a reasonable assumption to add 0,3 mass% tolerance to be sure to obtain a continuous iron concentration profile. A solubility limit of 0,8 mass% was therefore applied in the script. A noise acceptance factor (explained in Section 3.3.1) of two was considered a reasonable adjustment. The factor is added in order to avoid columns of diffused iron concentrations being excluded because of values that can be considered as noise. The average diffusion profile obtained with the optimal script adjustments is presented in Figure 4.11. The part

of the curve fitted to Equation 2.5.6 is marked with a red line. The first data points are not part of the diffusion profile as the script makes sure the first columns does not contain many zeros, and are unnaturally higher than the rest of the data points. The diffusion profile therefore starts by the red fit curve.

In order to test the significance of introducing tolerance and noise acceptance, six different scenarios were created. The images of which the maximum intensity of the image corresponded to 70 mass%, were imported and run through the script with the six different scenarios. Scenario 1, 2, and 3 have the solubility of 0,5 mass% and Scenario 4, 5, and 6 have the solubility of 0,8 mass%. The noise acceptance increases from 0 to 2 for both solubilities. Figure 4.12 shows the diffusion profiles from the six different scenarios obtained from sample C.1100.17.1. The scenarios in the first columns (a, b, c) have the solubility adjustment of 0,5 mass%. The second column (c, d, f) has the solubility adjustment of 0,8 mass%. The first, second and third row have the noise acceptance adjustment of 0, 1, and 2, respectively.

The diffusivities at the three different temperatures that resulted from the different conditions are presented in Table 4.3. The concentration profile of Scenario 1 was too scattered to give a trustworthy diffusion profile for each of the three samples. Scenario 2 for sample C.1200.7.1 was also too scattered. The rest of the mapping images are presented in Appendix C.2. The rest of the concentration profiles used to estimate the diffusivities in Table 4.3 are given in Appendix D.

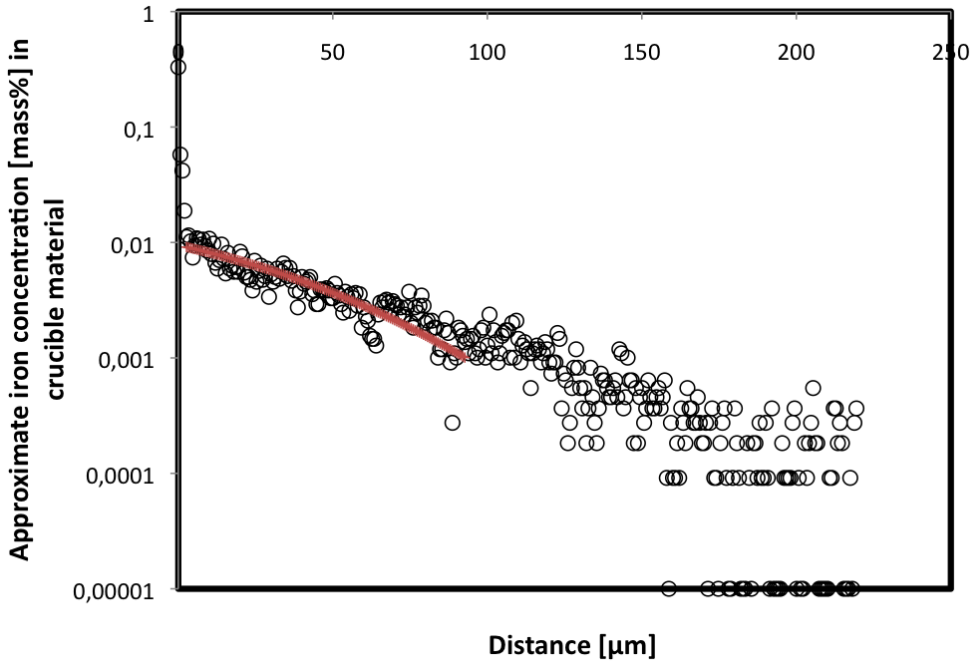

Figure 4.11: Shows the concentration profile of Scenario 6, in which the maximum intensity of the image corresponded to 70 mass% at 1100 °C

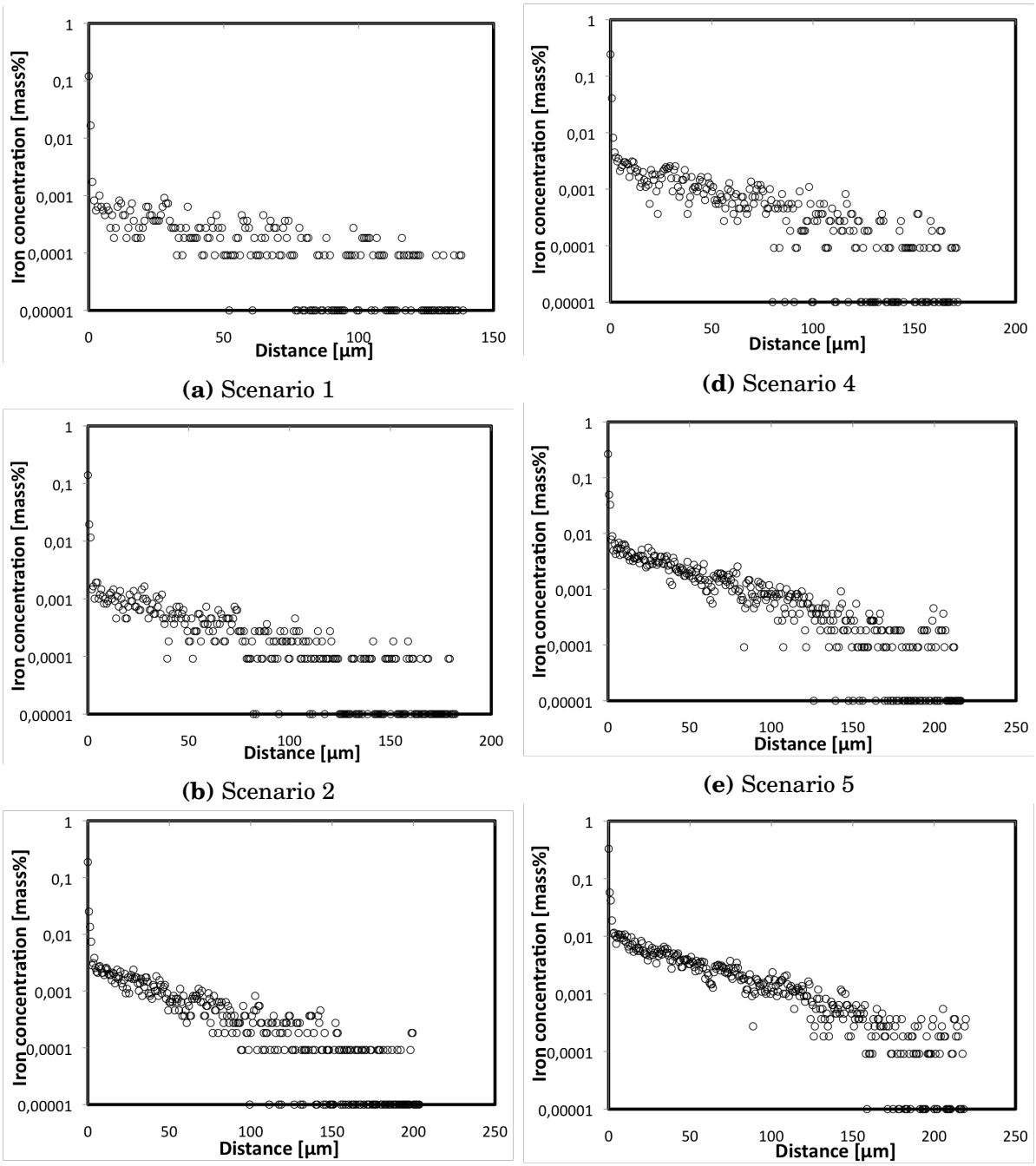

(a) Scenario 1

(d) Scenario 4

(b) Scenario 2

(e) Scenario 5

(c) Scenario 3

(f) Scenario 6

Figure 4.12: Shows the diffusion profiles from the six different scenarios obtained from sample C.1100.17.1. The scenarios in the first columns (a, b, c) have the solubility adjustment of 0,5 mass%. The second column (c, d, f) has the solubility adjustment of 0,8 mass%. The first, second and third row have the noise acceptance adjustment of 0, 1, and 2, respectively.

Table 4.3: Shows the mapping diffusivity. The corresponding sample name, contrast adjustment, scenario, solubility limit, noise acceptance are presented.

Sample	Max mass%	Scenario	Solubility	Noise accept	D[m^2/s]
C.1100.17.1	70	1	0,5	0	-
		2	0,5	1	$1{,}79\times10^{-14}$
		3	0,5	2	$1{,}77\times10^{-14}$
		4	0,8	0	$1{,}98\times10^{-14}$
		5	0,8	1	$2{,}29\times10^{-14}$
		6	0,8	2	$2{,}60\times10^{-14}$
	20	6	0,8	2	$3{,}46\times10^{-14}$
	10	6	0,8	2	$3{,}64\times10^{-14}$
C.1200.7.1	70	1	0,5	0	-
		2	0,5	1	-
		3	0,5	2	$8{,}93\times10^{-14}$
		4	0,8	0	$9{,}21\times10^{-14}$
		5	0,8	1	$7{,}63\times10^{-14}$
		6	0,8	2	$8{,}65\times10^{-14}$
	20	6	0,8	2	$1{,}44\times10^{-13}$
	10	6	0,8	2	$1{,}18\times10^{-13}$
C.1300.3.1	70	1	0,5	0	-
		2	0,5	1	$1{,}62\times10^{-13}$
		3	0,5	2	$1{,}48\times10^{-13}$
		4	0,8	0	$1{,}18\times10^{-13}$
		5	0,8	1	$1{,}46\times10^{-13}$
		6	0,8	2	$1{,}32\times10^{-13}$
	20	6	0,8	2	$2{,}01\times10^{-13}$
	10	6	0,8	2	$1{,}55\times10^{-13}$

The diffusivities of Scenario 6 at the three temperatures, in which the maximum intensity of the image corresponded to 70 mass% are collected in Table 4.4. The diffusivities are plotted against temperature in Figure 4.13.

Table 4.4: Shows the diffusivities of Scenario 6 at the three temperatures, in which the maximum intensity of the image corresponded to 70 mass%.

T[°C]	t[h]	Line scan	D[m^2/s]
1100	17	C.1100.17.1.1	$2{,}60\times10^{-14}$
1200	7	C.1200.7.1.1	$8{,}65\times10^{-14}$
1300	3	C.1300.3.1.1	$1{,}32\times10^{-13}$

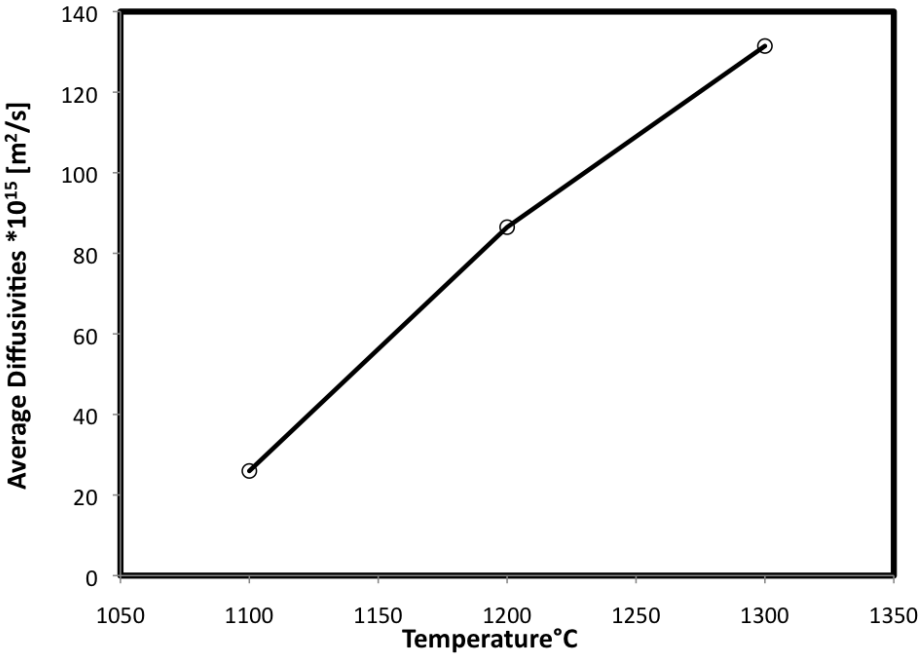

Figure 4.13: Shows the diffusivities of Scenario 6 at the three temperatures, in which the maximum intensity of the image corresponded to 70 mass%.

Chapter 5

Discussion

Due to suggested improvements in previous work by the author [35], adjustments were made to the method in the present work. In the present work, the method of sample preparation was modified in order to obtain improved sample contact in the diffusion couples. Heat treatments at 1300 °C have also been performed, which is 100 °C higher than the maximum temperature reached in previous work. In present work, the diffusivity in an actual slip-cast crucible material have been estimated in addition to the quartz glass. The actual slip-cast crucible material is more challenging to investigate due to its porosity as described in Section 4.2. The assumptions in previous work were also tested in present work. The original assumptions of this work were the following:

1. The iron oxide phase is formed in the beginning of the heat treatment and is constantly present as an infinite iron source on the sample surface during the heat treatment. Line scans should therefore be performed across the surface iron oxide phase and infinite source conditions can be applied.

2. The diffusion coefficient, D, should be independent of time, t, and concentration, C. The samples heat treated at longer holding times at the same temperature should give flatter slopes the longer the heat treatments. However, the resulting diffusion coefficients should be the same for the same temperatures.

5.1 Analysis of Quartz glass

How quickly the iron oxide phase was formed on the sample surface was investigated by heat treating the samples for a short period of time as described in Section 4.1. The phase could be detected on the sample only heat treated for 10 minutes, which is considered a negligible time compared to the duration of the heat treatments. Considering the phase as an infinite source from the beginning of the heat treatment, was from these results considered a reasonable assumption. This supports the assumption 1. As can be seen from the EDS results in Figure 4.2, the phase that forms on the surface is indeed a phase of high iron content. Presence of oxygen in this phase can be

detected as well as a small amount of silicon. Both the EDS and the EPMA analysis detected that iron was the element present in the largest concentration in this area. The composition matches the phase composition of Fayalite, Fe_2SiO_4, approximately. XRD analysis was performed on sample Qr.1280.3.1 in order to determine the phase composition, as described in Section 4.1. The XRD analysis did not detect any crystalline phase of this composition, nor of any iron oxide. However this does not indicate that no such phase is present. It indicates that no such *crystalline* phase is present or that the crystallites might have been to small for detection.

Even though samples heat treated at 10 and 30 minutes, Qr.1100,0,17.1 and Qr.1100,0,5.1, contained the iron oxide phase, cross sections with no iron oxide phase were detected. This was the case for sample surface of Qr.1100.3.1.3. Even though an improvement of contact between the diffusion couples was attempted, there were still variations in the surface phase, regarding thickness and formation. A difference in continuity of iron oxide layer can be observed from the two images of the sample heat treated at 1100 and 1300 °C, Figure 4.1a and Figure 4.1b, respectively. At higher temperatures the formation of the phase was generally more patched and less continuous. In case of patched layer formation, line scans were performed starting in a iron oxide precipitate at the interface, as can be seen in Figure 4.1b.

At 1200, 1280 and 1300 °C there were samples that were difficult to analyse and gave scattered concentration profiles. This was most likely because of larger amount of cracks in the area of precipitates described as part 3 in Figure 4.4, after heat treatment at higher temperatures. The cracks were only visible when the cross sections were magnified in SEM. The cracks makes the EPMA analysis more problematic. There can be several reasons why there were a larger amount of cracks, in samples heat treated at the higher temperatures. Securing sample with Kanthal wire may in some cases have caused cracks. It is reasonable to assume that the steel has expanded slightly during heat treatment which can have contributed to cracks during heat treatment. Cracks can also have been introduced during sample preparation for analysis. The cracks introduced during heat treatment are more problematic than the ones introduced during sample preparation. This is because crack formation during heat treatment can have affected the iron diffusion, since iron can diffuse in cracks. Cracks can also have been introduced because of phase transformation in fractions of the glass during heat treatment. Cristobalite undergoes a volume reduction during cooling that can cause internal cracks in the samples as described in Section 2.4.1.

Crystalline phases were detected in sample Qr.1280.3.1 that had been heat treated at 1280 °C for 3 hours. The three peaks in Figure 4.3 correspond to synthetic cristobalite and quartz. At higher temperatures β- cristobalite formation is possible at shorter times.

5.1.1 Diffusion coefficients

The diffusivity values in Table 4.1 and Figure 4.7 follow the expected trend when the averages of the diffusivity values at 1100 and 1300 °C are considered. The expected trend is that the diffusivity values incerase with temerparture. The average diffusivity at 1100 °C is a little higher than expected, although within the expected order of magnitude compared to previous work. It was unexpected that there was an order of magnitude difference in the samples heat treated at 1100 degrees. It also was unexpected that the slowest average diffusivity was obtained from the 1200 °C samples. The average solubility of 0,4 mass% was a little lower than the solubility obtained from previous work of 0,5 mass%. The solubility at 1200 and 1300 °C showed lower solubility. The variations in the values of diffusivity and solubility indicate that the contact has not improved significantly, or that the contact is not the cause of the variations. The patched iron oxide phase at 1200 °C and 1300 °C and large areas of precipitates might have complicated the method of estimating the solubility by extrapolation. Hence, the method for estimating solubility requires further development.

Several samples were heat treated at 1100 °C in order to gain better statistics and to investigate the assumption of no time dependence (assumption 2). Theoretically, all the diffusion profiles obtained from samples heat treated at the same temperature at different times should give similar diffusion coefficients. The average diffusivities heat treated at 1100 °C at 3, 5, 7, 15 and 17 hours are presented in Figure 5.1. The diffusivity obtained from the samples heat treated at only 3 hours are higher than the rest. The immediate observation is that diffusivity slows down with time, however the average diffusivity at 7 hours is slower than the average at 15 hours. The average diffusivity at 17 hours is the slowest. According to Section 2.4.1, cristobalite devitrification can occur at 1100 °C at longer heat treatments. Diffusion in crystalline structures is considered to differ from the diffusion in amorphous silica according to Section 2.5.4. This indicates that the assumption of time independence of the diffusion coefficient should be further investigated in conjunction with crystallisation of amorphous silica over time at 1100 °C.

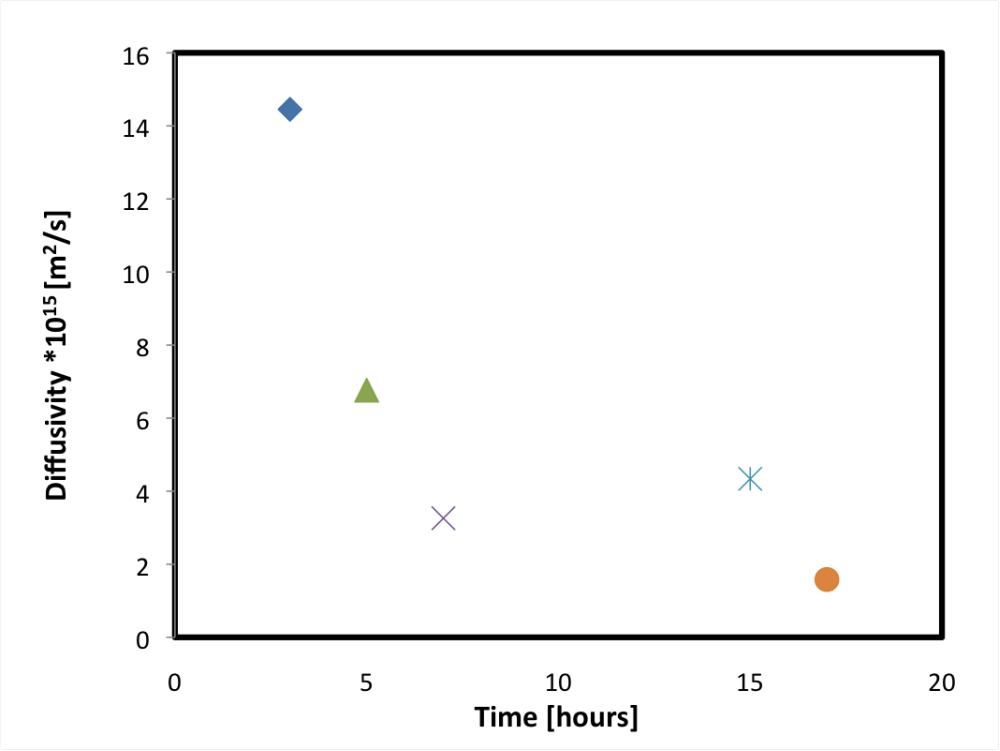

Figure 5.1: Shows average diffusivities heat treated at 1100 °C at 3, 5, 7, 15 and 17 hours.

The *Arrhenius* plots are obtained according to theory from Section 2.5.1 and 2.5.2. The deviations from the expected trend are continued in the *Arrhenius* plots. Figure 5.2 and 5.3 are the *Arrhenius* plots of the average diffusion coefficients and solubilites, respectively. The temperature independent diffusion coefficient, D_0, and activation energy of the diffusion, E_a, were obtained from the linear regression y = -0,54× -28,97, and are presented in Equations 5.1.1 and 5.1.2. The diffusivity, D, is expressed in Equation 5.1.1 with D_0, E_a and the Universal gas constant [J/molK]. The diffusivity, D, is expressed in Equation 5.1.2 with D_0, E_a and the *Boltzman* constant [eV/K]. The temperature independent solubility pre-exponential, S_0, as well as the solution enthalpy, H_S, were quantified from the linear regression y= 0,66× -5,79, and are presented in the Equations 5.1.3 and 5.1.4. The solubility is expressed in Equation 5.1.3 with S_0, H_S and the Universal gas constant [J/molK]. The solubility is expressed in Equation 5.1.4 with S_0, H_S and the *Boltzman* constant [eV/K]. The expressions for diffusivity and solubility are given in m^2/s and mass%, respectively.

$$D = 2,6 \times 10^{-13} \exp(-\frac{44,9 \text{kJ/mol}}{RT}) \tag{5.1.1}$$

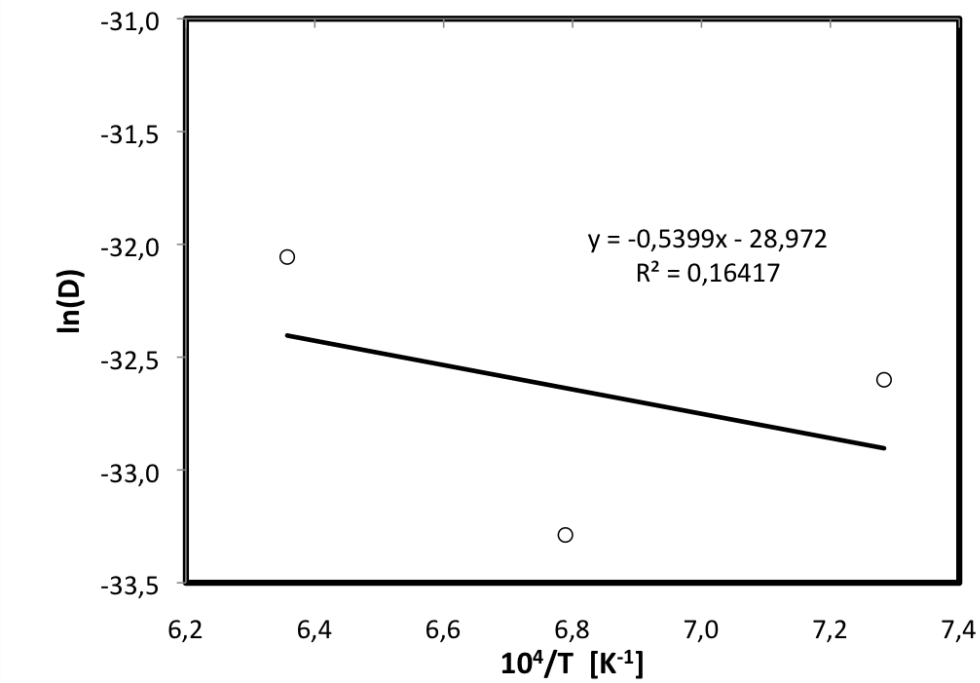

Figure 5.2: Plot of ln(D)from the quartz glass as a function of inverse temperature, and the linear regression

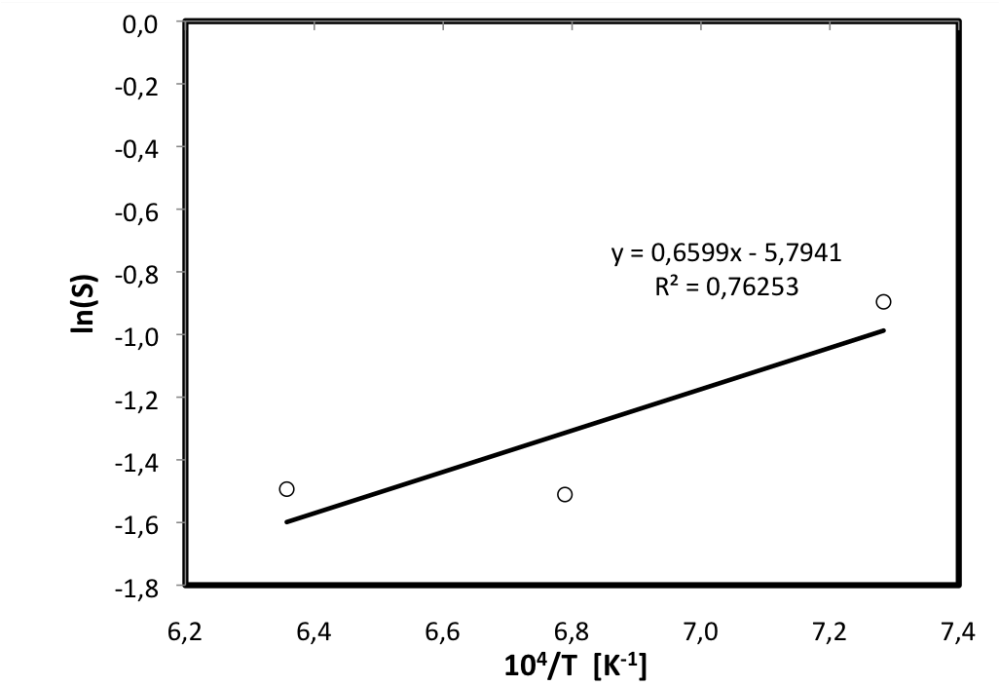

Figure 5.3: Plot of ln(S) as a function of inverse temperature, and the linear regression

$$D = 2,6 \times 10^{-13} \exp(-\frac{0,5\text{eV}}{\text{k}T}) \tag{5.1.2}$$

$$S = 1,3 \times 10^{-3} \exp(-\frac{-66,3\text{kJ/mol}}{\text{R}T}) \tag{5.1.3}$$

$$S = 1,3 \times 10^{-3} \exp(-\frac{-0,7\text{eV}}{\text{k}T}) \tag{5.1.4}$$

5.1.2 Reproducibility

The assumption 1 was supported with the EDS results, although samples that deviated from this assumption occurred. The varying degree of precipitate formation might also have affected the results as explained earlier. The investigation of assumption 2, showed deviations that indicates that it is important to look further into the crystallisation during heat treatment. The crystallisation of quartz glass introduces a level of uncertainty both in terms of estimating diffusivity and solubility. The area on how iron affects the amorphous silica crystallisation is not well explored in the literature. Because of the investigation of the time dependence there are more statistics of diffusivity at 1100 °C. The average diffusivity at 1200 °C could possibly have been higher with more statistics. Even though deviations have been observed, it is reasonable to assume that the method works and gives reliable results. The diffusivity were consistent within two orders of magnitude and showed the expected trend compared to previous work by the author. It is therefore assumed to be a sufficient method of obtaining approximate diffusivity of iron in quartz glass. More statistics are however required to estimate the parameters with higher certainty. Three values in an *Arrhenius* graph shows a good indication of the trend. However, the amounts of values (temperature intervals) in order to obtain a linear regression with high certainty requires several points.

5.2 Analysis of Crucible material

From the secondary electron micrograph of the crucible material cross section, it can be seen that the material is porous and contains pores and grains. This is unlike a smooth glass surface without any visible porosity, as in the case of Heraeus quartz glass. This is supported by the measurements of volume density and average amount of grains per distance, compared to the measured volume density of Heraeus quartz glass which gives a much higher density. The average iron concentration from the crucible samples, obtained from ICP-MS, is 43,7 ppm wt. The iron concentration is

highest in the middle of the crucible for both research series. All the crucible samples in this work were cut from the inside part of the crucible. The concentration is considered to be low enough to not affect the diffusion experiments of this work, where iron is diffused into the samples in high concentrations.

The differences in the mapping intensities, given in Figure 4.10, should not give significant differences in the result as the concentration scale bar adjusts to the increase in contrasts. However, it was observed a larger risk of introducing noise in the image by increasing the contrast, and therefore the 70 mass% scale was chosen. When analysing the results of the X-ray mapping it is important to keep in mind that the analysis is only semi-quantitative. The intensity to mass% scale functions as an approximate guide. The reason for adjusting the maximum intensity of the scale bar to 20 mass% and 10 mass% in the two other images, was to compare images with a large difference in contrast adjustment. This was to investigate if the contrast adjustments were dominating the results. As can be understood from the Equation 3.3.1, the adjustment of the contrast should give more values below the solubility limit, however not affect the curve of the diffusion profile. This is explained further in Appendix A.

In Figure 4.12 it can be observed that the concentration profiles becomes more continuous with larger noise acceptance for both solubilities. The profile is more continuous for 0,8 mass% than 0,5 mass%. The tolerance of 0,3 mass% as well as noise acceptance were introduced as measures in order to avoid valid values being excluded. The value of the noise acceptance was chosen because it was considered unlikely that two subsequent concentrations above the solubility limit, midst a concentration profile of values below the solubility limit, could actually represent a precipitate. From Table 4.3 it can be observed that the diffusivities at 1100 °C are lower than the ones at 1200 °C, which in turn are lower than the diffusivities at 1300 °C. There is one exception being the diffusvivity obtained from sample C.1200.5.1, with maximum intensity 20 mass%. This diffusivity at 1200 °C is higher than two of the diffusivities at 1300 °C. A difference between the values from each scenario and between the values obtained from 70 mass%, 20 mass% and 10 mass% can be observed. A general trend, with increasing diffusivity with temperature, can however be observed regardless of contrast and scenario. Since the contrast and script adjustments did not change the overall trend of the results, this work has proceeded with images at 70 mass% maximum intensity combined with the scenario 6, since this was considered the most trustworthy results at each temperature. Hence, the values in Table 4.4 have been used in the rest of the

work.

The *Arrhenius* plot in Figure 5.4 is obtained according to theory from Section 2.5.1. The temperature independent diffusion coefficient, D_0, and activation energy of the

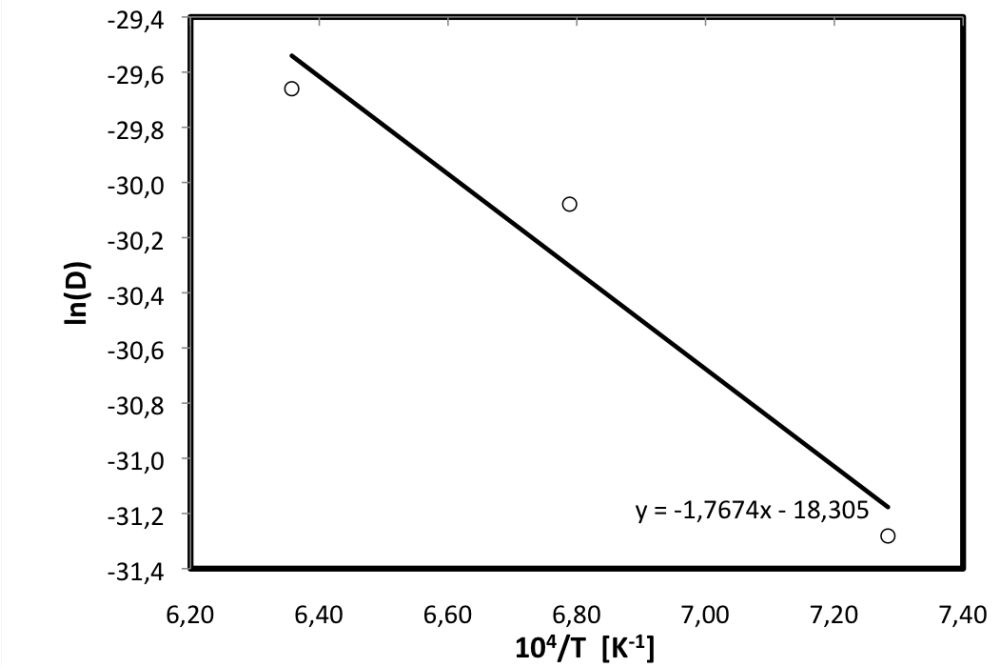

Figure 5.4: Plot of ln(D)from the crucible as a function of inverse temperature, and the linear regression.

diffusion, E_a, were obtained from the linear regression y = -1,77× -18,31, and presented in Equations 5.2.1 and 5.2.2. The diffusivity, D, is expressed in Equation 5.2.1 with D_0, E_a and the Universal gas constant [J/molK]. The diffusivity, D, is expressed in Equation 5.2.2 with D_0, E_a and the *Boltzman* constant [eV/K]. The diffusivity is given in m^2/s.

$$D = 1,2 \times 10^{-8} \exp(-\frac{146,7\text{kJ/mol}}{\text{R}T}) \tag{5.2.1}$$

$$D = 1,2 \times 10^{-8} \exp(-\frac{1,52\text{eV}}{\text{k}T}) \tag{5.2.2}$$

5.2.1 Reproducibility

As mentioned, the semi-quantitative X-ray technique is not a 100% quantitative. This has affected the concentration scale in Figure 4.13 which is believed to be lower than

reality. The solubility limit was therefore set to a very approximate value. The crucible material is too porous for the quantitative X-ray technique, which would have given more accurate concentrations. However, it is reasonable to assume that the relationship between the concentrations obtained from semi-quantitative X-ray mapping is sufficient to obtain a trustworthy diffusion trend. The right order of magnitude and the correct trend of the diffusion constants are believed to be found and the method created is believed to be valid. Values from more than one sample at each temperature is required to determine the diffusivity with higher certainty. The same uncertainties that is described in section 5.1.2 regarding crystallisation of quartz glass, also applies in the case of the crucible material. More temperatures values are also required to obtain a more accurate trend from the *Arrhenius* plot.

5.3 Comparison to literature

The diffusion coefficients found in this work are plotted as a function of inverse temperature in Figure 5.5. The values have also been compared to literature values. The diffusivities from Table 2.2 are plotted within the temperature interval of the corresponding study. The actual diffusivity at each temperature obtained in this work are marked as points in the Figure. The activation energy is estimated to be much higher in the crucible than in the quartz glass. Because of the deviation from the temperature trend, the average diffusivity at 1200 °C for quartz glass causes the slope of the *Arrhenius* curve to be less steep. However, in theory, there is no reason that the activation energy for iron diffusion should be higher than in the quartz glass. The diffusivity of quartz glass obtained in this work is an order of magnitude lower than in the crucible. The values of diffusivities lies within a reasonable interval, between values obtained from literature.

As explained in Section 2.5.4, Schubert's study is the only one of the studies described which has looked at a crucible material. It can be seen from Figure 5.5 that the values for the diffusivity in the crucible match well with Schubert's diffusivities. The slope is steeper in Schubert's estimations. Schubert has used Istratov's activation energy, therefore it can be observed that these curves have the same slopes. Another activation energy would have changed the slope of Schubert's curve. The quartz glass diffusivities in this work are considerably higher than Atkinson, Kononchuc and Ramappa's estimations for amorphous silica with dense structures.

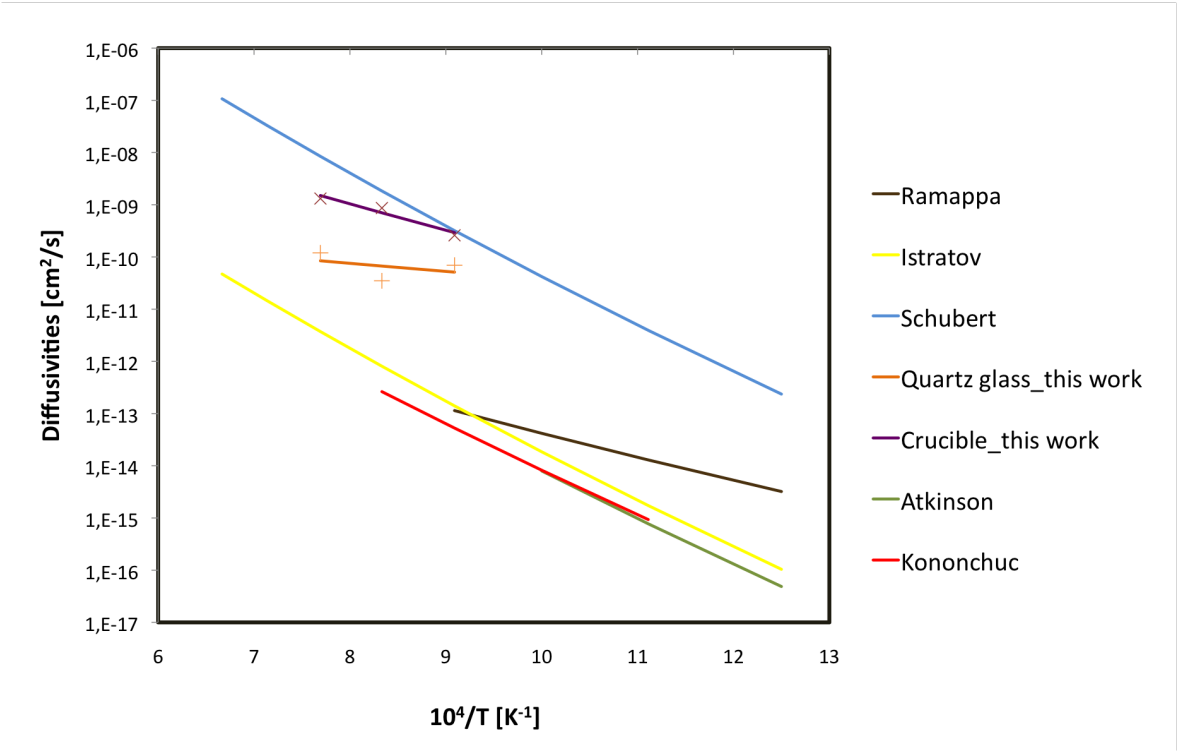

Figure 5.5: Comparison of the diffusivities obtained from literature [2, 5–8] and this work

The Figure indicates that the crucibles made of quartz glass should experience considerably faster diffusion than expected from literature values. This Figure also indicates that it is important to account for the structure of the amorphous silica in order to estimate the diffusivity in a particular system.

5.4 Simulation

In the model, described in Section 3.3.3, iron diffuses from the crucible and coating into the melt during the melting stage. The approximate iron concentration in the silicon melt was estimated. Both the quartz glass and the actual slip-cast crucible were used as the crucible material in order to compare the influence of the two materials on the contamination of the silicon melt. By applying the Scheil equation, to the iron concentration in the melt, the iron concentration at different positions in the ingot could be obtained. The different scenarios are given in Table 5.1. The concentration in the melt and in the solid ingot have been estimated from each scenario. The Crucible type indicates if the diffusivity values used in the model is taken from the obtained values of quartz glass or slip-cast crucible in this study. The iron concentrations in the melt

and in the ingot are given as a function of position in the ingot in Figure 5.6. The position in the ingot is given as a percentage of distance from the bottom to the top, where 0 is the bottom an 1 is at the top.

Table 5.1: The iron concentrations in the melt and in the ingot are given as a function of position in the ingot for the different scenarios

Scenario melt	Scenario solid	Crucible type	Crucible standard	Coating quality
$C_0(1)$	C(1)	slip-cast	regular	regular
$C_0(2)$	C(2)	slip-cast	regular	pure
$QA_0(1)$	QA(1)	quartz glass	regular	regular
$QA_0(2)$	QA(2)	quartz glass	regular	pure
$QA_0(3)$	QA(3)	quartz glass	high purity	pure

In order to investigate if the poor *Arrhenius* fit (Figure 4.7) of the quartz glass influenced the modelling results, some adjustments were made to the diffusivity values. A scenario was created, where the diffusivities of the shortest heat treatment at 1100 °C were excluded. The new *Arrhenius* graph resulted in a more accurate fit and the resulting parameters were used in the model. However, the results became extremely similar to the values of quartz glass, and the curves of the corresponding scenarios of quartz glass overlapped in Figure 5.6. Hence, the consequence of the poor fit did not have a large influence on the simulation.

The concentration of iron in the ingot centre in the case of the slip-cast crucible with regular coating (Scenario C1) amounted to $1{,}65\times10^{10}$ cm^{-3}. Schubert's estimations for the iron concentration estimated in a G4 ingot was $3{,}2\times10^{10}$ cm^{-3} [2]. Schubert's model also accounts for contamination of the melt during solidification, and a factor of two in difference between the model in this work and Schubert's model can be expected. The iron concentration obtained in the high purity crucible scenario (QA(3)) which amounts to $4{,}8\times10^{9}$ cm^{-3} also corresponds (if multiplied with the factor two) to the concentration found in the Schubert study, which was $0{,}89\times10^{10}$ cm^{-3}. The values obtained in this study therefore indicates that the model used in this study works.

The scenarios with the regular crucible and coating, (C(1) and QA(1)), gave the two

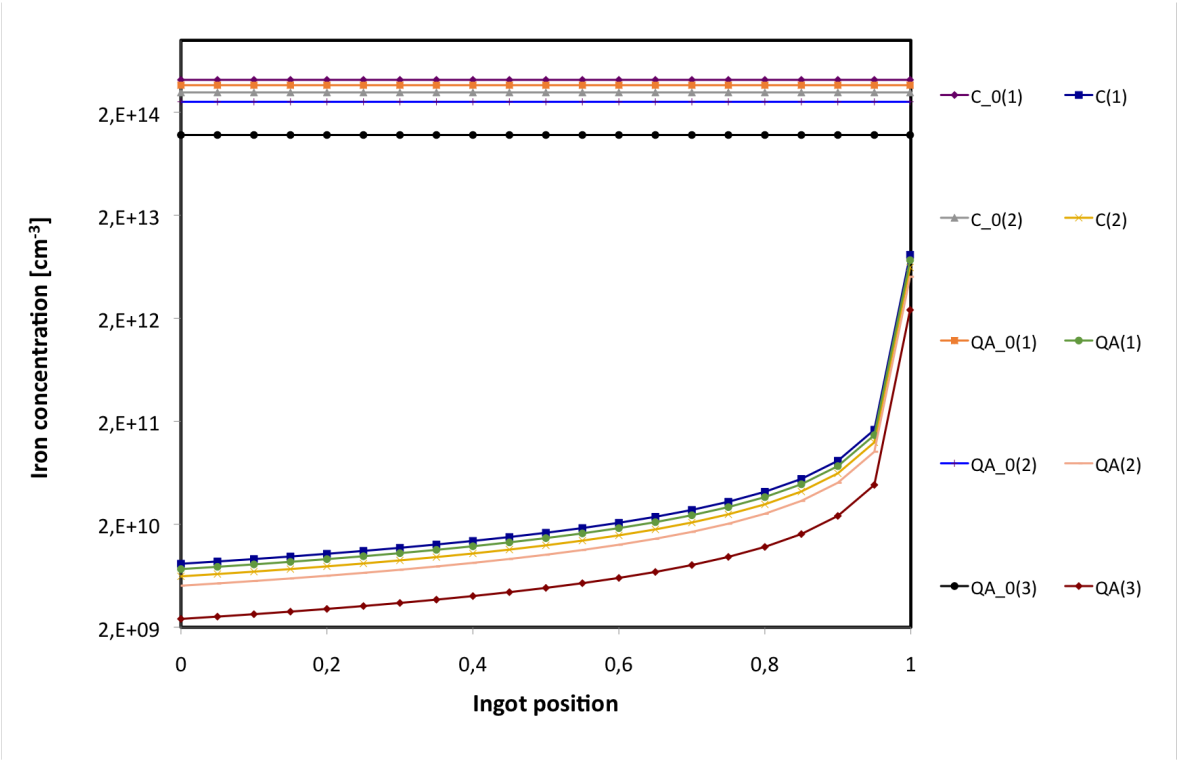

Figure 5.6: Iron concentrations in the melt and in the ingot given as a function of position in the ingot

highest concentrations curves of iron in the solid. The concentration from the slip-cast crucible is a little higher than from the quartz glass crucible. The difference in iron concentration between the scenarios with pure coating and regular coating was expected to be larger. A larger difference from the rest of the curves can be observed in the scenario with high a purity quartz glass crucible with pure coating, (QA(3)). This indicates that the impurity level of the crucible is important.

It was unexpected that the two different crucible types did not give a larger difference in iron concentration in the silicon, given the results obtained from the difference that can be seen from the plots in Figure 5.5. The results from 5.6 do not indicate that the structure differences of the materials used as crucibles result in a significant difference in iron concentration. However, it is reasonable to assume that a material structure that is less porous, should reduce the contamination. It is also reasonable to assume that if the high purity coating could been further improved, a larger difference between the quartz glass and the slip-cast crucible could have been observed.

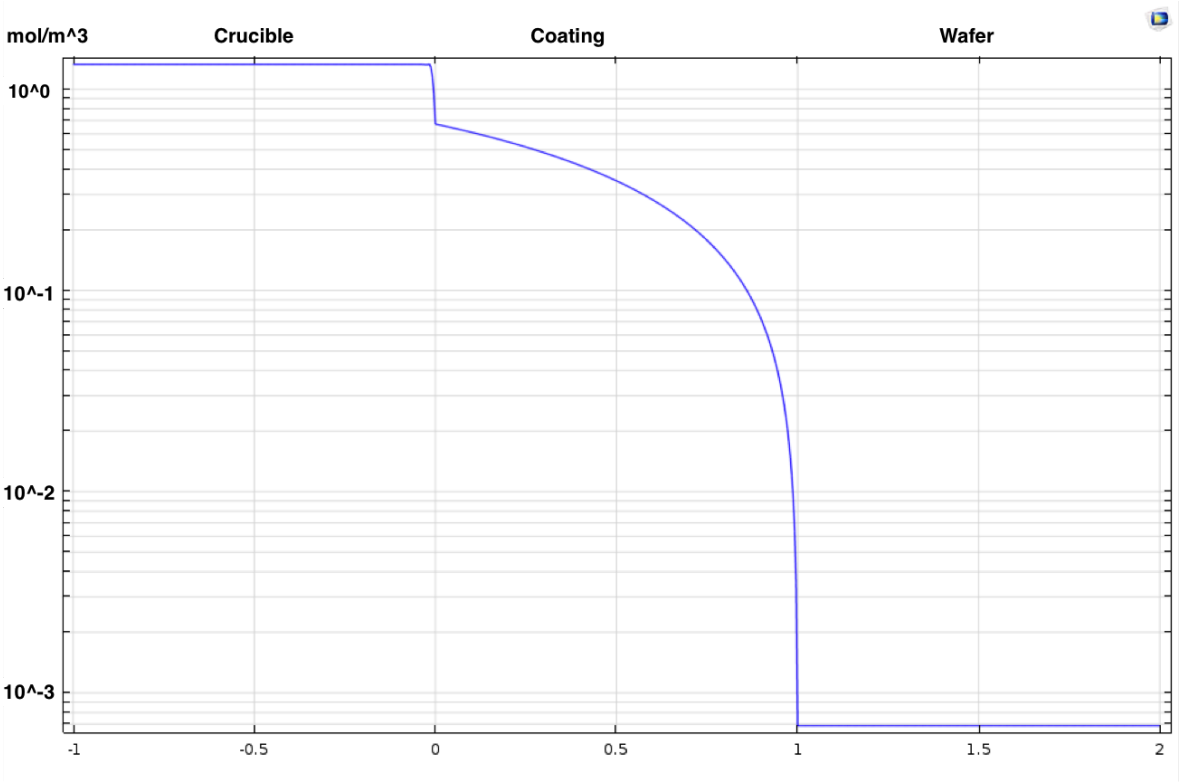

Figure 5.7: The Figure shows the concentration (mol/m^3) diffused into each media.

As can be seen from Figure 5.7 obtained in COMSOL for the modelling scenario $C_0(1)$, the diffusion profile into the crucible is very short. The Figure shows the concentration (mol/m^3) diffused into each media. Some model modification must also be performed, as the shape of the concentration curve into the coating should be the shape of a diffusion curve. Based on the model, a suggestion to the industry could be to make a slip-cast crucible, with a thin denser quartz glass layer on the inside of the crucible, and use cleaner coating. However modifications to the model must be performed and more studies should be performed to determine this with certainty.

Chapter 6

Conclusion and further work

The motivation of this work was to investigate the behaviour of the slip-cast crucible as a contamination source of multicrystalline silicon. Two methods have been developed in order to investigate iron diffusion in both quartz glass and a slip-cast crucible material. The method for obtaining solubility and diffusivity of iron in quartz glass has been modified, according to suggestions from previous work by the author. A method for estimating iron diffusivity in the slip-cast crucible was created.

The diffusivity of iron in quartz glass was estimated to be on the order of 10^{-15} and 10^{-14} m^2/s over the range of 1100-1300 °C. The diffusivity of iron in the quartz at 1100 and 1300 °C showed the expected temperature dependence in terms of diffusion increasing with temperature. The average diffusivity at 1100 °C was within the expected order of magnitude compared to previous work by the author. It was unexpected that the slowest diffusivity was obtained from the 1200 °C samples. The average solubility of 0,4 mass% was a little lower than the solubility obtained from previous work of 0,5 mass%. The solubility at 1200 and 1300 °C was estimated to be lower than the average one at 1100 °C, which was unexpected. The method of obtaining solubility at higher temperatures most likely needs further development. The diffusivity of iron in the crucible material was estimated to be on the order of 10^{-14} and 10^{-13} m^2/s over the range of 1100-1300 °C. In the crucible material, an approximate value of solubility of 0,5 mass%, with a 0,3 mass% tolerance, has been used. The diffusivity in the crucible material increased with temperature. The diffusivity of quartz glass and the slip-cast crucible can be expressed in terms of the *Arrhenius* equation in m^2/s, respectively.

$$D = 2,6 * 10^{-13} \exp(-\frac{44,9 \text{kJ/mol}}{\text{R}T}) \tag{6.0.1}$$

$$D = 1,2 * 10^{-8} \exp(-\frac{146,7 \text{kJ/mol}}{\text{R}T}) \tag{6.0.2}$$

There was an order of magnitude difference between the diffusivity of iron in the quartz glass and in the slip-cast crucible, and the diffusivity was higher in the crucible material. The crucible diffusivity supports Schubert's estimations. The estimated

quartz glass diffusivity indicate that crucibles made out of these materials should experience considerably faster diffusion than expected from literature values. The model used in this study was verified by comparing the results to the results of Schubert's modelling. The simulation resulted in a very similar iron contamination from the quartz glass crucible and the slip-cast crucible. It is reasonable to assume if the simulation had been tested with even cleaner coating, a larger difference could have been observed. More statistics are required for the diffusivity of the slip-cast crucible and more investigation should be performed on the time dependence of the diffusion coefficient, as well as crystallisation of amorphous silica at 1100°C-1300°C.

Bibliography

[1] REN21. 2016. Renewables 2016 Global Status Report (Paris: REN21 Secretariat). ISBN 978-3-9818107-0-7. Technical report.

[2] M. C. Schubert, J. Schon, F. Schindler, W. Kwapil, A. Abdollahinia, Bernhard. Michl, Stephan. Riepe, C. Schmid, M. Schumann, S. Meyer, and W. Warta. Impact of Impurities From Crucible and Coating on mc-Silicon Quality-the Example of Iron and Cobalt. *IEEE Journal of Photovoltaics*, 3(4):1250–1258, oct 2013.

[3] R. Kvande, L. Arnberg, and C. Martin. Influence of crucible and coating quality on the properties of multicrystalline silicon for solar cells. *Journal of Crystal Growth*, 311(3):765–768, jan 2009.

[4] E. Olsen and E. J. Øvrelid. Silicon Nitride Coating and Crucible- Effects of Using Upgraded Materials in the Casting of Multicrystalline Silicon Ingots. *Progress in Photovoltaics: Research and Applications*, 16(2):93–100, mar 2008.

[5] D. A. Ramappa. Diffusion of Iron in Silicon Dioxide. *Journal of The Electrochemical Society*, 146(10):3773–3777, oct 1999.

[6] A. A. Istratov, W. Huber, and E. R. Weber. Gettering Strategies for SOI Wafers. *Solid State Phenomena*, 95-96:547–552, 2004.

[7] A. Atkinson and J.W. Gardner. The diffusion of Fe3+ in amorphous SiO2 and the protective properties of SiO2 layers. *Corrosion Science*, 21(1):49–58, jan 1981.

[8] O. Kononchuk, K. G. Korablev, N. Yarykin, and G. A. Rozgonyi. Diffusion of iron in the silicon dioxide layer of silicon-on-insulator structures. *Applied Physics Letters*, 73(9):1206, 1998.

[9] W. C. O'Mara, R. B. Herring, and L. P Hunt. *Handbook of semiconductor silicon technology*. Noyes Publications, Park Ridge, N.J., 1990.

[10] G. Bye and B. Ceccaroli. Solar grade silicon: Technology status and industrial trends. *Solar Energy Materials and Solar Cells*, 130:634–646, 2014.

[11] Fraunhofer Institute for Solar Energy and ISE Systems. Presentation: Photovoltaics report, Freiburg, 6 June, 2016.

[12] G. Coletti. Sensitivity of state-of-the-art and high efficiency crystalline silicon solar cells to metal impurities. *Progress in Photovoltaics: Research and Applications*, 21:1163–1170, mar 2012.

[13] Y. M. Yang, A. Yu, B. Hsu, W. C. Hsu, A. Yang, and C. W. Lan. Development of high-performance multicrystalline silicon for photovoltaic industry. *Progress in Photovoltaics: Research and Applications*, 23(3):340–351, mar 2015.

[14] A. Ciftja and G. Stokkan. Growth of High Performance Multicrystalline Silicon; A Literature Review. Technical report, /0/774/1500/1607/1609/, 2014.

[15] G. Stokkan, Y. Hu, Ø. Mjøs, and M. Juel. Study of evolution of dislocation clusters in high performance multicrystalline silicon. *Solar Energy Materials and Solar Cells*, 130:679–685, 2014.

[16] A. A. Istratov, T. Buonassisi, R. J. McDonald, A. R. Smith, R. Schindler, J. A. Rand, J. P. Kalejs, and E. R. Weber. Metal content of multicrystalline silicon for solar cells and its impact on minority carrier diffusion length. *Journal of Applied Physics*, 94(10):6552, 2003.

[17] D. Macdonald, A. Cuevas, A. Kinomura, Y. Nakano, and L. J. Geerligs. Transition-metal profiles in a multicrystalline silicon ingot. *Journal of Applied Physics*, 97(3):033523, 2005.

[18] G. Coletti, R. Kvande, V. D. Mihailetchi, L. J. Geerligs, L. Arnberg, and E. J. Ovrelid. Effect of iron in silicon feedstock on p- and n-type multicrystalline silicon solar cells. *Journal of Applied Physics*, 104(10):104913, 2008.

[19] K. E Ekstrøm. *Structure control of multicrystalline silicon*. PhD thesis, Norwegian University of Science and Technology, 2016.

[20] Vesuvius. Vesuvius - industrial processes - solar - SOLAR Crucible RTU- Ready To Use crucible: URL: http://www.vesuvius.com/en/end-markets/industrial-processes/solar/solarr-crucible-rtu-ready-to-use-crucible/ Accessed: 03.04.16.

[21] V. Presser and K. G. Nickel. Silica on Silicon Carbide. *Critical Reviews in Solid State and Materials Sciences*, 33(1):1–99, feb 2008.

[22] K. A. Jackson. *Kinetic Processes*. Wiley-VCH Verlag GmbH & Co. KGaA, Weinheim, FRG, jul 2004.

[23] J.F Shackelford and R.H. Doremus. *Ceramic and Glass Materials: Structure, Properties and Processing*. Springer Science & Business Media, 2008.

[24] R. Brükner. Properties and structure of vitreous silica. I. *Journal of NON-CRYSTALLINE SOLIDS, North-Holland Publishing Co*, 5:123–175, 1970.

[25] M.A. Lamkin, F.L. Riley, and R.J. Fordham. Oxygen mobility in silicon dioxide and silicate glasses: a review. *Journal of the European Ceramic Society*, 10(5):347–367, jan 1992.

[26] The Quartz Corp. Quartz glass. URL: www.thequartzcorp.com/en/applications/quartz-glass. Accesed 22.11.2015.

[27] Heraeus. Standard optics information- HOQ 310. Technical report, Heraeus Quarzglass GmbH &Co. KG, Hanau.

[28] W. D. jr. Callister and D. G. Rethwisch. *Materials Science and Engineering: An Introduction*. John Wiley & Sons Canada, Limited, 2011.

[29] J. Crank. *The Mathematics of Diffusion*. Clarendon Press, 1979.

[30] D. A. Porter, K. E. Easterling, and M. Sherif. *Phase Transformations in Metals and Alloys, Third Edition (Revised Reprint)*. CRC Press, 2009.

[31] R. J. D. Tilley. *Understanding Solids: The Science of Materials, 2nd Edition*. John Wiley & Sons, 2013.

[32] A. Myerson. *Handbook of Industrial Crystallization*. Butterworth-Heinemann, 2002.

[33] G. Coletti. *Impurities in silicon and their impact on solar cell performance*. PhD thesis, sep 2011.

[34] A. Autruffe. *Silicon directional solidification: Impurity segregation and defects*. PhD thesis, 2014.

[35] H. V. Skarstad. *Diffusivity and Solubility in Fused Quartz Crucibles*. Project thesis, Norwegian University of Science and Technology.

[36] G.A. Jenner, H.P. Longerich, S.E. Jackson, and B.J. Fryer. ICP-MS - A powerful tool for high-precision trace-element analysis in Earth sciences: Evidence from analysis of selected U.S.G.S. reference samples. *Chemical Geology*, 83(1-2):133–148, jun 1990.

[37] University of Cambridge. XRD-introduction URL:www.doitpoms.ac.uk/tlplib/xray-diffraction/intro.php Accessed 04.05.16.

[38] Materials Evaluation and Engineering INC(MEE). Energy dispersive X-ray spectroscopy (EDS). URL: http://www.mee-inc.com/hamm/energy-dispersive-x-ray-spectroscopyeds/ Accessed: 29.06.16.

[39] J. Hjelen. JEOL JXA-8500F Electron Probe Micro analyzer (EPMA). URL: www.material.ntnu.no/lab/material/equipment/ProdInfoEPMA.pdf. Accesed: 20.10.2015.

[40] COMSOL Multiphysics Modeling Software. URL:www.comsol.com, Accessed 08.12.15.

[41] A. Autruffe. Private communication, 2015.

[42] T. W. Clyne and W. Kurz. Solute redistribution during solidification with rapid solid state diffusion. *Metallurgical Transactions A*, 12(6):965–971, jun 1981.

Appendix A

Calculations

The volume density calculations performed in this work were estimated by Equation A.1.1, where V is volume and m is mass.

A.1 Density

$$\rho = m/V \tag{A.1.1}$$

A.2 Conversion from intensity to concentration

The Equation 3.3.1, applied when converting intensities into concentrations in Section 3.3.1, gives a larger amount of lower values, when the maximum intensity is 10 mass% compared to 70 mass%. The relation is given once again in Equation A.2.1.

$$\frac{(C_{max} - C_{min}) \times I}{I_{max} - I_{min}} = C_{Fe}. \tag{A.2.1}$$

If (I) is 1 and is converted into concentration (C_{Fe}) and the maximum intensity corresponds to to 70 mass% and 10 mass% ($C_{max} - C_{min}$), the iron concentration will amount to 0,27 and 0,04 mass%, respectively. Hence, a higher amount of numbers will be below the solubility limit of 0,5 mass% (with the tolerance 0,3 mass%) in the case of maximum intensity corresponding to a lower concentration. As can be seen from the graphs in Section D, the trend stays the same even though the graphs from the the 10 mass% and 20% images contain more values. As earlier explained this does not affect the estimation of the diffusion coefficients significantly.

A.3 Scheil Equation

The Scheil equation given in Equation A.3.1 is applied in this work to convert a concentration in a liquid into a concentration in a solid. C_s is the concentration in the solid, C_m is the concentration in the melt, k is the effective segregation coefficient and

f_s is the mass fraction of the melt that is solidified [42].

$$C_s = k \times C_m(1 - f_s)^{(k-1)} \tag{A.3.1}$$

Appendix B

Image analysis

B.1 MatLab script

The Matlab script applied in present work is given in this section. The scrip is explained in Section 3.3.1.

```
clear all
close all
clc
%%%Step 1: Imports image and returns the contrast matrix%%%%%
Contrast=imread('c11g2.tiff'); %%% Importing the black and white
image. You get a matrix containing contrast values ranging from 1 to
256
Contrast = double(Contrast);

%N= Number of rows in your image-i.e. pixels in the vertical
direction%
%P=%%% Number of columns in your image-i.e. pixels in the horizontal
direction

[N,P] = size(Contrast);


%disp(Contrast);

Sol=0.8; %%% Solubility limit

Cmax=70; %%% Maximum concentration in your image/on the
concentration scale
noiseAcceptance = 2;


%%%% Step 2  Convert contrast to concentration %%%%%%%%%%%%%%%%%%%%
%%%%%%%%%%%%%%%%%%%%%%%%%%%%%%%%%%%%%%%%%%%%

Concentration=zeros(N,P);

for i=1:N
    for j=1:P
        Concentration(i,j) = (Contrast(i,j)*Cmax)/256.0;
    end;
end;



%%% Step 3 : Flip concentration matrix and search each column for
concentration boundary, Zero out all values above solubility limit.
Flip the matrix back %%%%%%%%%%%%%

FlipedBoundary = zeros(N,P);
ConcentrationFliped = flipud(Concentration);

for col = 1:P
    counter = 0;
    for row = 1:N
        if ConcentrationFliped(row,col) >= Sol
            counter = counter + 1;
        else
            FlipedBoundary(row,col) = ConcentrationFliped(row,col);
        end
```

```
        if counter > noiseAcceptance
            break;
        end
    end
end



BoundaryMatrix = flipud(FlipedBoundary);

%%%% Push the columns to the top of the matrix

Dist=zeros(1,P);
NewBoundary = zeros(N,P);
for j=1:P
    for i=1:N

       if BoundaryMatrix(i,j)==0

        Dist(1,j)=Dist(1,j)+1;

        else

        break;

       end;

end;
end;


for j=1:P
    for i=1:(N-Dist(1,j))
        NewBoundary(i,j)=BoundaryMatrix(Dist(1,j)+i,j);
end;
end;
%%%%Step 4: Average the values in the each row to form one average
column

 B = mean(NewBoundary,2);
```

Appendix C

Images

C.1 Quartz glass

This section presents the rest of the backscatter images of the cross section where the line scans were performed. The line scan can be seen as a vertical line in the centre of the image. Only the cross sections that gave a diffusion profile are included. All the micrographs are obtained with the same magnification. Because of EPMA failure, cross section images were not obtained for the line scan Qr.1100.15.1.1, Qr.1200.15.1.2, Qr.1200.15.1.3.

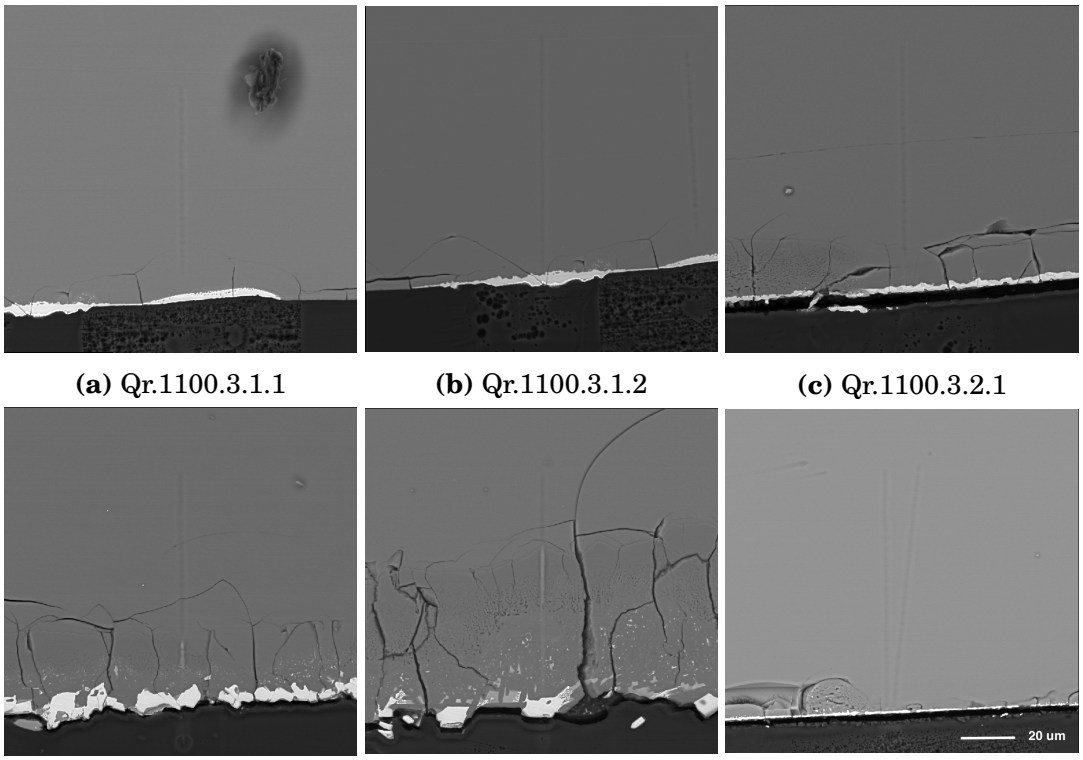

(a) Qr.1100.3.1.1 **(b)** Qr.1100.3.1.2 **(c)** Qr.1100.3.2.1

(d) Qr.1100.5.1.1 **(e)** Qr.1100.5.1.2 **(f)** Qr.1100.7.1.1

Figure C.1: Backscatter images of the cross section where the line scans were performed. The line scan can be seen as a vertical line in the centre of the image, and the line scan name is given below each figure.

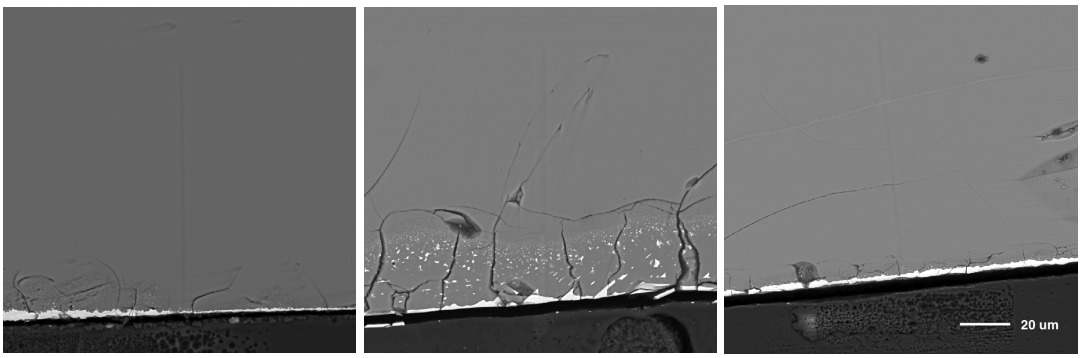

(a) Qr.1100.7.1.2 **(b)** Qr.1200.15.1.1 **(c)** Q.1100.17.1.1

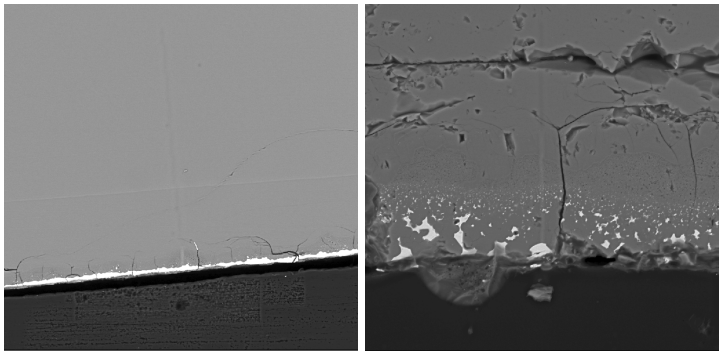

(d) Q.1100.17.1.2 **(e)** Q.1300.3.1.3

Figure C.2: Backscatter images of the cross section where the line scans were performed. The line scan can be seen as a vertical line in the centre of the image, and the line scan name is given below each figure

C.2 Crucible

This section presents the rest of the mapping images. Figure C.3 and Figure C.4 presents the mapping images from the samples heat treated at 1200 and 1300 °C, respectively. Figure C.3a, C.3b and C.3c present the X-ray mapping images of the cross section C.1200.7.1, with image maximum intensity corresponding to 70 mass%, 20 mass% and 10 mass%, respectively. Figure C.4a, C.4b and C.4c present the X-ray mapping images of the cross section C.1300.3.1, with image maximum intensity corresponding to 70 mass%, 20 mass% and 10 mass%, respectively.

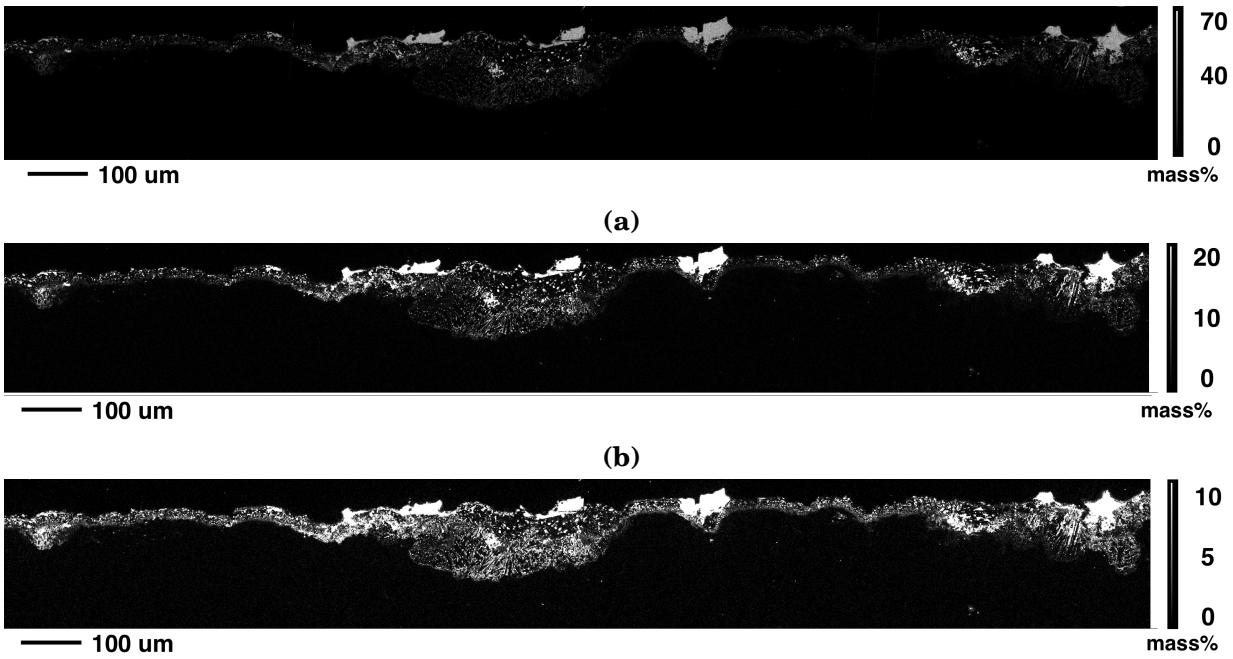

Figure C.3: Figure C.3a, C.3b and C.3c present the X-ray mapping images of the cross section C.1200.7.1, with image maximum intensity corresponding to 70 mass%, 20 mass% and 10 mass%, respectively.

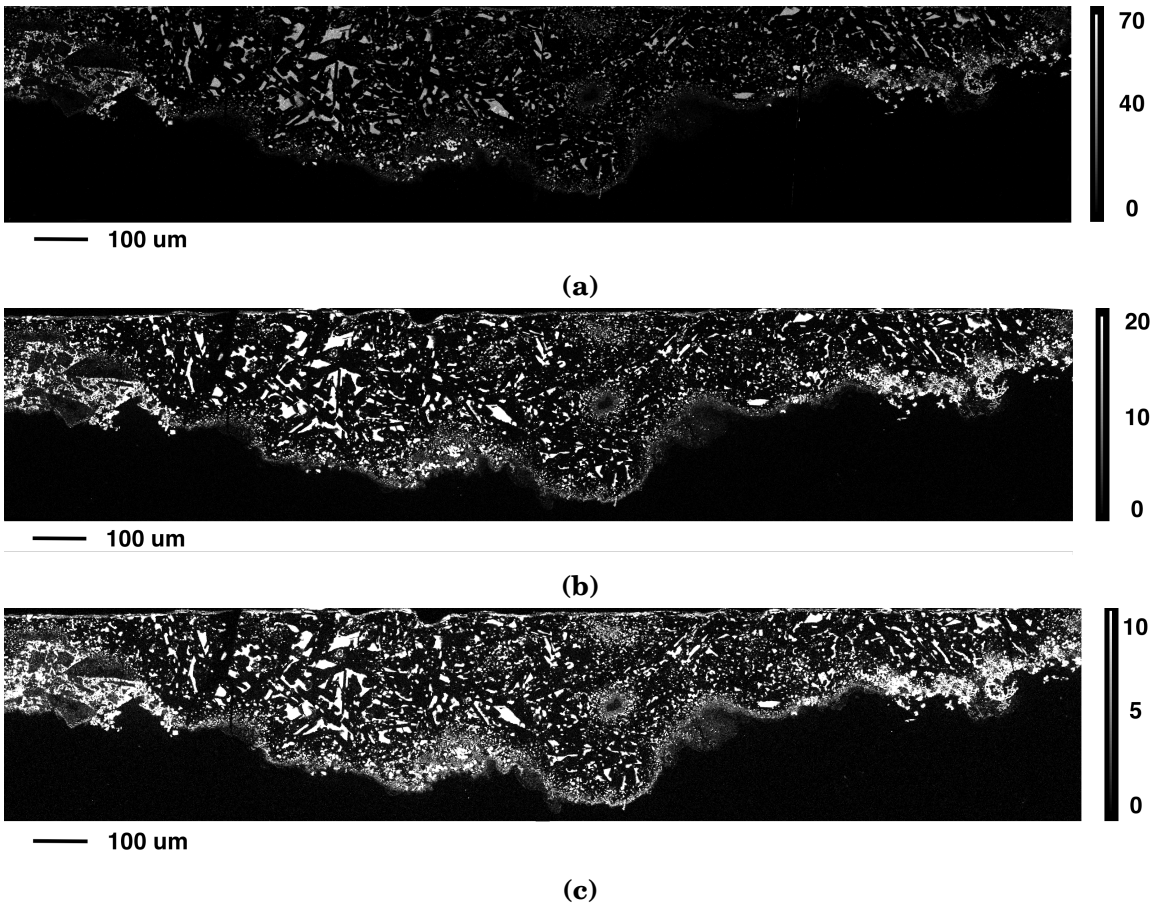

Figure C.4: Figure C.4a, C.4b and C.4c present the X-ray mapping images of the cross section C.1300.3.1, with image maximum intensity corresponding to 70 mass%, 20 mass% and 10 mass%, respectively.

Appendix D

Iron Distribution

D.1 Quartz glass

The diffusivities, D and solubilities, S, presented in Table 4.1, were obtained from the diffusion profiles presented in this section. The plots present the iron concentration as a function of distance from the high content iron oxide phase on the surface and into the quartz glass sample. The plots have been adjusted so that only the parts 2-4 (explained in Section 4.1.1) are visible. The line scans that did not show a diffuison profile were not included in this section.

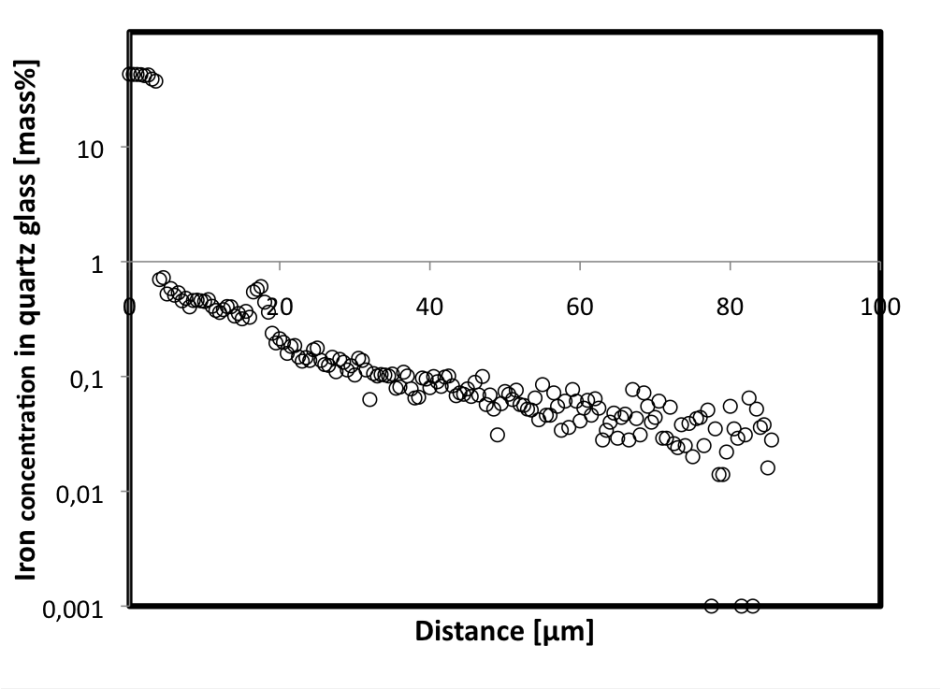

Figure D.1: Iron concentration [mass%] as a function of distance [µm] obtained from line scan Qr.1100.3.1.1

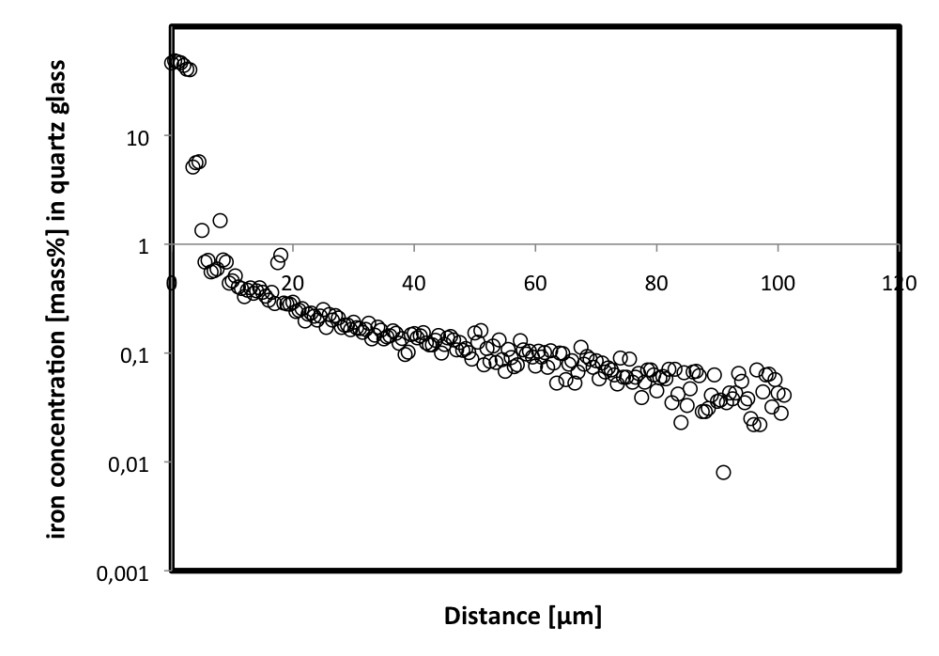

Figure D.2: Iron concentration [mass%] as a function of distance [µm] obtained from line scan Qr.1100.3.1.2

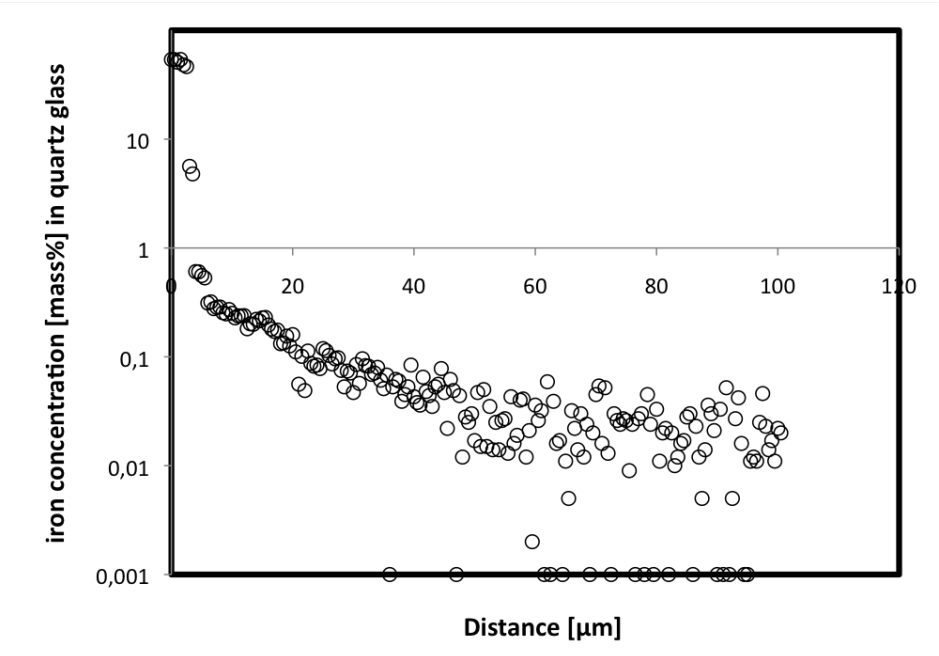

Figure D.3: Iron concentration [mass%] as a function of distance [µm] obtained from line scan Qr.1100.3.2.1

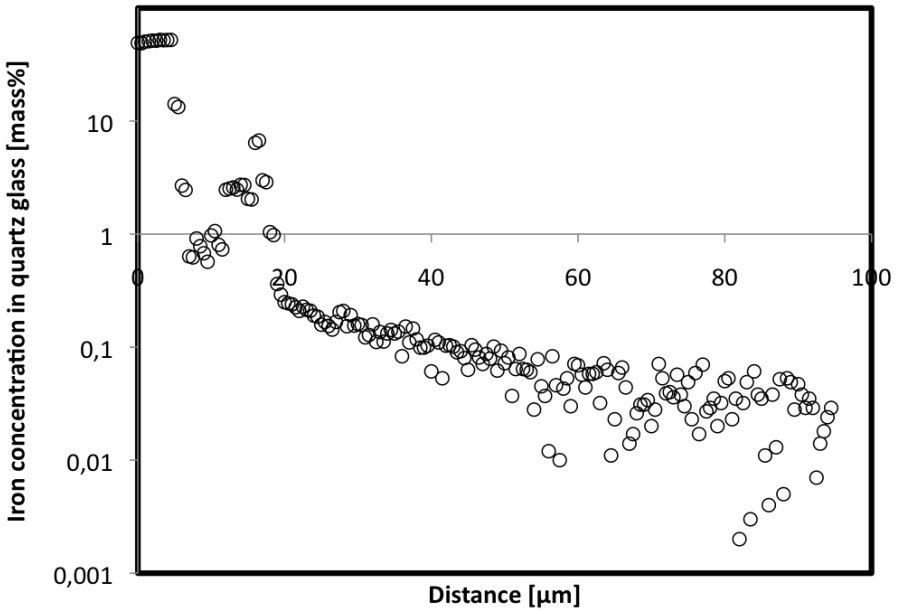

Figure D.4: Iron concentration [mass%] as a function of distance [µm] obtained from line scan Qr.1100.5.1.1

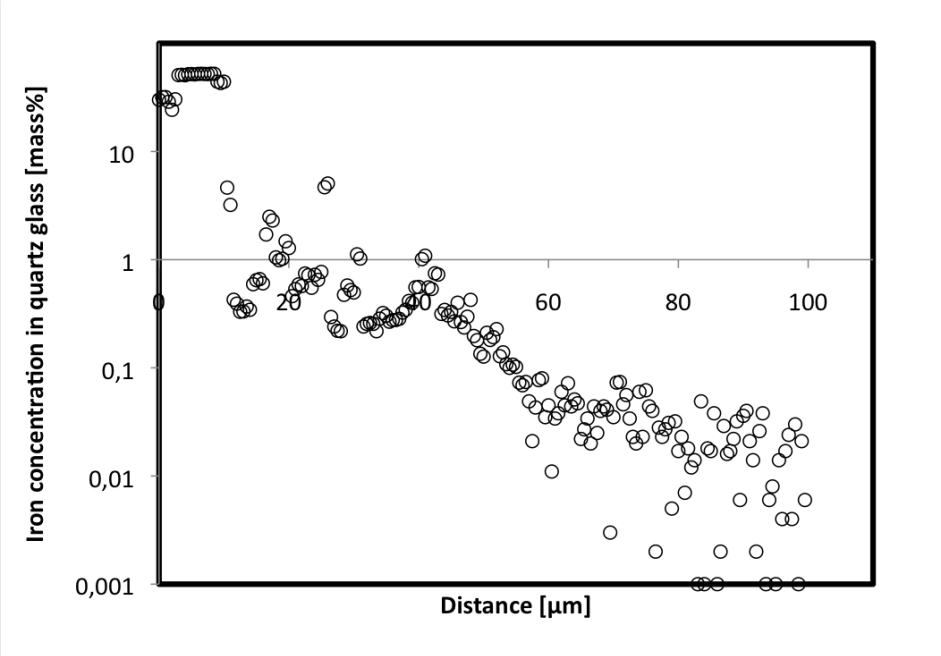

Figure D.5: Iron concentration [mass%] as a function of distance [µm] obtained from line scan Qr.1100.5.1.2

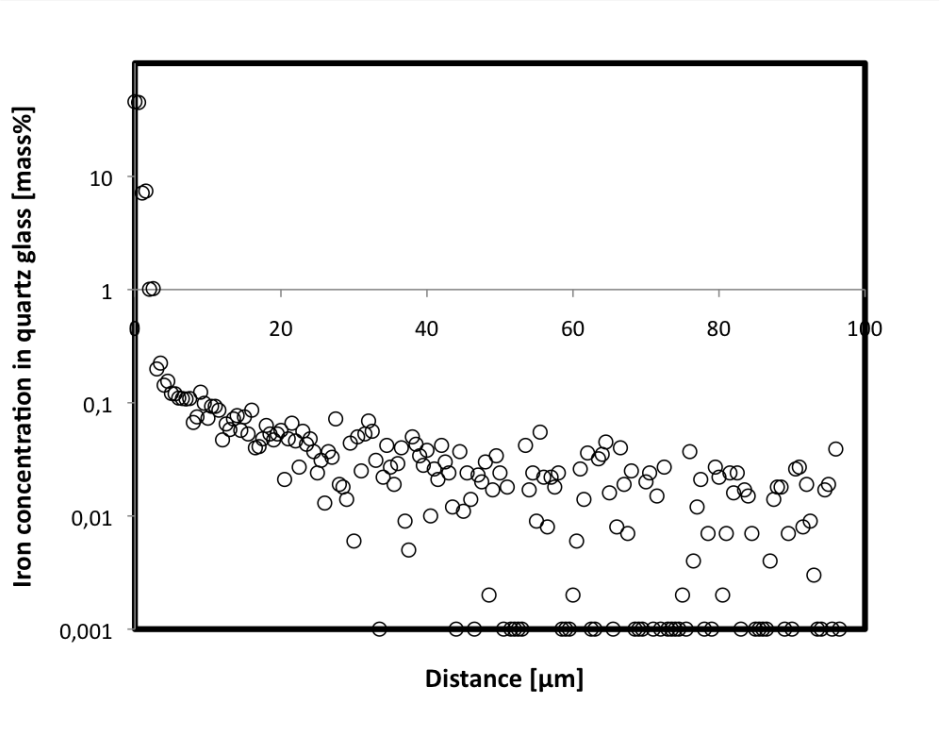

Figure D.6: Iron concentration [mass%] as a function of distance [µm] obtained from line scan Qr.1100.7.1.1

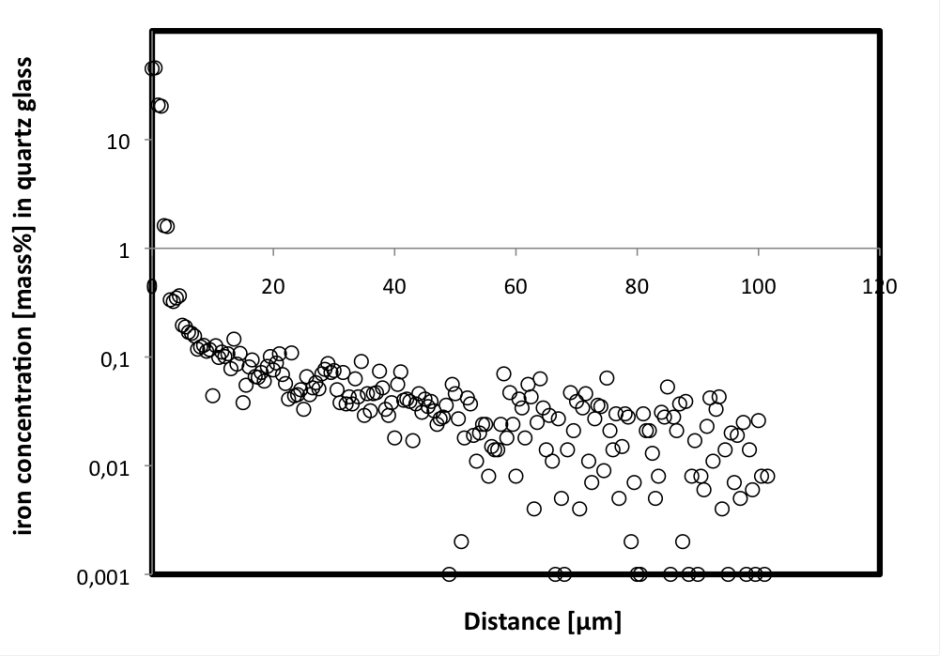

Figure D.7: Iron concentration [mass%] as a function of distance [µm] obtained from line scan Qr.1100.7.1.2

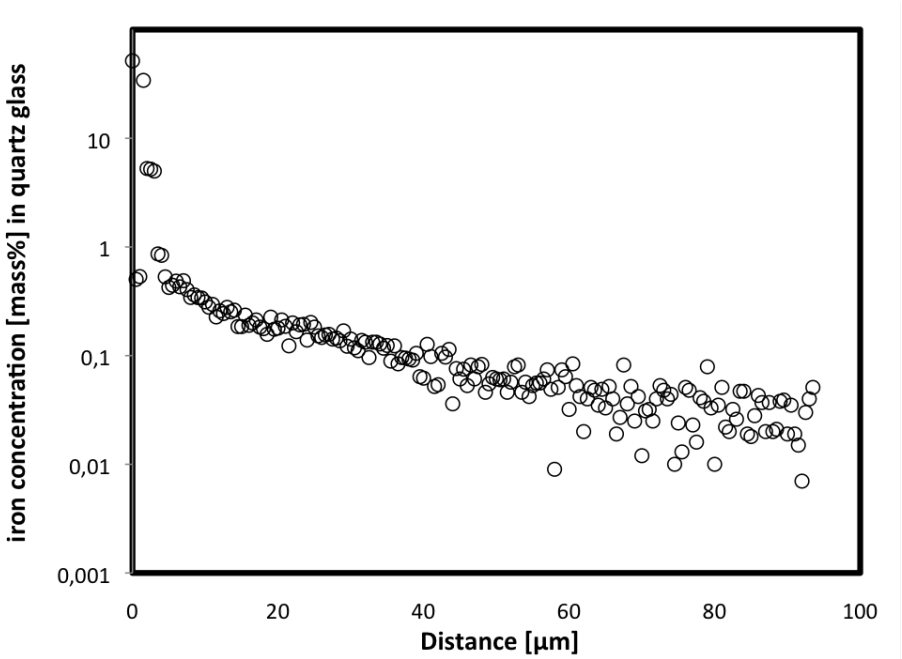

Figure D.8: Iron concentration [mass%] as a function of distance [µm] obtained from line scan Qr.1100.15.1.1

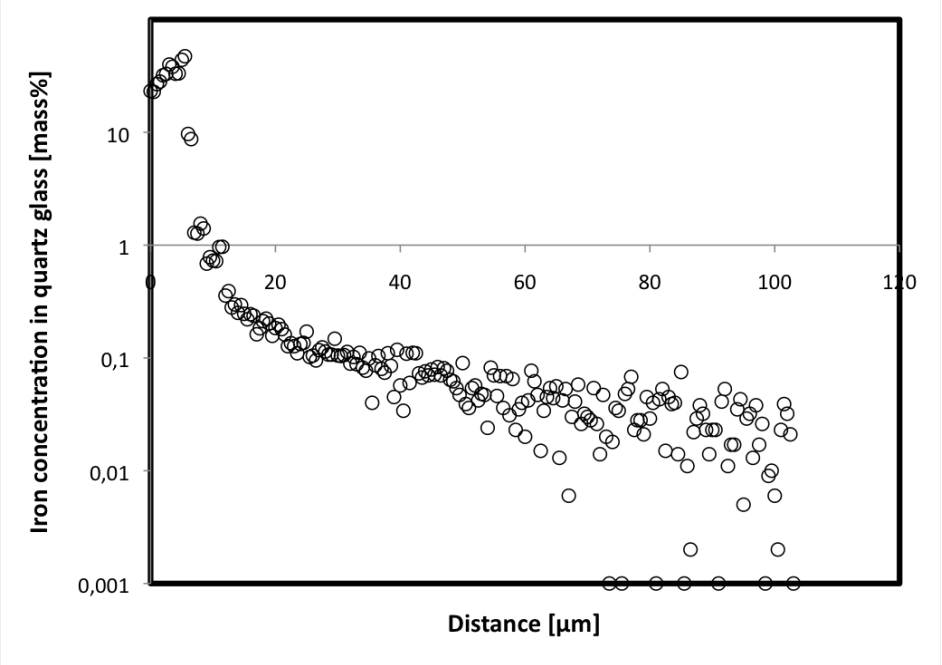

Figure D.9: Iron concentration [mass%] as a function of distance [µm] obtained from line scan Q.1100.17.1.1

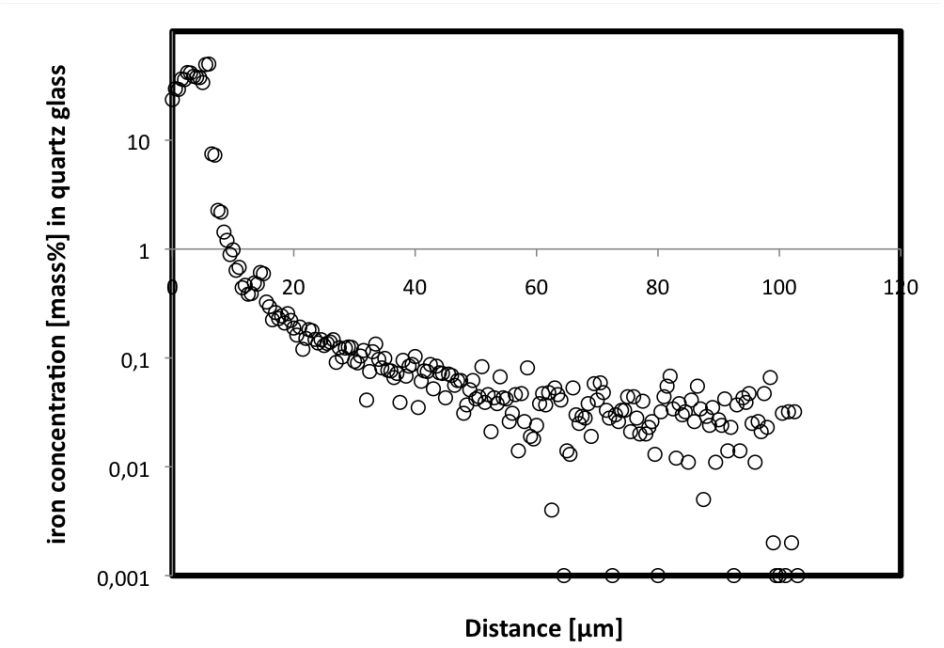

Figure D.10: Iron concentration [mass%] as a function of distance [µm] obtained from line scan Q.1100.17.1.2

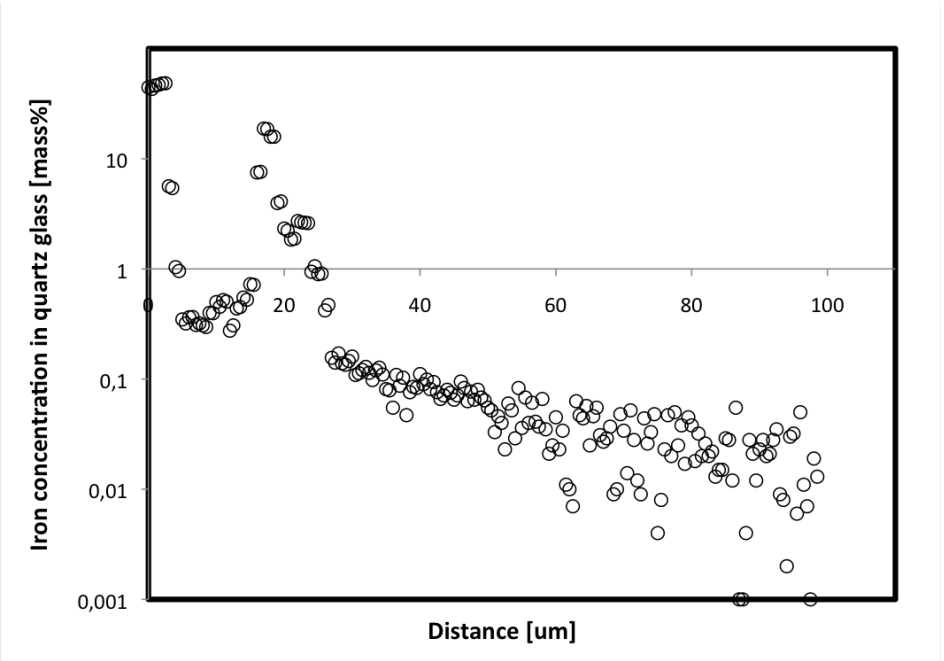

Figure D.11: Iron concentration [mass%] as a function of distance [µm] obtained from line scan Qr.1200.15.1.1

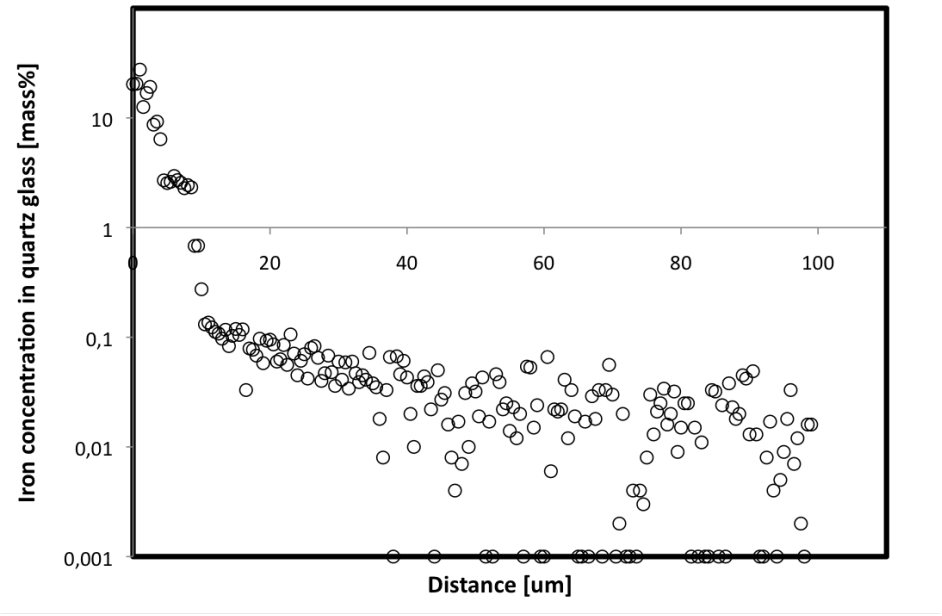

Figure D.12: Iron concentration [mass%] as a function of distance [µm] obtained from line scan Qr.1200.15.1.2

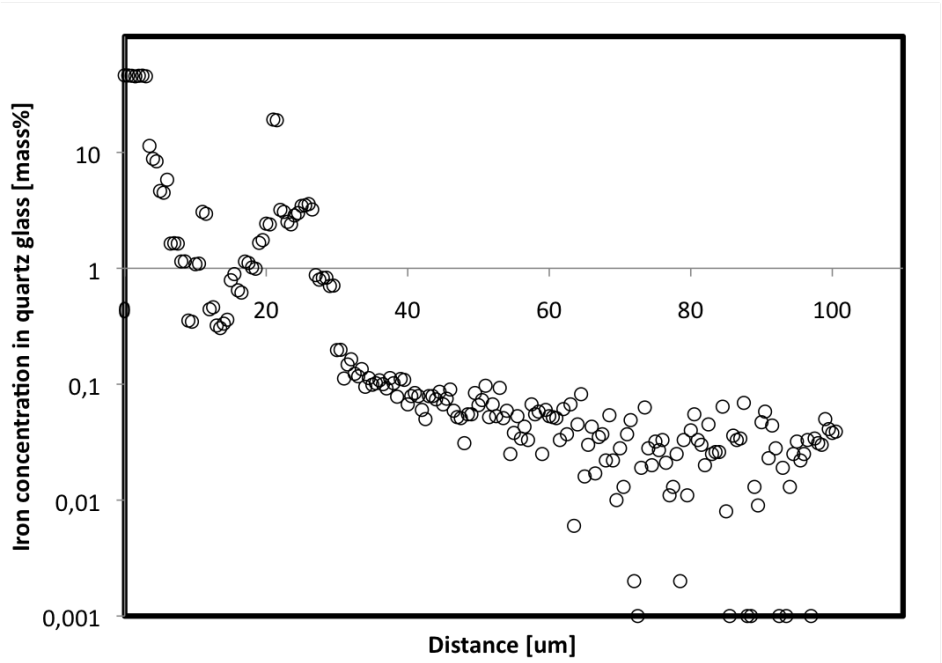

Figure D.13: Iron concentration [mass%] as a function of distance [µm] obtained from line scan Qr.1200.15.1.3

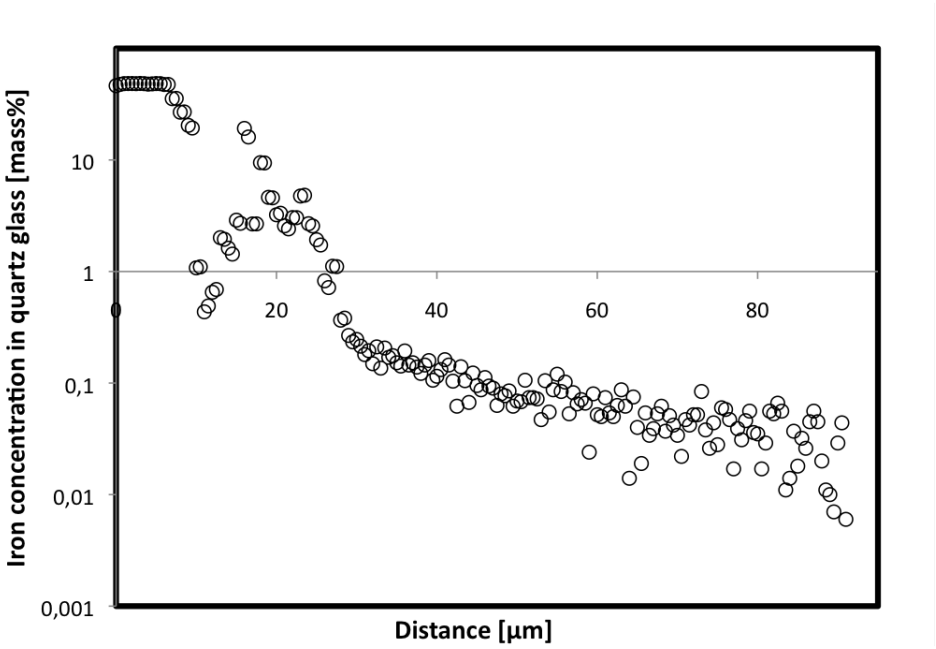

Figure D.14: Iron concentration [mass%] as a function of distance [µm] obtained from line scan Q.1300.3.1.2

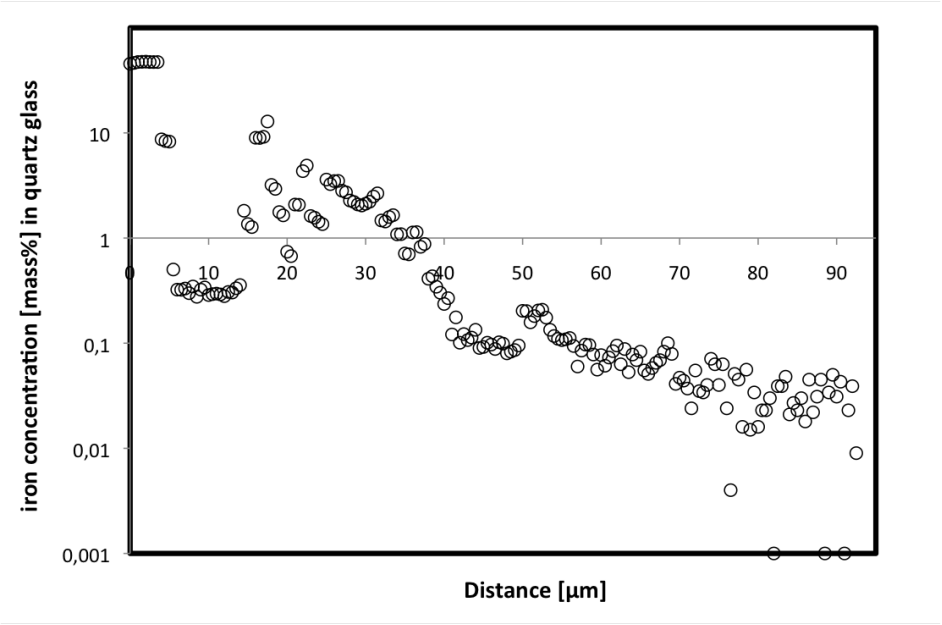

Figure D.15: Iron concentration [mass%] as a function of distance [µm] obtained from line scan Q.1300.3.1.3

D.2 Crucible material

The diffusivities, D presented in Table 4.3, were obtained from the diffusion profiles presented in this section.

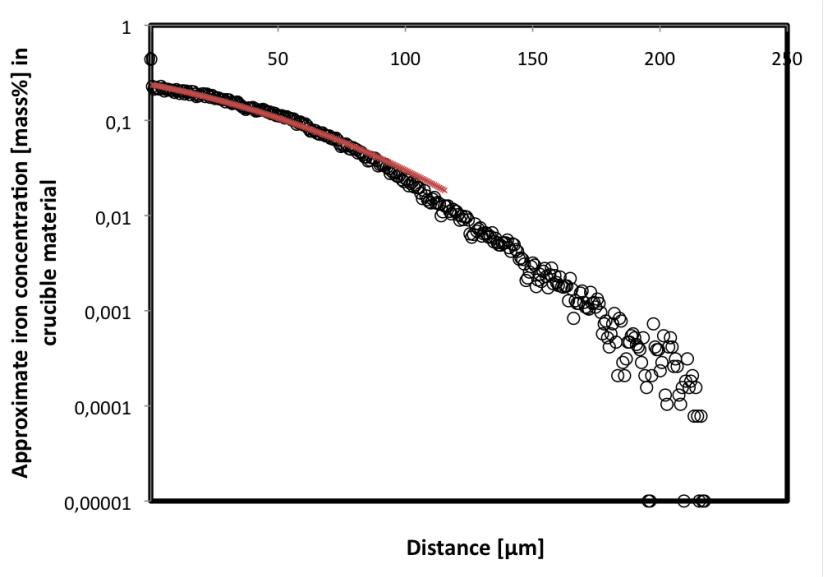

Figure D.16: Iron concentration [mass%] as a function of distance [µm] obtained from C.1100.17.1, with the image adjustments of 20 maximum mass% and script adjustments of Scenario 6

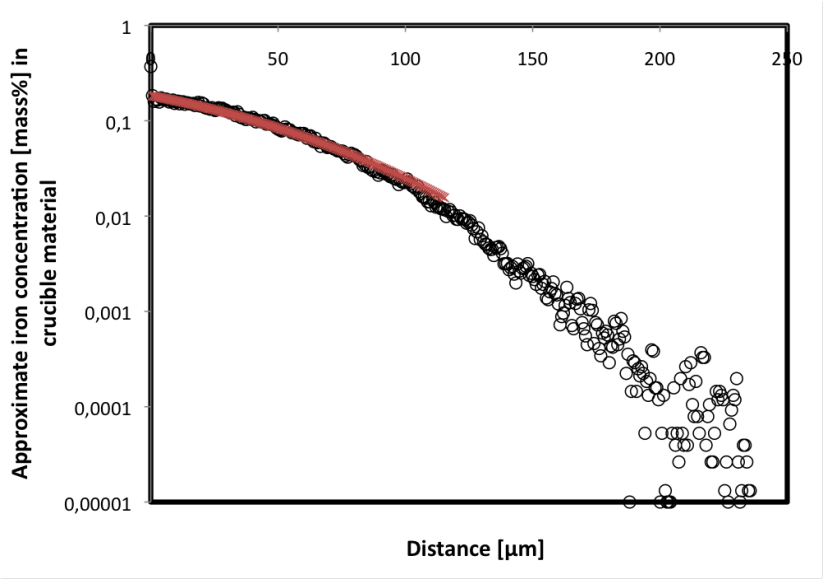

Figure D.17: Iron concentration [mass%] as a function of distance [µm] obtained from C.1100.17.1, with the image adjustments of 10 maximum mass% and script adjustments of Scenario 6

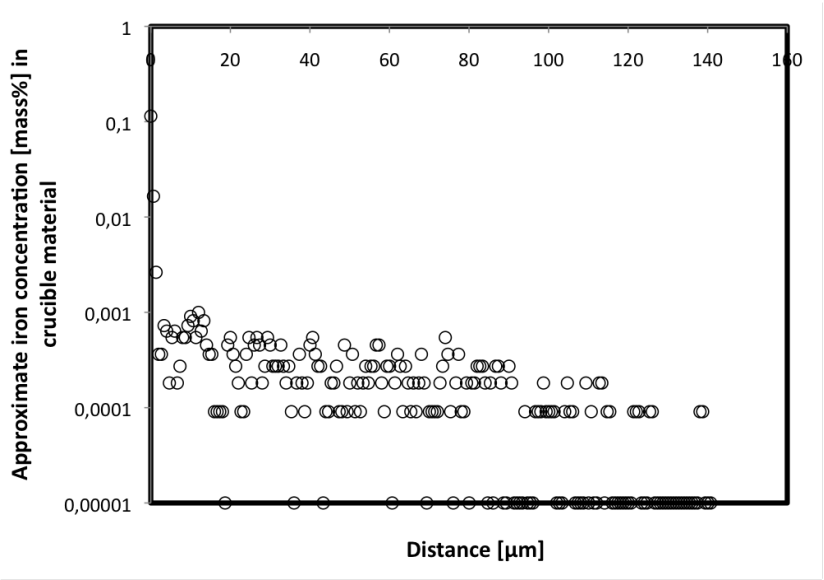

Figure D.18: Iron concentration [mass%] as a function of distance [µm] obtained from C.1200.7.1, with the image adjustments of 70 maximum mass% and script adjustments of Scenario 1

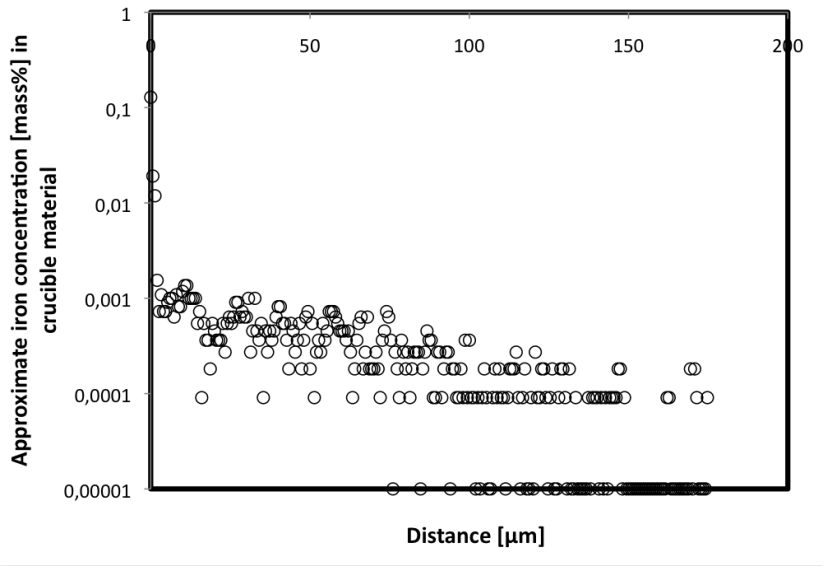

Figure D.19: Iron concentration [mass%] as a function of distance [µm] obtained from C.1200.7.1, with the image adjustments of 70 maximum mass% and script adjustments of Scenario 2

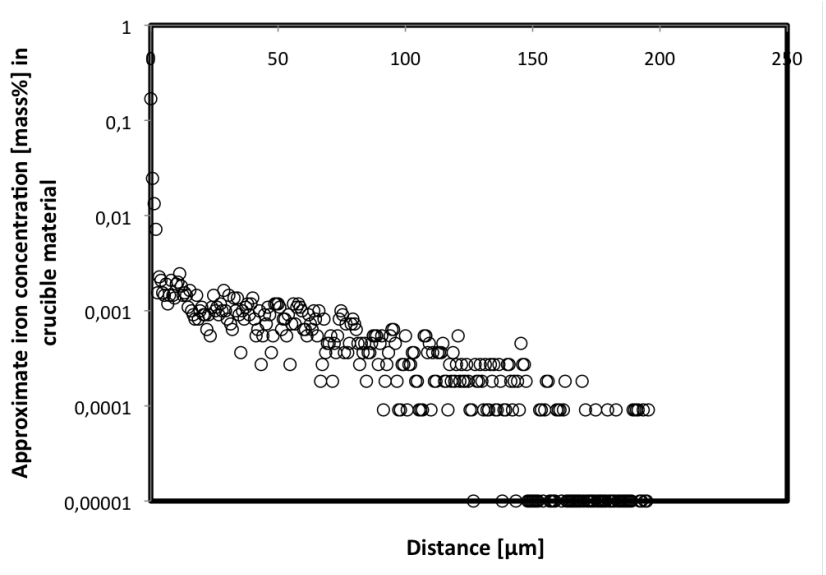

Figure D.20: Iron concentration [mass%] as a function of distance [µm] obtained from C.1200.7.1, with the image adjustments of 70 maximum mass% and script adjustments of Scenario 3

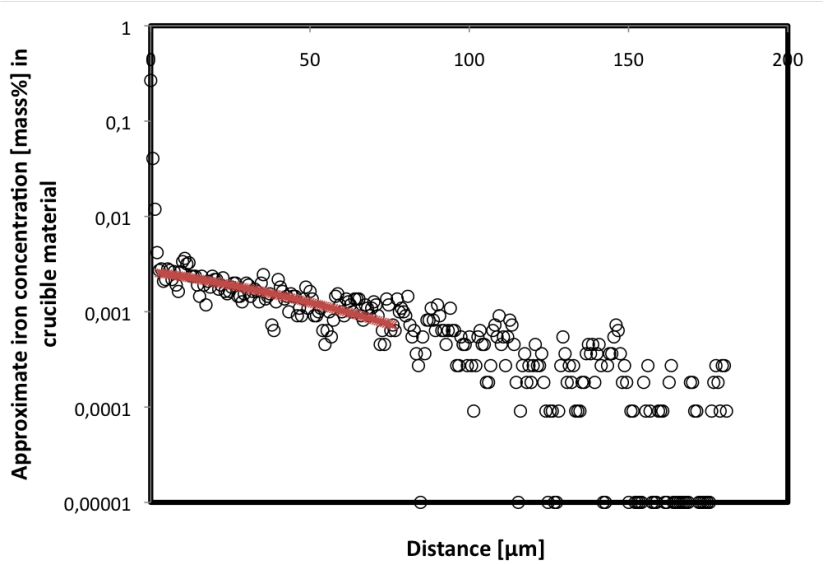

Figure D.21: Iron concentration [mass%] as a function of distance [µm] obtained from C.1200.7.1, with the image adjustments of 70 maximum mass% and script adjustments of Scenario 4

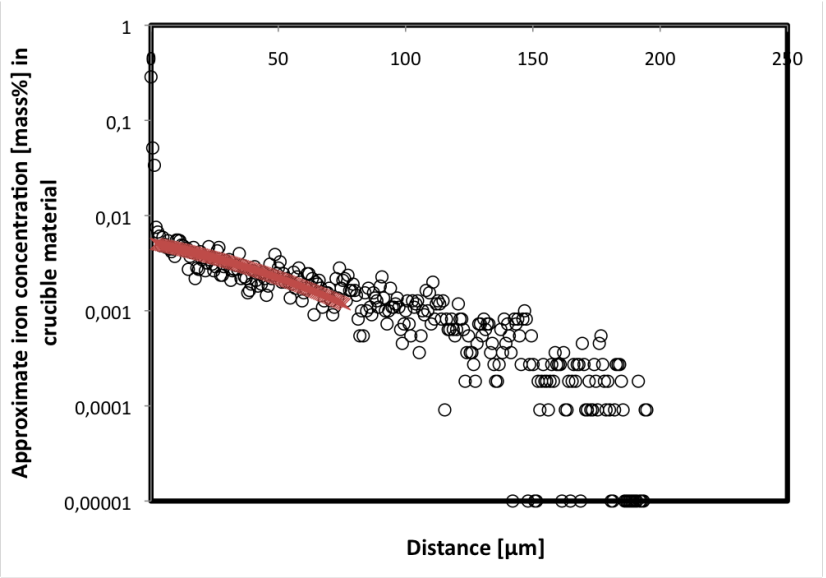

Figure D.22: Iron concentration [mass%] as a function of distance [µm] obtained from C.1200.7.1, with the image adjustments of 70 maximum mass% and script adjustments of Scenario 5

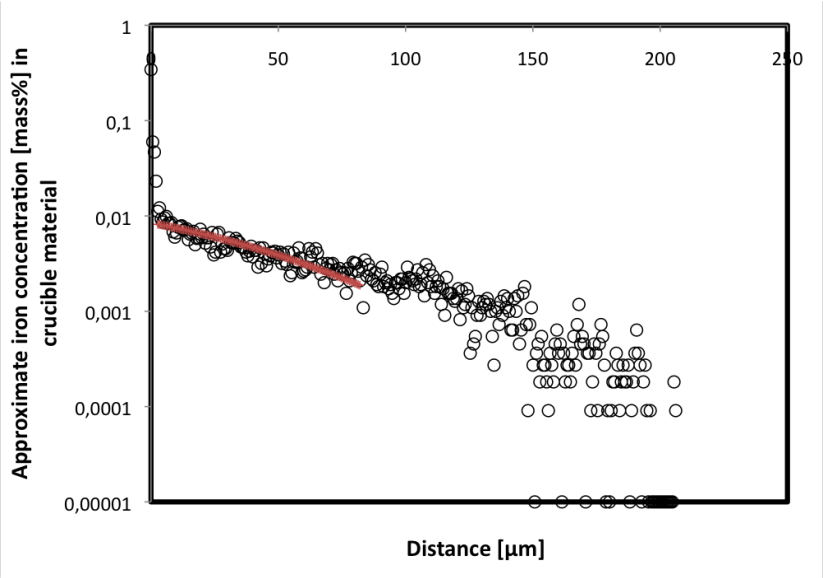

Figure D.23: Iron concentration [mass%] as a function of distance [µm] obtained from C.1200.7.1, with the image adjustments of 70 maximum mass% and script adjustments of Scenario 6

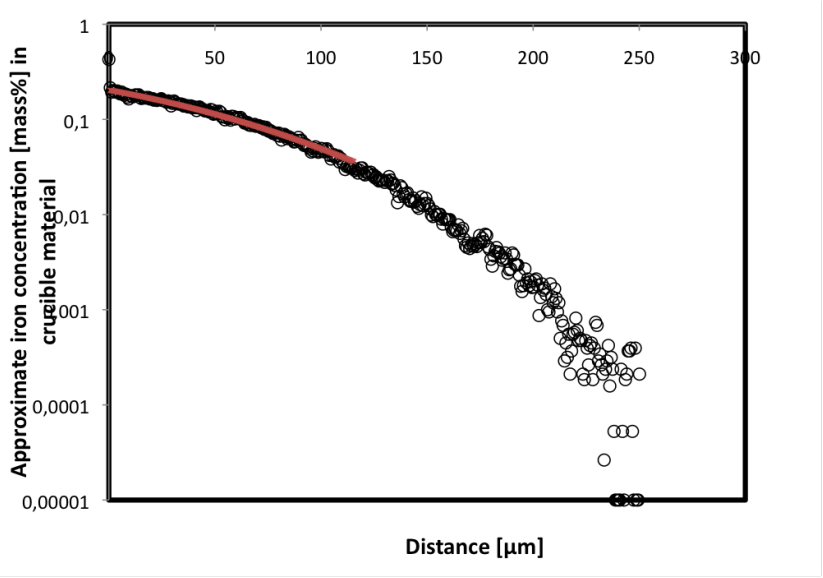

Figure D.24: Iron concentration [mass%] as a function of distance [µm] obtained from C.1200.7.1, with the image adjustments of 20 maximum mass% and script adjustments of Scenario 6

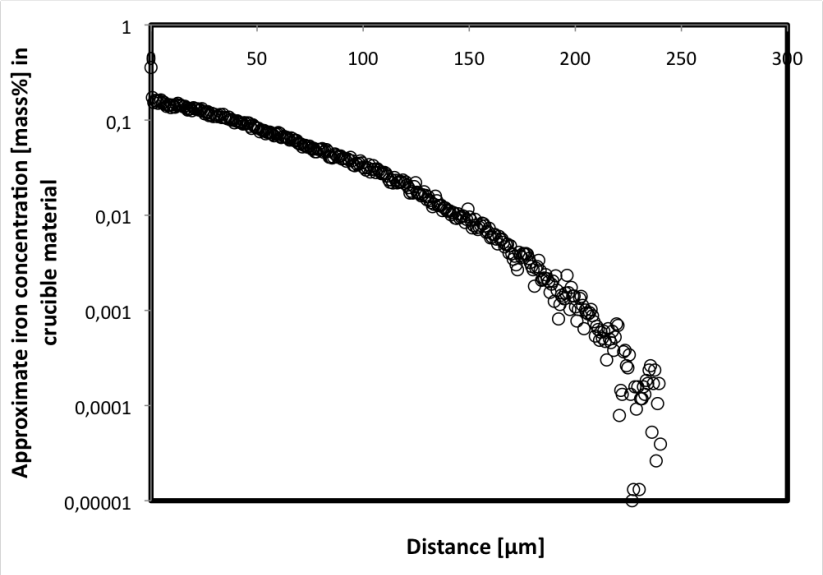

Figure D.25: Iron concentration [mass%] as a function of distance [µm] obtained from C.1200.7.1, with the image adjustments of 10 maximum mass% and script adjustments of Scenario 6

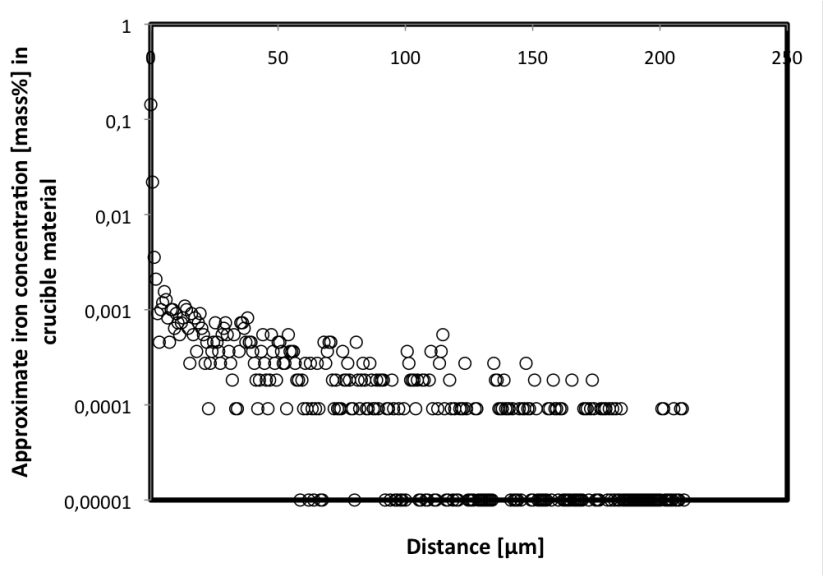

Figure D.26: Iron concentration [mass%] as a function of distance [µm] obtained from C.1300.3.1, with the image adjustments of 70 maximum mass% and script adjustments of Scenario 1

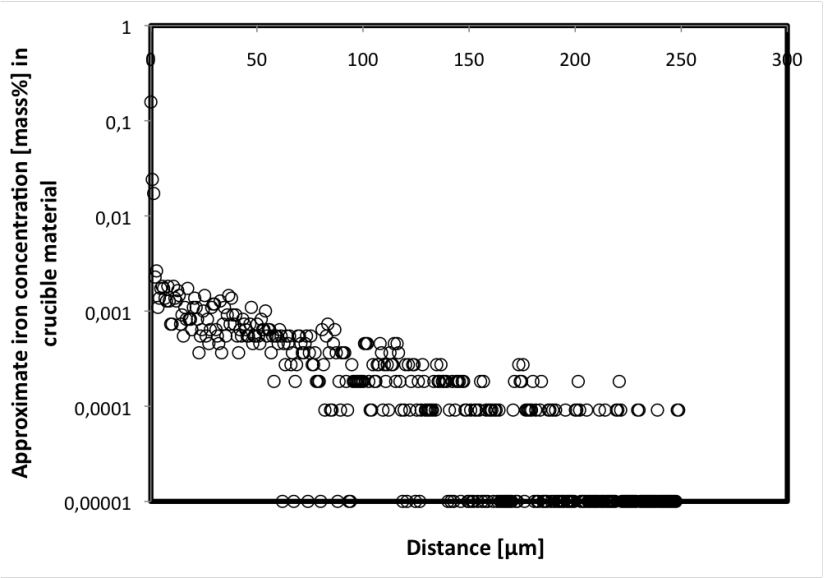

Figure D.27: Iron concentration [mass%] as a function of distance [µm] obtained from C.1300.3.1, with the image adjustments of 70 maximum mass% and script adjustments of Scenario 2

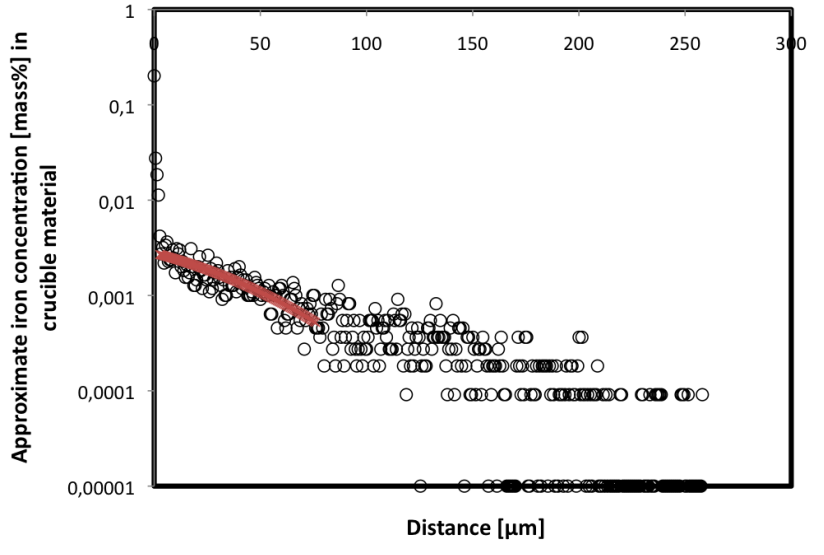

Figure D.28: Iron concentration [mass%] as a function of distance [µm] obtained from C.1300.3.1, with the image adjustments of 70 maximum mass% and script adjustments of Scenario 3

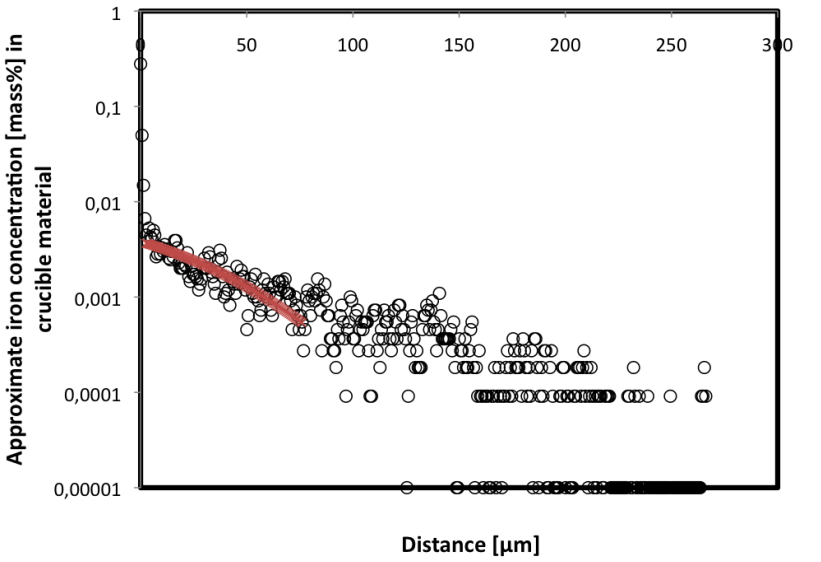

Figure D.29: Iron concentration [mass%] as a function of distance [µm] obtained from C.1300.3.1, with the image adjustments of 70 maximum mass% and script adjustments of Scenario 4

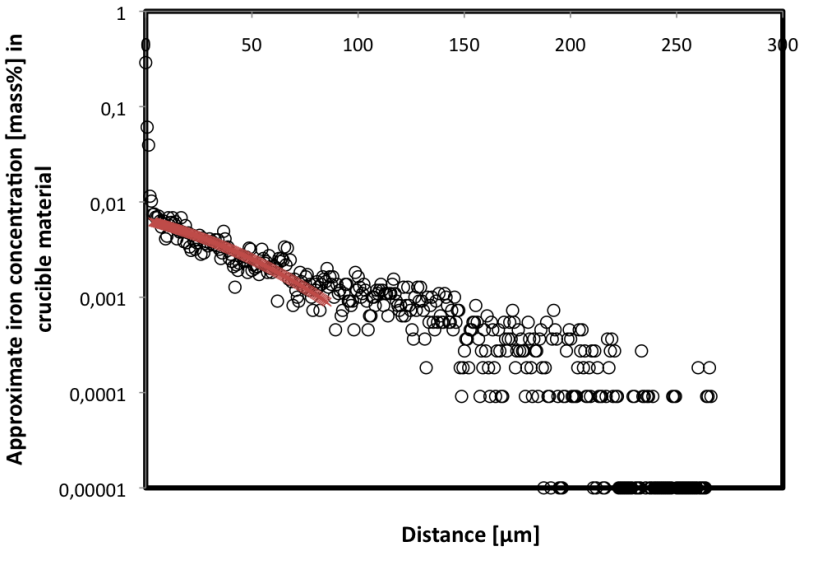

Figure D.30: Iron concentration [mass%] as a function of distance [µm] obtained from C.1300.3.1, with the image adjustments of 70 maximum mass% and script adjustments of Scenario 5

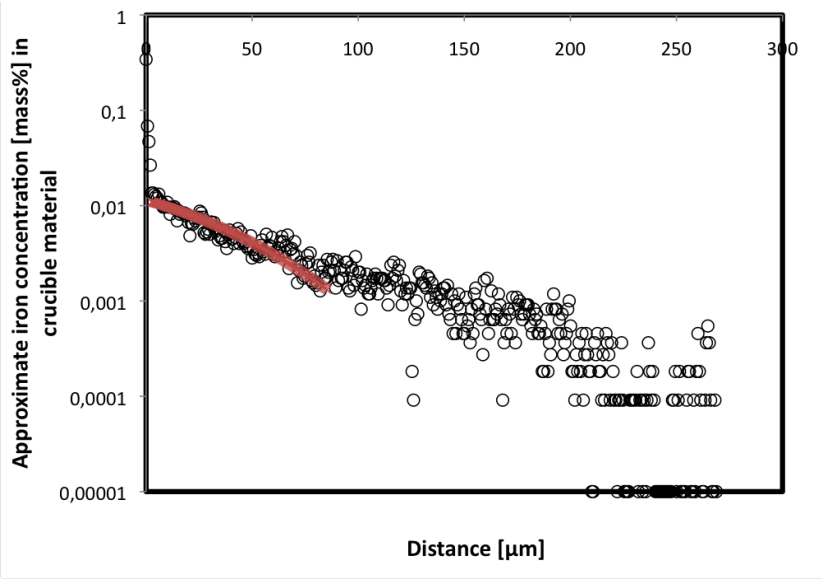

Figure D.31: Iron concentration [mass%] as a function of distance [µm] obtained from C.1300.3.1, with the image adjustments of 70 maximum mass% and script adjustments of Scenario 6

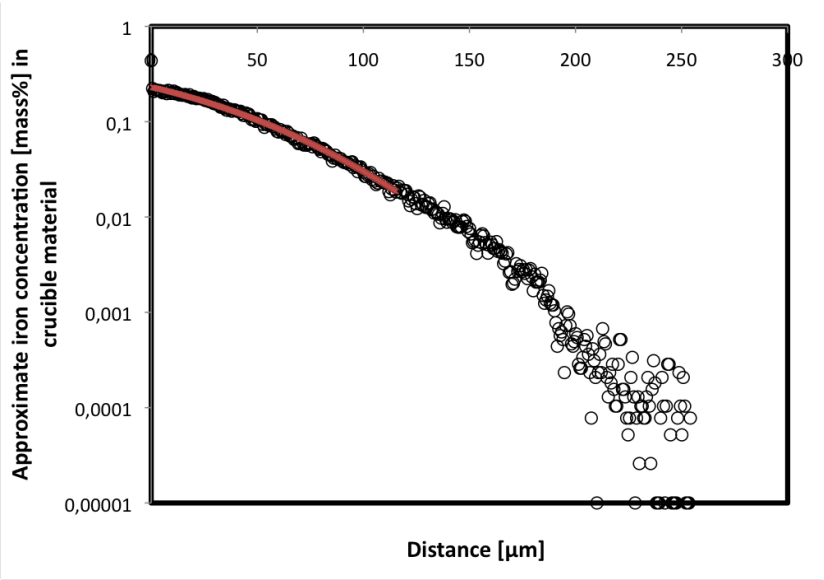

Figure D.32: Iron concentration [mass%] as a function of distance [µm] obtained from C.1300.3.1, with the image adjustments of 20 maximum mass% and script adjustments of Scenario 6

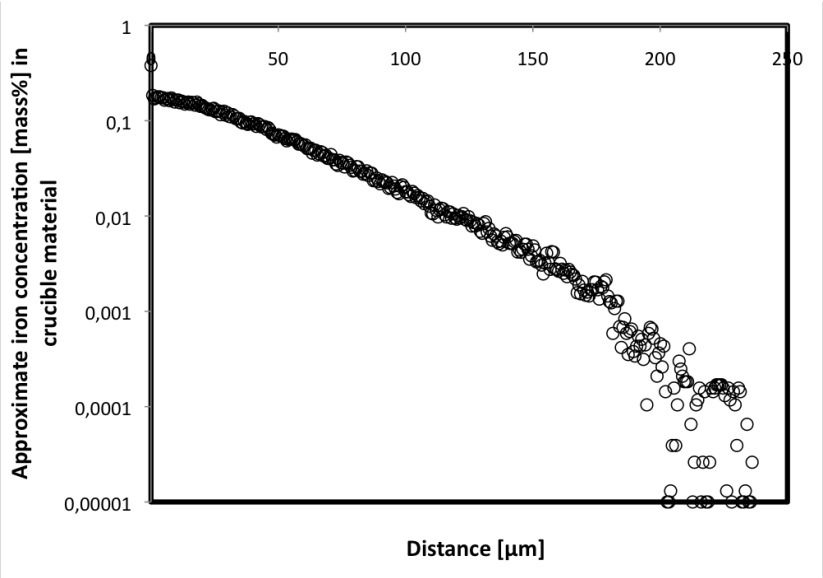

Figure D.33: Iron concentration [mass%] as a function of distance [µm] obtained from C.1300.3.1, with the image adjustments of 10 maximum mass% and script adjustments of Scenario 6